CrIS

Cross-track Infrared Sounder

Algorithm Theoretical Basis Document for the Cross Track Infrared Sounder (CrIS)

Volume I, Sensor Data Records (SDR)

ITT A/CD Document 818004

Document Number: **BOM-CrIS-0067**

Issue: **2** **Revision:** **-**

Issue Date: 25 May 2001 **Document Name:** BOM-CrIS-0067 2- SDR ATBD.doc

	Function	Name	Signature	Date
Prepared by	Scientist	Stéphane Lantagne		
Prepared by	Scientist	Yvan Dutil		
Prepared by	Scientist	Steve Levesque		
Prepared by	Scientist	François Châteauneuf		
Checked by	SDR Algorithms Lead	Robert Poulin		
Approved by	Project Manager	Germain Legault		

ABB Bomem Inc. • Unit of ABB Inc. • Automation Division

585 Charest Blvd. E, Suite 300 • Québec, Québec G1K 9H4 Canada • Phone (418) 877–2944 • Fax (418) 266–1422 • www.bomem.com

TABLE OF CONTENTS

1. INTRODUCTION 1
1.1 Purpose of Document 1
1.2 Scope 1
1.3 Document Overview 2
1.4 Reference documents 2
1.5 Acronyms 4
1.6 Notation and Symbols 7
1.6.1 Notation and Operators 7
1.6.2 Predefined Functions and Operators 7
1.6.3 List of Symbols Used 7
1.6.4 Identifiers Notation 8
1.6.5 Mathematical Definitions 10
2. SDR ALGORITHMS PRINCIPLES 11
2.1 Objective of the SDR Algorithms 12
2.2 Space Segment Signal Processing 13
2.2.1 Spikes Detection/Correction 14
2.2.2 Filtering and Decimation 15
2.2.3 Bit Trimming 18
2.2.4 Packet Encoding 19
2.3 Ground Segment Processing 20
2.4 Interferometer model 21
2.4.1 Instrument Phase 21
2.4.2 Other Signal Contributors 23
2.4.3 Instrument Line Shape 23
2.4.4 Other Types of Errors 23
2.4.5 Interferometer Modeling Equations 25
2.5 CrIS Characteristics 27
2.5.1 Double-Sided Interferogram Measurements 27
2.5.2 CrIS Spectral Bands 28
2.5.3 CrIS Field of Regard 29
2.5.4 CrIS Measurement Sequence 30
2.5.5 CrIS Signal Processing 31
2.6 Signal Representation 32
2.6.1 Array dimensions 33
2.6.2 Data ordering 36
3. SPECIAL CONSIDERATIONS 37
3.1 Non-linearity correction 37
3.2 Scan Mirror Polarization Compensation 37
3.3 Fringe Count Error Handling 38
3.3.1 Phase analysis 38
3.3.2 Chosen approach for detection and correction 38
3.3.3 FCE detection 39
3.3.4 FCE correction 42
3.4 Alignment of data to a common spectral grid. 44
3.5 ILS Correction 47
3.5.1 Introduction 47
3.5.2 CrIS Off-Axis Self Apodization 51

3.5.3 Self-Apodization removal 52
3.5.4 Residual term 57
3.5.5 Guard band damping 57
3.6 Signal Apodization 59
3.6.1 Unapodized channel response function 59
3.6.2 Hamming's filter function 61
3.6.3 Blackman's apodization function 63
4. SPECTRAL CALIBRATION 65
4.1 Neon-lamp as a spectral reference 66
4.1.1 Wavelength Calculation 66
4.2 Metrology Wavelength Monitoring 67
5. RADIOMETRIC CALIBRATION 68
5.1 Basic radiometric relations 69
5.2 General Calibration equation 70
5.3 CrIS Specific Calibration Equation 71
5.4 Radiometric model 72
5.4.1 Radiometric error 74
5.4.2 Temperature Computation 75
5.5 Signal Coaddition 75
5.5.1 Moving Average 75
5.5.2 Impact of temperature drift 77
5.5.3 Throughput delay 78
6. GEOMETRIC CALIBRATION 81
6.1 System characteristics 82
6.2 Field-of-View Location 83
6.3 Sequence of transformations 87
6.4 Pixel Size Computation 90
6.5 Time Representation 91
7. MODULES DEFINITION 92
7.1 General Flow diagram 94
7.2 Load and Sort Data Module 95
7.3 Compute Spectrum Module 96
7.3.1 Definition of variables 97
7.3.2 Exception handling 98
7.4 Fringe Count Error Detection Module 99
7.4.1 Definition of variables 101
7.4.2 Exception handling 102
7.5 Fringe Count Error Correction 103
7.5.1 Definition of variables 105
7.5.2 Exception handling 105
7.6 Moving Average Module 106
7.6.1 Definition of variables 107
7.6.2 Exception handling 108
7.7 Radiometric Calibration Module 109
7.7.1 Definition of variables 109
7.7.2 Exception handling 111
7.8 Health Monitoring Module 112
7.8.1 Definition of variables 113
7.8.2 Exception handling 114
7.9 Spectral Correction Module 115

7.9.1 Definition of variables 115
7.9.2 Auxiliary CMO computation 116
7.9.3 Exception handling 117
7.10 Geometric Calibration Module 118
7.10.1 Definition of variables 120
7.10.2 Exception handling 121
7.11 Data Quality Indicators round up 122
8. CONCLUSION 123
9. APPENDICES 125
9.1 Fast Fourier transforms 125
9.1.1 Comments on various algorithms 126
9.1.2 Data translation and centering 127
9.1.3 Prime Factor Algorithm Fast Fourier Transform 128
9.2 Alias unfolding 129
9.3 Linear fitting 131
9.3.1 Implementation of the linear interpolation 132
9.4 Numerical Integration 133
9.5 Determination of the goodness of fit 134
9.6 Sinc Smoothing 136
9.6.1 Definition of variables 137
9.7 Definitions 138
9.7.1 Sensor Calibration 138
9.7.2 Raw Data Record (RDR) 138
9.7.3 Sensor Data Record (SDR) 138
9.7.4 Environmental Data Record (EDR) 139
9.7.5 Data product Levels 139
9.7.6 Measured Data 140
9.7.7 Calibration Data 140
9.7.8 Ancillary Data 141
9.7.9 Other Instrument Specific Terms and Definitions 141

LIST OF FIGURES

Figure 1: CrIS System Segments 11
Figure 2: Data processing flow at various levels 11
Figure 3: Space Segment Processing of the CrIS Sensor 13
Figure 4: In-space interferogram processing 14
Figure 5: Interferogram spike 14
Figure 6: Parks-McClellan FIR Bandpass Filter for CrIS (LW) 16
Figure 7: Interferogram numerical processing 17
Figure 9: Interferogram envelope for a 16-bit ADC 18
Figure 9: Ground Processing Data Flowchart 20
Figure 11: Phase dependencies in an interferometer 25
Figure 12: Double-sided versus single-sided interferograms 27
Figure 13: Long, Mid, and Short Wave IR bands 29
Figure 14: Field of Regard definition 30
Figure 15: CrIS Measurement Sequence 31
Figure 16: Numerical vectors data ordering 36
Figure 1: Barrel-roll scanner type 37
Figure 2: FCE detection scheme 40
Figure 3: Effect of the **F**-matrix viewed in the interferogram domain 45
Figure 4: Instrument function contributors 48
Figure 5: Off-axis geometry and rays 48
Figure 6: Self-apodization due to beam divergence in the interferometer 50
Figure 7: Self-apodization function for the three basic pixel geometry 51
Figure 8: Off-axis geometry 53
Figure 9: Self-apodization effects and correction 55
Figure 10: Errors due to non-precise characterization 56
Figure 11: Boxcar apodization function and its sinc Fourier transform 60
Figure 12: Hamming apodization function and its Fourier transform 62
Figure 13: Blackman-Harris 3-terms apodization function and its Fourier transform 64
Figure 14: Spectral Calibration Parameter diagram 65
Figure 15: Neon calibration scheme using interpolation approach 67
Figure 16: Radiometric Calibration Parameter Diagram 68
Figure 17: Radiometric model when the scene is the ICT 73
Figure 18: Moving average window updating (example case N^{ma} = 5) 76
Figure 19: Relative error causes by combining many blackbodies (N=30) 77
Figure 20: Relative error causes by combining many blackbodies (N=8) 78
Figure 21: Throughput delay in measurement sequence with N^{ma}=30 79
Figure 22: Geometric Calibration Parameter diagram 81
Figure 23: CrIS viewing angle on Earth's surface 82
Figure 24: Geometry of the detector field of view and Earth ellipsoid intersection 83
Figure 25: Orientation of the inertial and Earth fixed coordinate systems with respect to the equatorial and orbital planes 84
Figure 26: Orientation of the detector field of view with respect to the spacecraft and local horizon coordinate systems. 85
Figure 27: Reference Axes and Attitude definition 86
Figure 43: General flow diagram for the Radiometric and Spectral calibration 94
Figure 44: Load and Sort Data Module Flow Chart 95
Figure 45: Compute Spectrum Flowchart 96

Figure 46: Compute Sampling Wavelength Flowchart 97
Figure 47: Fringe Count Computation Flowchart 100
Figure 48: Fringe Count Error Correction Flowchart 104
Figure 49: Moving Average Flowchart 106
Figure 50: Radiometric Calibration Flowchart 109
Figure 51: Health Monitoring Module Flowchart 113
Figure 52: Spectral Correction Flowchart 115
Figure 53: Self-Apodization Matrix Operator Computation Flowchart 116
Figure 54: S/C State Interpolation Module Flowchart 118
Figure 55: Geometric Calibration Module Flowchart 119
Figure 56: Interferogram decimation and alias unfolding 130

LIST OF TABLES

Table 1: Description of various global identifiers 9
Table 2: CrIS Specifications 28
Table 3: CrIS signal dimensions 31
Table 4: Long Wave array dimensions 34
Table 5: Middle Wave array dimensions 34
Table 6: Short Wave array dimensions 34
Table 7: Array dimensions and computing times (PII, 350 MHz) 35
Table 1: Resampling parameters for each band 44
Table 3: Error evaluation due to Dirac's delta approximation 54
Table 4: Summary of standard deviation error [%] 56
Table 5: Parameters for the post calibration filter f_F 58
Table 6: Blackman-Harris coefficients 64
Table 7: Temperatures used in the ICT model 73
Table 8: Radiometric model uncertainties 74
Table 9: Various time definitions 91
Table 16: List of SDR Algorithms Partitions and Modules 92
Table 17: CrIS Product Levels Classification 139

DOCUMENT CHANGE RECORD

Issue	Rev.	Date	Chapter/Paragraph Number, Change Description (and Reasons)
Draft	–	26 February 1999	Draft of document
1	–	26 March 1999	First release of document
1	A	21 April 1999	Small modifications according to comments and baseline changes.
1	B	27 April 2001	Interim (post DDR) release. Updated ICT radiometric model, radiometric calibration and ILS correction schemes. Updated sampling wavelength and array size. Clarified explanations about fringe count error handling.
2	-	25 May 2001	Revised interim (post DDR) release. High level architecture of processing algorithm follows specification. Minor corrections to reflect updated CrIS instrument baseline.

Measure to understand,

Understand to predict,

Predict to survive.

1. INTRODUCTION

1.1 PURPOSE OF DOCUMENT

The purpose of this document is to define the SDR Level 1B algorithms needed on ground in order to produce meaningful data meeting all the requirements of the CrIS instrument. Level 1B data is made of geolocated, radiometrically and spectrally (spatial frequency) calibrated spectra with annotated quality indicators.

The Cross-track Infrared Sounder (CrIS) is a part of the National Polar-orbiting Operational Environmental Satellite System (NPOESS) series of polar-orbiting spacecrafts. The CrIS *sensor* forms a key component of the larger Cross-track Infrared/Microwave Sounding Suite (CrIMSS) and is intended to operate within the context of the CrIMSS architecture. It also provides supporting measurements for a variety of other geophysical parameters.

The CrIS instrument is a Michelson interferometer infrared sounder covering the spectral range of approximately 3.9 to 15.4 microns. CrIS provides cross-track measurements of scene radiance to allow the calculation of temperature and moisture vertical distributions in the Earth's atmosphere.

1.2 SCOPE

This document presents the theoretical basis of the CrIS SDR Algorithms. The functional flow of algorithms required to transform Raw Data Record (RDR) coming from the satellite into Sensor Data Record (SDR) are described. These SDR are then transformed into Environmental Data Record (EDR). Physical retrievals of atmospheric parameters from infrared spectra are computed by accurate radiative transfer models, known as forward models, relating the atmospheric parameters to the observed channel radiances. The CrIS forward model is described in another document and is not presented here.

This document describes the CrIS SDR Algorithms specific processing required at the ground segment. It covers the processing needs for all data being sent to ground when the instrument is operational, including observational and calibration data, for all measurements performed by the instrument. The algorithms for decoding and calibrating the calibration data (e.g. generation of ICT radiance) are also covered here.

However, the present document does not cover the data manipulation related to all instruments of the NPOESS platform. In other words, it is assumed that the data entering the SDR algorithm processing chain is identical to the CCSDS formatted data leaving the instrument on board. The processing of the data produced when the instrument is under test or characterization, e.g. during the Commissioning Phase, is excluded. The operational and processing steps required during the Commissioning Phase will be addressed in an upcoming document. This will identify how CrIS is to be calibrated, what the baseline operational scenario is, how this scenario can be verified, etc.

The government considers the SDR and EDR algorithms adopted, adapted, or developed by the CrIS contractor to be scientific, rather than operational, algorithms. The CrIS contractor is not responsible for identifying or developing operational SDR and EDR algorithms for the CrIS.

1.3 DOCUMENT OVERVIEW

This document contains the SDR definitions for all the data processing algorithms. Chapter 1 serves as an introduction for the definition of various terms and concepts related to the CrIS instrument and data. Chapter 2 presents the SDR Algorithms principles and CrIS instrument characteristics. Chapter 3 describes special critical considerations for the SDR Algorithms design. Chapter 4, 5, and 6 discuss the spectral, radiometric, and geometric calibration respectively. Finally Chapter 7 gives a rigorous description of specific modules and functions and gives detailed information about the way that they will be applied. Assumptions, trade studies, alternatives, and justifications are given to highlight the choice of particular algorithms.

1.4 REFERENCE DOCUMENTS

No	Reference and Title
[RD 1]	CCSDS 701.0-B.2, CCSDS Recommendations for Space Data, System Sandards Telecommand Part 3: Data Management, Service, Architectural Definition, Issue 1, Jan 87.
[RD 2]	J. R. Birch and F. J. J. Clarke, “Fifty categories of ordinate error in Fourier transform spectroscopy” Spectroscopy Europe 7/4, 16 – 22, 1995.
[RD 3]	H. E. Revercomb, H. Buijs, H. B. Howell, D. D. Laporte, W. L. Smith, and L. A. Sromovsky, “Radiometric calibration of IR Fourier transform spectrometers: solution to a problem with the High-Resolution Interferometer Sounder”, Appl. Opt., Vol. 27, No 15, pp. 3210–3218, Aug. 1988.
[RD 4]	James W. Brault, “Fourier Transform Spectrometry”, National Solar Observatory, Tucson, Arizona, 1984.
[RD 5]	C. Temperton, “Implementation of a self-sorting in-place prime factor FFT algorithm”, Journal of Computational Physics, Vol. 58, pp. 283–299, 1985.
[RD 6]	C. Temperton, “A new set of minimum-add rotated DFT modules”, Journal of Computational Physics, Vol. 75, pp. 190–198, 1988.
[RD 7]	CrIS Engineering Demonstration Model (EDM) Test Results: Technical interchange Meeting (TIM) at Bomem, 5 – 6 October 1998.
[RD 8]	”Correction of the non-linearity of FT remote sensing instruments”, Richard L. Lachance, André Villemaire, and Luc Rochette, Third Workshop on Infrared Emission Measurements by FTIR, Quebec, Feb. 4 – 6 1998.
[RD 9]	“Spectral line-shape distortions in Michelson interferometers due to off-focus radiation source”, Pekka Saarinen and Jyrki Kauppinen, Appl. Opt., Vol. 31, No. 13, May 1992, pp. 2353 – 2359.
[RD 10]	“An Analytical Transformation Between Cosine Apodized Spectra and Unapodized Spectra”, C. D. Barnet, J. M. Blaisdell, and J. Susskind, Appl. Opt., Submitted Jan 1997.
[RD 11]	E. O. Brigham, “The Fast Fourier Transform”, Prentice hall, Englewood Cliffs, New Jersey, 1974.
[RD 12]	F. J. Harris, *Proceedings of the IEEE*, Vol. 66, (1978) 51.
[RD 13]	Neon Wavelength Measurement System, System Description, ITT-BOM-014/97, Issue 1, Nov 7, 1997.
[RD 14]	C. Weddigen et al., “Phase corrections for the emission sounder MIPAS-FT”, Appl. Opt. 32, 4586–4589, 1993.

[RD 15] E. E. Bell, "The use of asymmetric interferograms in transmittance measurements", *J. Physique Colloq.* No. 2, 28, 18 – 25, 1967.

[RD 16] J. R. Birch, "Imperfect optical figure in Fourier transform spectroscopy", *Infrared Physics*, 30, 155 – 159, 1990.

[RD 17] "Clouds and the Earth's Radiant Energy System (CERES) ATBD", Volume II – Geolocation, Calibration, and ERBE-Like Analyses (Subsystems 1-3), CERES Science Team, NASA Langley Research Center, Hampton, Virginia.

[RD 18] M. Frigo and S. G. Johnson, "The Fastest Fourier Transform in the West", Massachusetts Institute of Technology, http://theory.lcs.mit.edu/~fftw/, fft@theory.lcs.mit.edu.

[RD 19] W. H. Press, S. A. Teukolsky, W. T. Vetterling, and B. P. Flannery, *Numerical Recipes in C: The art of scientific computing*, Second Ed., Cambridge University Press, 994 p., 1992.

[RD 20] R. L. Burden and J. D. Faires, "Numerical Analysis", Fourth Ed. PWS-KENT Publishing Company, Boston, 1988. [RD 20] A. Chedin, N. A. Scott, C. Wahicle, and P. Moulinier, 1985: "Contribution to the development of radiative transfer models for high spectral resolution observations in the infrared". *J. Quant. Spectrosc. Radiat. Transfer*, Vol. 53, No. 6, pp. 597–611. (TIGR)

[RD 21] P. R. Bevington and D. K. Robinson, *Data reduction and error analysis for the physical sciences*, Second Edition, McGraw-Hill, Inc., New York, 328 p., 1992.

[RD 22] J. F. Hair, Jr., R. E. Anderson, R. L. Tatham, *Multivariate Data Analysis*, with readings", Second Ed., Macmillan Publishing Company, London, 449 p., 1987.

[RD 23] Erwin Kreyszig, *Advanced Engineering Mathematics,* Seventh Ed., John Wiley & Sons, Inc., New York, 1400 p., 1993.

[RD 24] CrIS SDR Document, Appendix A: Definition/Glossary of Terms, Revision 1998-04-17, R. J. Hertel, editor.

[RD 25] IPO CrIS Sensor Requirements Document (SRD), Revision 4/2/98

[RD 26] MIPAS, Michelson Interferometer for Passive Atmospheric Sounding, ESA ENVISAT-1 Instrument. http://envisat.estec.eas.nl/instruments/mipas,

[RD 27] IASI, Infrared Atmospheric Sounder Instrument, Alcatel.

[RD 28] SDR Scientific Code Description for the Cross Track Infrared Sounder (CrIS), BOM-CrIS-0084.

[RD 29] SDR Algorithms Requirements, ITT A/CD Document 8192900.

1.5 ACRONYMS

ADC	Analog to Digital Converted
AER	Atmospheric and Environmental Research Incorporated
ATBD	Algorithm Theoretical Basis Document
BB	Black Body
BS	BeamSplitter
CCSDS	Consultative Committee for Space Data Systems
CMO	Correction Matrix Operator
CPU	Central Processing Unit
CrIS	Cross-track Infrared Sounder
CrIMSS	Cross-track Infrared/Microwave Sounding Suite
DA	Dynamic Alignment
DFT	Discrete Fourier Transform
DoD	Department of Defense
DS	Deep Space
DSP	Digital Signal Processor
EDM	Engineering and Qualification Model
EDR	Environmental Data Record
EMI	Electro-Magnetic Interference
EOS	End of Scan
ES	Earth Scene
ESA	European Space Agency
ET	Elapsed Time
FCE	Fringe Count Error
FFT	Fast Fourier Transform
FIR	Finite Impulse Response
FLOP	Floating Point Operation
FOR	Field of Regard
FOV	Filed of View
FTS	Fourier Transform Spectrometer
FWHM	Full Width at Half Maximum
GEO	Geosynchronous Earth Orbit
HgCdTe	Mercury-Cadmium-Telluride
ICT	Internal Calibration Target
IF	Intermediate Frequency
IDPS	Interface Data Processing Segment
IERS	International Earth Rotation Service
IFFT	Inverse Fast Fourier Transform
IGM	Interferogram
ILS	Instrument Line Shape

IMC	Image Motion Compensator
INT	Interferometer
IPO	Integrated Program Office
IR	Infra Red
LOS	Line Of Sight
LWIR	Long Wavelength InfraRed
MCT	Mercury Cadmium Telluride
MPD	Maximum Path Difference
MFLOP	Million FLOP
MWIR	Mid Wavelength InfraRed
NEdN	Noise Equivalent Differential Irradiance
NEdT	Noise Equivalent Differential Temperature
NIST	National Institute of Standards and Technology
NL	Non-Linear
NLS	Natural Line Shape
NOAA	National Oceanic and Atmospheric Administration
NPOESS	National Polar-orbiting Operational Environmental Satellite System
OBT	On Board Time
OPD	Optical Path Difference
P/S	PorchSwing
PC	Photo-Conductive
PDR	Preliminary Design Review
PFA	Prime Factor Algorithm
ppm	Part Per Million
PRT	Platinum Resistance Thermometer
PV	Photo-Voltaic
RDR	Raw Data Record
RMS	Root Mean Square
RSS	Root Sum Squared
S/C	SpaceCraft
SBT	Satellite Binary Time
SDR	Sensor Data Record
SEU	Single Event Upset
SFR	System Functional Review
SNR	Signal-to-Noise Ratio
SPC	Spectrum
SRD	Sensor Requirement Document
SWIR	Short Wavelength Infrared
SZA	Solar Zenith Angle
TDI	Time Delay and Integration
TE	Thermo-Electric
TIGR	TOVS Initial Guess Retrieval

TIM	Technical Interchange Meeting
TIROS	Television InfraRed Observational Satellite
TLM	Telemetry
TOA	Top Of Atmosphere
TOVS	TIROS-N Operational Vertical Sounder
TSPR	Total System Performance Responsibility
UT	Universal Time
UTC	Universal Time Coordinated
ZPD	Zero Path Difference

N/A	Not applicable, none
TBC	To Be Confirmed
TBD	To Be Determined
TBR	To Be Reviewed
TBS	To Be Supplied

Units

cm	centimeter
cm^{-1}	wavenumber
count	count
day	day, Julian day
deg	degree
h	hour
K	Kelvin
μm	micrometer, micron
nm	nanometer
rad	radian
sec	second
sr	steradian

[a.u.]	Arbitrary units
[d.u.]	Digitalization units (ADC or digital counts)
[n.u.]	No units (also called *dl* for “dimensionless”)
[r.u.]	Radiance units: $\frac{\mathrm{m}W}{\mathrm{m}^2\,\mathrm{sr}\,\mathrm{cm}^{-1}}$

1.6 NOTATION AND SYMBOLS

This section gives the general description of all the notation conventions and mathematical symbols used throughout this document.

1.6.1 Notation and Operators

$\{\ \}$	Routine or process arguments, e.g. $\mathrm{F}\{x\}$
$(\ )$	Mathematical function argument, e.g. $\cos(\alpha)$, and also
	Range of mathematical vectors, e.g. $I(x)$, $S(\sigma)$
$[\ ]$	Index of numerical discrete arrays, e.g. $I[n]$, $S[m]$
$\langle\ \rangle$	Mean value, e.g. $\langle T \rangle$

1.6.2 Predefined Functions and Operators

$\tilde{Q}$	Complex quantity, as opposed to real quantity noted without tilde ($\tilde{}$)
$\mathrm{Re}\{\ \}$	Real part of a complex argument
$\mathrm{Im}\{\ \}$	Imaginary part of a complex argument
$\mathrm{F}\{\ \}$	Direct Fourier transform operator
$\mathrm{F}^{-1}\{\ \}$	Inverse Fourier transform operator
$\mathrm{FFT}\{\ \}$	Numerical discrete Fast Fourier Transform

1.6.3 List of Symbols Used

i	Complex unit: $i^2 = -1$
λ_L	Laser wavelength [cm] (e.g. 1550×10^{-7} cm)
x	Optical path difference [cm]
σ	Wavenumber [cm^{-1}]
σ_s	Sampling frequency of the reference laser [cm^{-1}] ($=1/\lambda_L$)
σ_{Max}	Spectral range maximum frequency [cm^{-1}] ($=\sigma_s/2$)
Δx	Sampling interval [cm]
$\Delta\sigma$	Spectral interval, also called wavenumber spacing [cm^{-1}]
ϕ	Phase function ($\tilde{S}(\sigma) = A(\sigma)\, e^{i\phi(\sigma)}$) [rad]
φ	Linear phase dependency [rad]
θ	Elevation Scan Mirror Angle [deg]
δ	Slant path viewing angle relative to sea level
Φ_C	Geodetic latitude of satellite [deg], range [–90..90]
Λ_C	Earth fixed longitude of satellite [deg], range [–180, +180]

α	Azimuth angle [deg]; angle of incidence of off-axis rays in interferometer
β	Elevation angle [deg]
T	Temperature [K]
N	Number of points in numerical arrays
n, m	Interferogram and spectrum data points indices $[0,\ldots,N-1]$
h	Fringe count error shift
★	Convolution operator (☆ is the Correlation operator)

1.6.4 Identifiers Notation

Symbol convention:

$I(x)$	Interferogram (IGM) (real or complex function), digitalization units [d.u.]
$\widetilde{S}(\sigma)$	Measured raw spectrum (SPC) radiance, (complex function), arbitrary units [a.u.]
$L(\sigma)$	Radiance, radiance units [r.u.]
$B(\sigma, T)$	Planck function, radiance units [r.u.]
$A(\sigma)$	Signal amplitude ($\widetilde{S}(\sigma) = A(\sigma)\, e^{i\phi(\sigma)}$) [a.u.]
$\widetilde{O}(\sigma)$	Instrument Offset (see expression in Section 5.2)
$\widetilde{G}(\sigma)$	Instrument Gain (see expression in Section 5.2)

General superscripts referring to generic calibration:

X^C	Cold calibration reference measurement
X^H	Hot calibration reference measurement
X^S	Scene measurement

Equivalent superscripts referring to actual CrIS measurements:

X^{ds}	Deep Space measurement ($\equiv X^C$)
X^{ict}	Internal Calibration Target measurement ($\equiv X^H$)
X^{es}	Earth Scene; atmospheric measurement ($\equiv X^S$)
in	Contribution from the interior of the interferometer, not coming from the FOV.
ext	Contribution from the outside of the interferometer, as viewed through the FOV.

Complexity operator:

$O(\,)$	"Complexity" of an algorithm, standing for *of the order of*. The number of operations (or the time of computation) for the specified algorithm is proportional to the argument given.

Table 1: Description of various global identifiers

$$I^{type}_{b,p,d,i,j}[index]$$

Variable	Descriptive name	Comment
superscript	*Type of signal*	
ds	Deep Space	
ict	Internal Calibration Target	
es	Earth Scene	
subscript	*Signal identification*	
b	Band index	1 = LW, 2 = MW, 3 = LW
p	Pixel number	1 – 9
d	IGM sweep direction index	0 = forward, 1 = reverse
i	FOR sweep counter in scan	1 for first orbit; $1 \le i \le 30$
j	Scan counter per orbit	reset at equator; $1 \le j < \text{TBD}$
$index$	*Element indices*	
m	Interferogram spatial index	$0 \le m \le N_b - 1$
n	Spectrum frequency index	$0 \le n \le N_b - 1$

Note: On all equations, the *prime* identification (e.g. $I'^{ds}_{b,p,d}$) refers to a transformed signal. In the following processing, all numerical arrays are treated with origin zero.

1.6.5 Mathematical Definitions

Fourier Transform:

Continuous domain:

$$S(\sigma) = \int_{-\infty}^{\infty} I(x)\, e^{-2\pi i \sigma x} dx$$
$$I(x) = \int_{-\infty}^{\infty} S(\sigma)\, e^{+2\pi i \sigma x} d\sigma \qquad (1)$$

Discrete domain:

$$S[n] = \Delta x \sum_{m=0}^{N-1} I[m]\, e^{-2\pi i m n / N}$$
$$I[m] = \Delta\sigma \sum_{n=0}^{N-1} S[n]\, e^{+2\pi i m n / N}$$

With the following notation indicating the relation between the two spaces (see Appendix 9.1 for more details):

$$S(\sigma) \leftrightarrow I(x)$$

Convolution:

$$\begin{aligned} h(\sigma) &= f(\sigma) \star g(\sigma) \\ &= \int_{-\infty}^{\infty} f(u)\, g(\sigma - u)\, du \\ &= \mathrm{F}^{-1}\{\, \mathrm{F}\{f(\sigma)\} \times \mathrm{F}\{g(\sigma)\}\} \end{aligned} \qquad (2)$$

Planck Function:

$$B(\sigma\ [\mathrm{cm}], T\ [K]) = \frac{c_1 \sigma^3}{e^{(c_2 \sigma / T)} - 1}\ [\mathrm{r.u.}] \qquad (3)$$

with the radiation constants: $c_1 = 1.191 \times 10^{-5}\ \mathrm{cm^3 m} W/(\mathrm{m^2 cm^{-1}})$

$c_2 = 1.439 \quad K\ \mathrm{cm}$

Sinc Function:

$$\mathrm{Sinc}(a\, x) \equiv \frac{\sin(\pi\, a\, x)}{\pi\, a\, x} \qquad (4)$$

Standard deviation:

$$\mathrm{Stdev}\{V\} = \sqrt{\frac{1}{N-1} \sum_{i=0}^{N-1} \left(V - \langle V \rangle\right)^2} \qquad (5)$$

where N is the length of the vector V

2. SDR ALGORITHMS PRINCIPLES

The CrIS system is defined as a spaceborne sensor and ground-based scientific algorithms. The development of scientific algorithms is necessary to define the methods for calibrating and coregistering raw sensor data and for producing the environmental data required by the users. This data is delivered to the users in the form of Raw Data Records (RDRs), Sensor Data Records (SDRs), and Environmental Data Records (EDRs). The figure below indicates the functional interdependence of these elements, and the bold lines and shaded modules reflect the elements specific to the SDR Algorithms presented in this document.

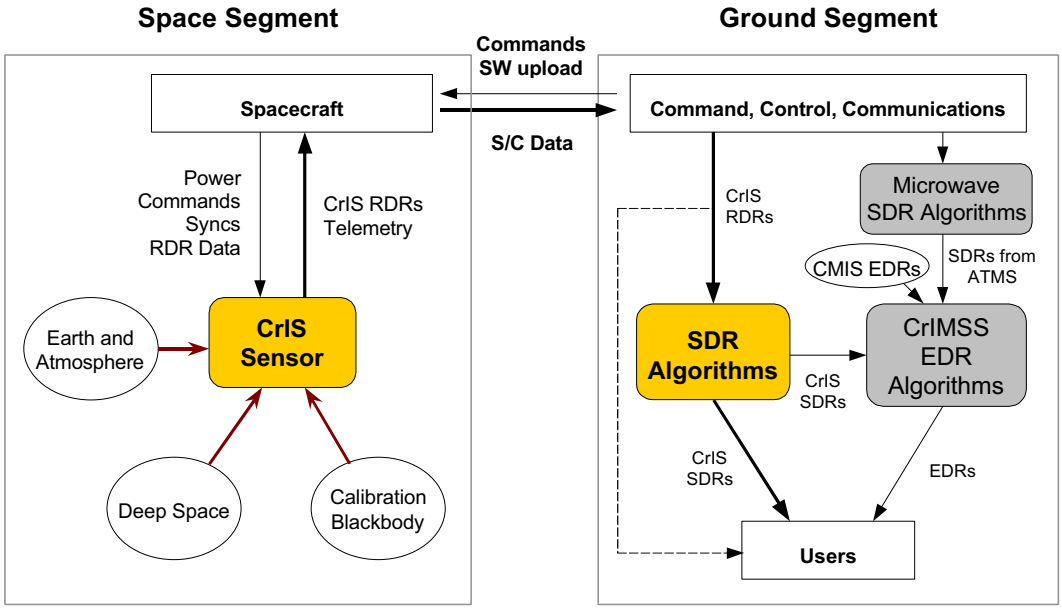

Figure 1: CrIS System Segments

Level 1B ground segment algorithms are required to transform raw instrument records (RDR) into sensor data records (SDR), which are essentially calibrated spectra. Auxiliary data will also be used in conjunction with several indicators to address the accuracy of the data. The SDRs are subsequently transformed into environmental data records (EDR) by another algorithm not presented in this document. Figure 2 shows the summary of the data processing flow between the measured radiance and the delivered EDR. All the needed functions are identified and described in this document, accompanied by all required major concepts and key equations.

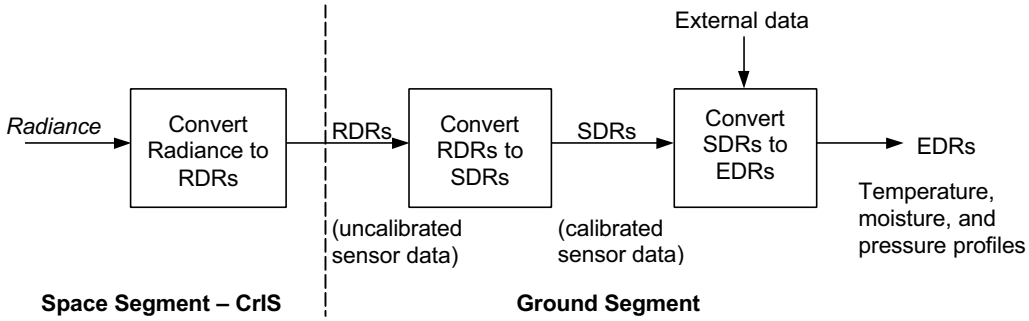

Figure 2: Data processing flow at various levels

2.1 OBJECTIVE OF THE SDR ALGORITHMS

Generally speaking, the SDR Algorithms system has to mathematically retransform the scene interferograms from the CrIS instrument into spectral information useful to scientists, considering all relevant data from characterization and calibration measurements in order to yield fully calibrated spectra. All this information will enable atmospheric key parameters retrieval.

The functions described in this section are to be implemented in the Ground Segment for processing of the CrIS scene and calibration data.

The incoming data may be acquired during deep space, internal calibration blackbody, and scene atmospheric measurements. Each incoming data therefore needs to be processed differently. Once combined together they will ultimately generate calibrated spectra with unavoidable associated errors.

The main objectives of the SDR Algorithms are:

Pre-process incoming data packets

- Load and sort data
- Convert interferograms to spectra
- Perform alias unfolding

Convert scene measurements into calibrated spectra

- Compute *spectral calibration*, using neon lamp reference measurements
  - » Map spectral channels to a fixed wavenumber grid
- Computes *radiometric calibration*, using reference calibration measurements
  - » Average warm target data, average cold target data
  - » Subtract sensor background radiance
  - » Remove sensor induced phase dispersion
  - » Remove detector non-linearity (if present)
  - » Correct for fringe count errors
  - » Correct for off-axis self-apodization on each FOV
  - » Correct for polarization errors
  - » Remove orthogonal noise components
- Compute *geometric calibration*, using LOS position and ephemeris data

Evaluate the associated error

- Check for data quality

2.2 SPACE SEGMENT SIGNAL PROCESSING

This section discusses processing done at the instrument level, namely spikes detection/correction, filtering and decimation, bit trimming, and packet encoding. Figure 3 summarizes the CrIS instrument part of the NPOESS satellite, viewed at the processing level.

CrIS is a Michelson interferometer based on the principle of Fourier Transform and designed to measure with high resolution and high spectral accuracy the emission of infrared radiation from the atmosphere in three bands in the spectral range from 3.9 to 15.4 μm (650 – 2550 cm^{-1}). The core of the instrument is a Fourier transform spectrometer which measures in one sweep the spectral features of the atmosphere with high spectral resolution and throughput. The spectrometer transforms the incoming spectral radiance, i.e. the spectrum, into a modulated signal, the interferogram, where all infrared wavenumbers in the band of interest are present simultaneously. The output from the spectrometer consists of one such interferogram for each observed scene.

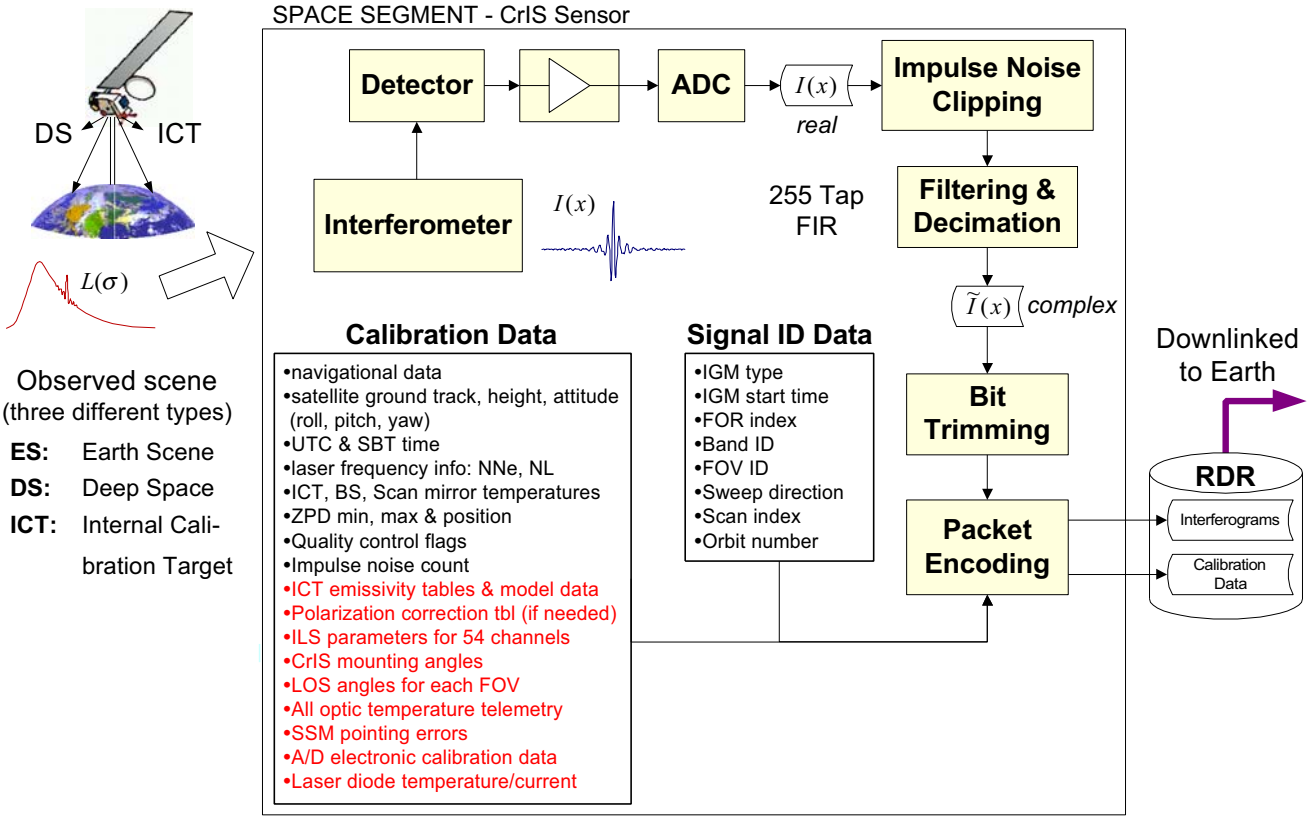

Figure 3: Space Segment Processing of the CrIS Sensor

Figure 4 depicts interferogram signal processing, showing filtering, decimation and data reduction.

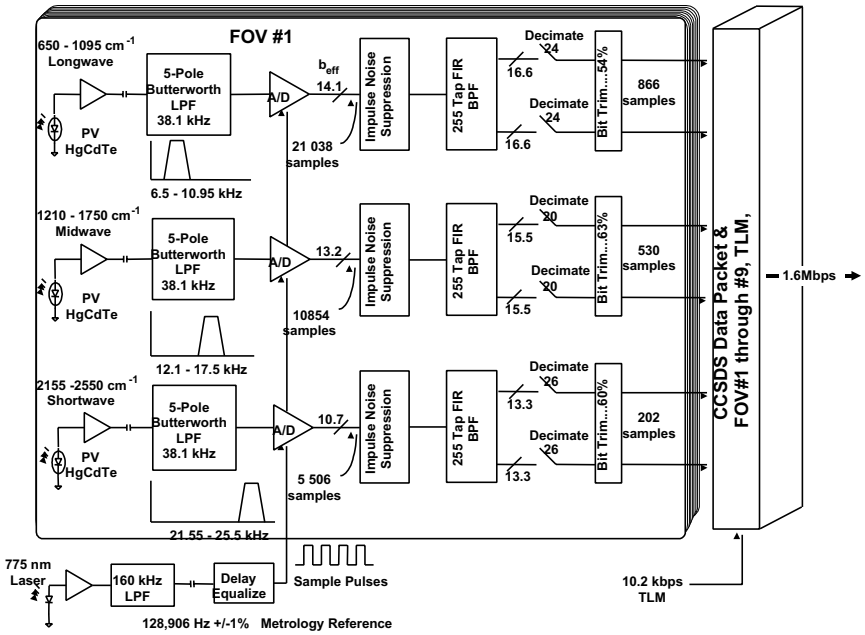

Figure 4: In-space interferogram processing

2.2.1 Spikes Detection/Correction

Noise spike detection and correction of raw interferogram data is accomplished by hardware and software on the CrIS sensor rather than by SDR Algorithms on the ground. This function is intended to suppress the effects of cosmic particle interaction with sensitive detector and associated electronics.

Detectors are subject to Impulse Noise due to direct bombardment of detector by high energy particles hitting spacecraft, then emitting X-rays that excite detector. The GOES satellite has shown to experience 2000 events/cm^2/sec (60 KeV X-rays), yielding to 2.5 hits per interferogram. The NPOESS orbit is under evaluation, but one can expect that the large CrIS detectors (1 mm diameter) will suffer from similar spikes with a span affecting many points.

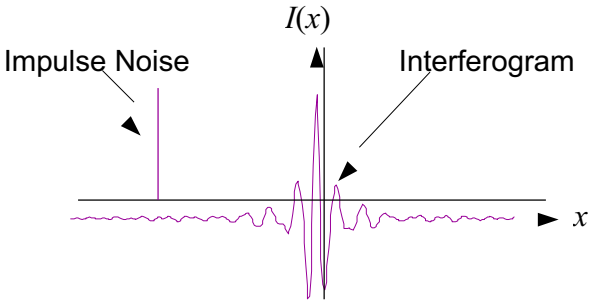

Figure 5: Interferogram spike

Spikes can be present anywhere in the interferogram, near or far the ZPD. Performing noise spike detection on raw interferograms and correction prior to filtering and decimation on the CrIS instrument is more effective than performing this same correction via software on the ground since the filtering and decimation process scrambles the data and makes the noise spike much less

detectable/correctable. Thus, scientific code performing this function is not needed since it will be performed on the instrument instead.

Error detection and correction of transmission link errors from spacecraft to ground station are assumed to be the responsibility of the spacecraft integrator and operate outside the bounds of the SDR Algorithms. It is assumed that the transmission link will incorporate robust coding methods to make this source of bit errors negligible (remaining bit error rates are quite small: of the order of 10^{-9} – 10^{-10}).

As the processing will be performed in-space, the algorithm or detection and correction must be minimal in order to avoid the implementation of dedicated electronics and supplementary storage memory. More elaborate algorithms could be designed, but the current baseline is to go for a simple straightforward approach. Detection makes use of a predefined bit trim mask, corresponding to an amplitude tight filtering window, that will identify erroneous spikes points. As a correction, each detected spike will be substituted by an average of the previous and following interferogram sample points on each side of the impulse. This measurement will be flagged for having been corrected for one or more spikes; the number of impulse noise hits is counted and reported for each interferogram via the telemetry data packets to aid in data quality assessment.

2.2.2 Filtering and Decimation

According to the current instrument design (and particularly the signal processor electronics), complex numerical filtering will be applied to the measurement data. The purpose of this section is to provide some theoretical background on this topic.

Neglecting the dispersion phenomenon inducing a non-null phase (see Section 2.3), an observed interferogram is basically a real and symmetrical function. The symmetry is about ZPD and, by extension about every multiple of MPD. The Fourier transform of such an interferogram is a real and symmetrical spectrum with symmetry about every multiple of the sampling frequency. We assume that the sampling frequency is chosen in order to meet the Nyquist criterion, i.e. there is no natural frequencies above half the sampling frequency. In other words, the full spectrum will show on one half the true physical spectrum and on the other half the image of this spectrum. Depending on the convention, this second half may be displayed as negative frequencies or as frequencies above half the sampling frequency (see Section 2.6).

A numerical filter with *real coefficients* shows the same symmetry as described above. The passband defined by such a filter transmits both the desired physical band and its image. Undersampling this filtered spectrum is possible provided the following two conditions are met:

1– The decimation factor is not larger than $\sigma_s/2(\sigma_1-\sigma_0)$, where σ_s is the sampling frequency (or Nyquist frequency) and σ_0, σ_1 are the band limits.

2– There is no folding frequency within the passband.

A *complex numerical filter* can be devised such that it has no image passband, by defining its imaginary part anti-symmetrical such that it produces a compensating negative image (negative frequencies are filtered out). After such a filtering, the only undersampling condition is:

1– The decimation factor is not larger than $\sigma_s/(\sigma_1-\sigma_0)$, where σ_S is the sampling frequency.

Thus, the decimation factor can be two times larger after complex filtering than the best case with real filtering. On the other hand, the generated spectrum produced by the numerical filtering is complex (composed of a real and an imaginary part).

Since the folding frequencies are not restricted to be out of the band of interest, there is not this additional restriction on the decimation factor. It is then possible to better optimize the decimation factor. This is where a gain can be made with respect to data reduction.

Figure 6 presents the 255 taps bandpass filter for the LW band, exhibiting a ±2.37 dB in-band ripple and a 69 dB stopband. This numerical filter approaches selectivity of optical alternatives and can be implemented with a low power ASIC electronic implementation (15 mWatt/channel).

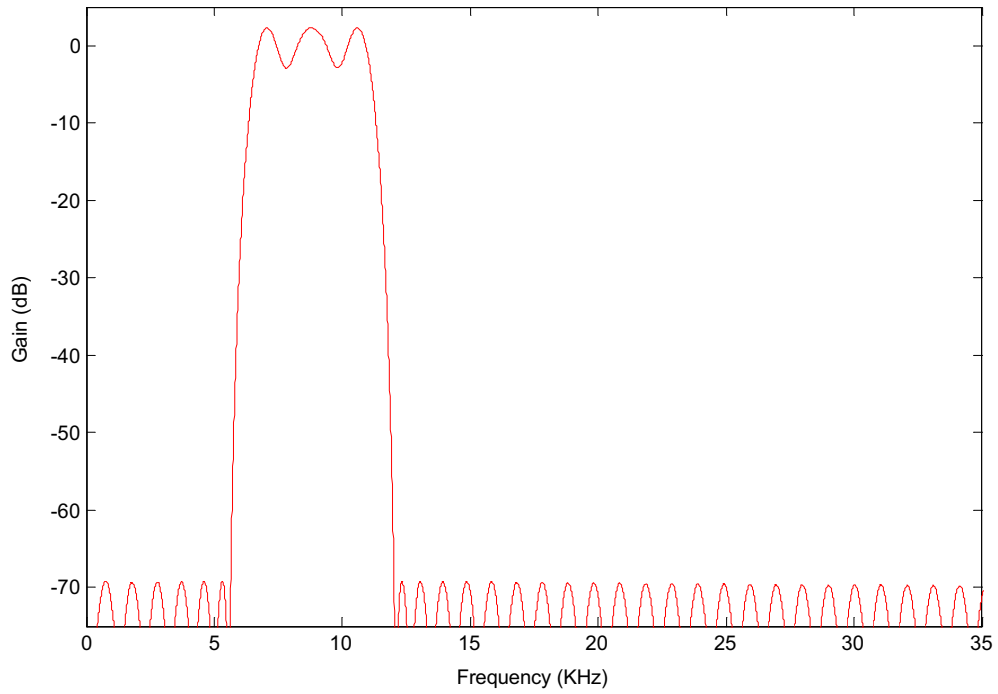

Figure 6: Parks-McClellan FIR Bandpass Filter for CrIS (LW)

Figure 7 summarizes the interferogram numerical acquisition process and Figure 56 summarizes the decimation and alias-folding process. The actual unfolding method processing needed for the proper recovery of the wavenumber axis is described in Section 9.2. This operation must be executed after the Fourier transform of every incoming decimated signals.

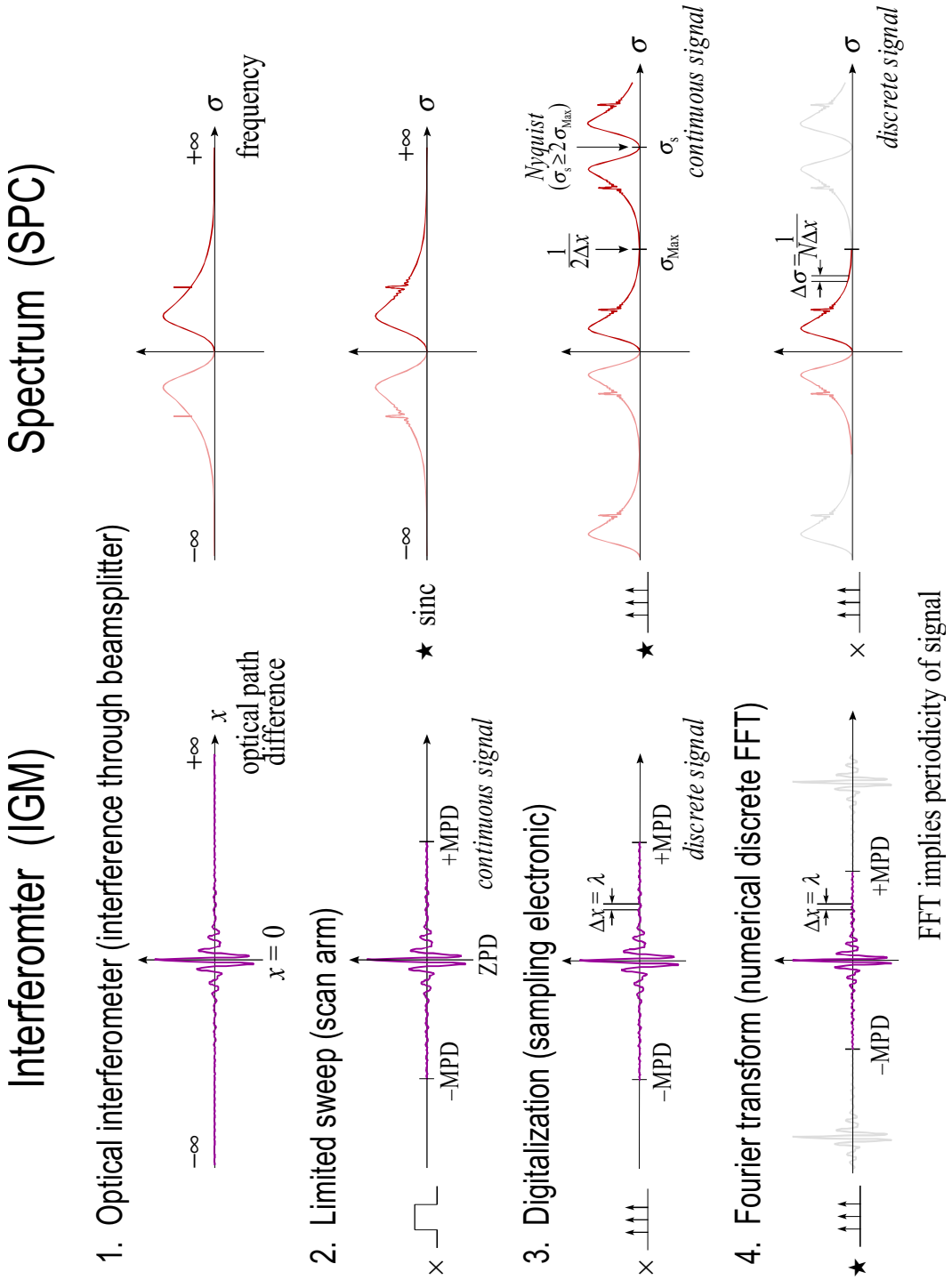

Figure 7: Interferogram numerical processing

2.2.3 Bit Trimming

In an effort to further compress the generated raw data rates to help meeting the available data transfer channels, bit truncation, or bit-trimming, is used to reduce the amount of data without losing information.

After performing filtering and decimation, the size of resulting interferograms can be reduced further by taking advantage of the characteristic distribution of the interferogram intensities. Intensities found away from the ZPD position are typically a few orders of magnitude lower than the intensity at the ZPD itself. The exact ratio depends primarily on the spectral content of the scene and other sources of radiation seen by the detector and on the bandwidth of the detector with its optical filters. To a lesser degree, it also depends on the recorded noise which can be important compared to the intensities in the interferogram ends. Keeping a constant gain while collecting the interferogram forces the digitalization range to be set by the ZPD intensity. For the points away from the ZPD this results in an under utilization of the digitized words. One can take advantage of this under utilization by omitting unused bits in a word (the most significant bits) and therefore contribute to data reduction. If the data values of the signal under consideration were more randomly distributed, as in spectral data, this method would not be appropriate as the range of points with important weights would become significant. This method is referred to here as bit trimming since the high order bits are trimmed from blocks of small valued data.

This bit trimming scheme is most useful for high resolution measurements where the ZPD region is narrow with respect to the full extent of the IGM. The full resolution sweeps benefit from extended truncation on a greater portion of its blocks than lower resolution sweeps. Bit truncation is most efficient when used with short block size. Compression rates on typical atmospheric spectra can range from 10 up to 40% reduction. Figure 8 shows the extent of the ADC bit-trimming mask, computed from the distribution of typical interferogram information. The CrIS bit-trimming masks enable compression factors of 37% in the LW, 27% in the MW, and 38% in the SW.

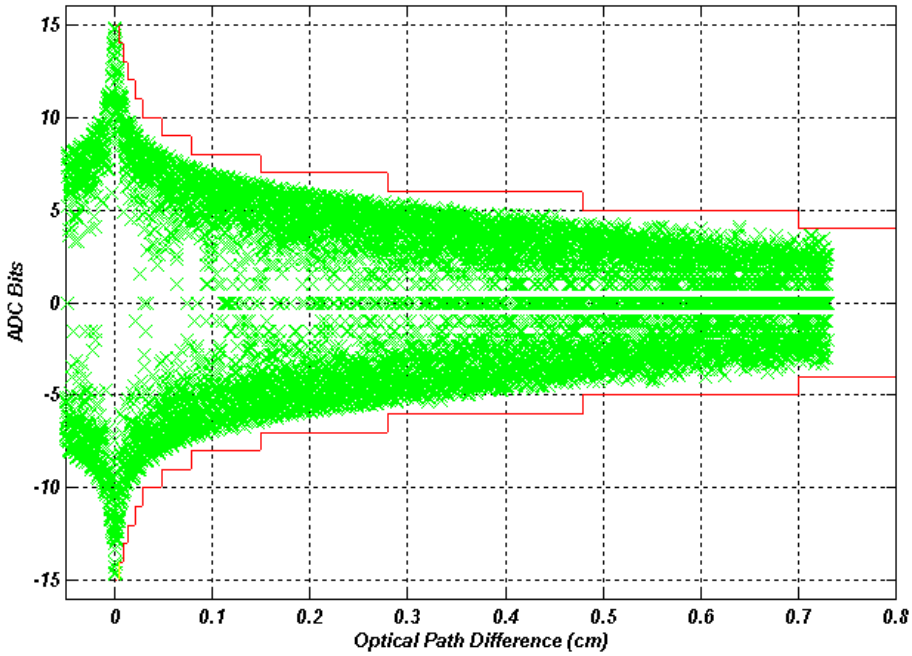

Figure 8: Interferogram envelope for a 16-bit ADC

2.2.4 Packet Encoding

All the data coming directly from the instrument are formatted into source packets. The data packets generated by the CrIS conform to the Consultative Committee for Space Data Systems (CCSDS) packetization per the real-time interface specification and the stored data interface specification. Details about the size, content and organization of data in the source packets as well as the data rate corresponding to the transfer of source packets to the ground processor can be found in [RD 1].

The data formatting and transmission will be performed as follows:

CCSDS Encoded Data Organized in Packets

- One packet per interferogram (includes identifiers)
- 27 packets per Field of Regard (FOR)
- One telemetry packet per FOR
- One diagnostic telemetry packet per FOR (when enabled)

1773A BUS Download to Spacecraft

- Spacecraft must service and download all 28 packets within 200 msec after collected

1773A BUS Upload to CrIS Sensor

- UTC time, S/C binary time, roll, pitch, yaw, position; once every second
- Commands
- Software uploads

2.3 GROUND SEGMENT PROCESSING

The SDR Algorithms can be viewed as two main modules being processed separately. Radiometric and spectral calibration are interlinked within one another, while geometric can be done in parallel. Those processes are described respectively in Chapters 4, 5, and 6. Individual sub-modules defining these super-modules are described in Chapter 7.

The ground processing flow is illustrated by the data flowchart of Figure 9.

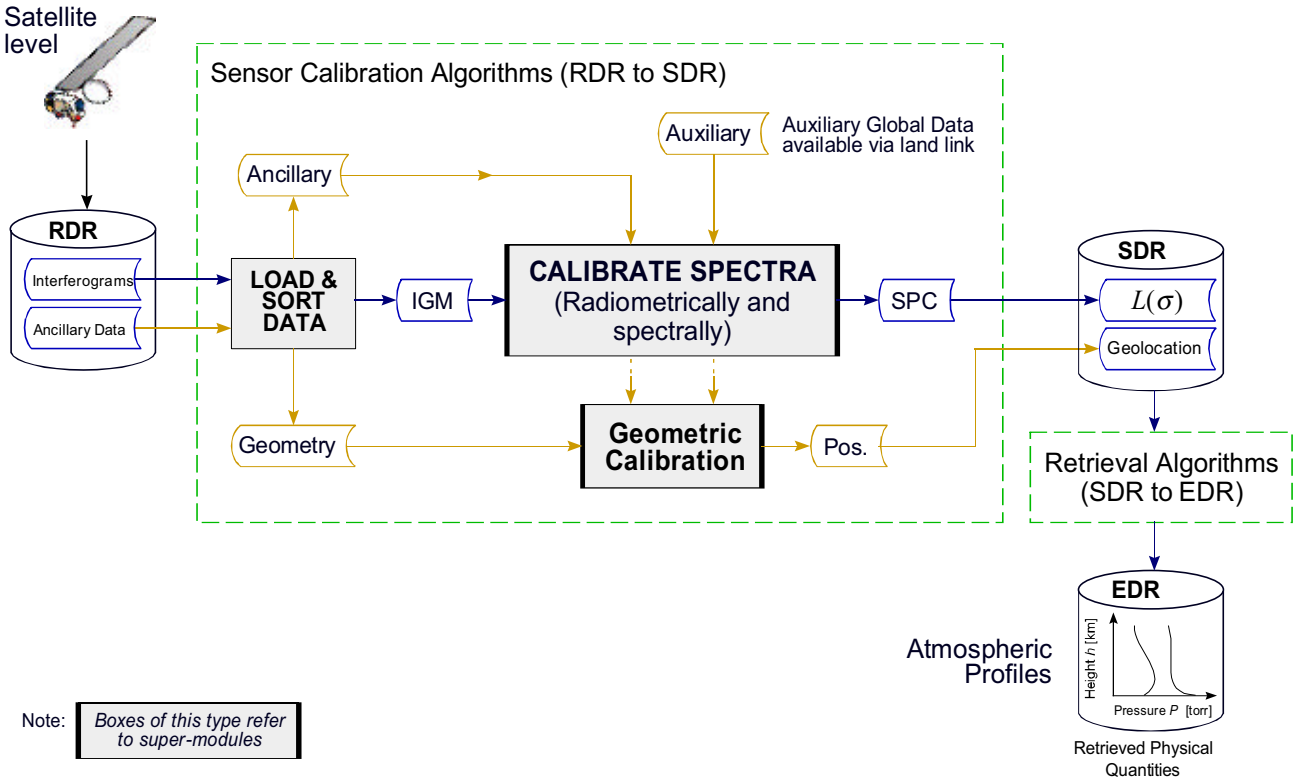

Figure 9: Ground Processing Data Flowchart

2.4 INTERFEROMETER MODEL

In this section we model a generic interferometer, with all relevant characteristics. The goal is to correctly describe the CrIS interferometer in order to define correctly the required ground segment SDR Algorithms.

If an interferometer was at a temperature of zero Kelvin, with perfectly symmetric (compensated) ports and with perfect electronics, particularly with perfect scanning speed then measured interferograms would be perfectly symmetric, resulting in a spectral signal with zero phase (real signal). Some of the real-life effects are hard to correct while some others are easier to avoid. Some effects can also be corrected by external complex calibration methods, like, for instance, the self-emission of the instrument.

The following sections present a comprehensive and logically ordered list of categories of the most significant ordinate errors that are found in conventional Fourier Transforms Spectroscopy (FTS). Each item in the list contains a brief description giving causes and consequences [RD 2].

Only the intrinsic errors caused by the instrument, technique or sample, are covered. Extrinsic errors induced by human actions are not considered. This discussion does not deal with error types that can be considered as “manipulation errors”, or “setup errors”, that can be avoided, like for example inappropriate sampling of the interferogram leading to spectral aliasing from above the Nyquist limit.

Knowledge of these error sources and their consequences is an essential pre-requisite for developing adequate calibration algorithms.

2.4.1 Instrument Phase

The reason for getting non-zero imaginary component out of the FT is that the FT interferogram is not mirror-symmetrical about the ZPD point ($x = 0$). The asymmetry originates from two different sources, either extrinsic or intrinsic. Extrinsic sources may arise from sampling errors for example. Intrinsic asymmetry may be due to wavenumber-dependent phase delays of either the optics or the electronics. Instrument phase, sometimes called “phase error” is more of a characteristic than an error as such.

Extrinsic

Electronic dispersion in the signal processing electronics (Sampling effects)

1– None of the IGM sampling positions coincides exactly with the proper position of zero path difference. This is generally the case and causes a phase linear in σ. This effect is easily corrected by calibration, if it remains constant during calibration and scene measurements. This incorrect location of center sample may be due to a poor algorithm or inadequate set of sample used for this (use of a reference white light).

2– If *fringe counts* are lost during the sweep, the effect is more dramatic and constitutes a phase errors. If fringe count errors occur at turn-around, corrective linear phase shifts can be applied to re-align measurements on the same reference. If a fringe count error occurs “in-sweep”, the last part of the interferogram will be shifted with respect to the first part of that interferogram. This effect results in a distortion of the current measurement that is very difficult to recover.

3– Also, reference metrology interferogram sampling may be different from infrared signal. This may cause *fractional FCE*, if for example metrology optical path changes slightly and suffers different temperature drifts not seen by IR optical path. This fact leads motivates the use of a coaxial IR and reference laser.

4– There are *sampling fluctuations* between each digitized point. Sampling jitter can be caused by metrology laser wavelength and/or amplitude fluctuations. Sweep speed may vary causing effective sampling jitter in systems where there exist delays between the IR signal and the metrology trigger signal. These errors result in instrument noise.

5– Errors due to differences between the optical paths in the interferometer used by the IR measuring beam and those used by the metrology laser radiation for monitoring the sampling of the interferogram.

It cannot be taken for granted that the monitoring beam optical surfaces are coplanar with the corresponding ones for the measuring radiation, as inserted elements and/or different coatings were involved. This type of error introduces constant phase shifts.

The electronics transfer function may be different from metrology laser and IR signal detectors. This causes mismatch delays between IR electrical response and ADC trigger signal.

5– Errors in the drive mechanism for OPD measurement.

6– Acquisition electronics introduce delays that vary with frequency (wavenumber).

Intrinsic

Optical dispersion in the beamsplitter-compensator subassembly

Because the overwhelming majority of BS coating materials is placed at one side of a dispersive substrate, the index of refraction of the substrate affects each wavelength in a different way. The ZPD of each monochromatic interferogram is at a different spatial location. This is the most common and better known source of phase error.

The role of the compensator plate is to attempt to compensate the dispersion effect of the beamsplitter. Its presence helps to compensate most of the phase errors introduced at the beamsplitter. The level of compensation depends on thickness matching.

Misalignments

Shear, Systematic IR misalignment, Interferometer divergence, Systematic OPD measuring Laser misalignment, Blur, Aberrations introduced by the interferometer collimator mirror can all contribute to the instrument phase error. If these effects remain constant between calibration and measurement, they will be cancelled out.

2.4.2 Other Signal Contributors

It is important to take into account other-than-scene contributors to the measured signal, mainly the instrument self-emission, also called self-radiance.

Beamsplitter

The *self-emission* constitutes an additional signal contribution to the observed scene. As it will be shown in Section 2.4.5, for any arbitrary measurement, the recorded interferogram is the sum of the interferogram of the viewed scene and the interferogram corresponding to the self-emission of the instrument. This last one is emitted principally by the beamsplitter, which undergoes phase shift different from the emission from the scene which goes through the whole optical chain of the interferometer [RD 3].

This effect is strongly temperature dependent. The out-of-phase contribution will depend on coatings.

Second port contribution

The second optical port of the interferometer is 180° out of phase with respect to the first port. The detected signal is the sum of the contribution from the two ports. For a perfectly compensated interferometer with a second port at 0 K, the observed signal would correspond to the pure scene, but in practice, the term corresponding to the instrument self-emission is not null. This explains IGM reversal when scene becomes colder than the terminator of the second port (complex calibration takes care of this effect).

Other parts of the instrument contributions

Can be grouped together, as long as they remain constant.

2.4.3 Instrument Line Shape

Traditionally, the spectrum $S(\sigma)$ of a finite interferogram was obtained by convolving the true spectrum with the “instrumental line shape” (ILS) function. This enabled a clear description of a measured lineshape in terms of a natural lineshape (NLS) due to physical line-broadening, the ILS representing the contribution of instrumental finite resolution and all other contributors like instrument misalignments, shear, blur, etc. Due to an ILS that depends significantly on wavenumbers, this approach is no longer valid for CrIS. A new approach is presented in this document.

2.4.4 Other Types of Errors

Includes non-uniform sampling intervals: two cases are possible:

1. repeatable, causing artifacts,
2. non-repeatable, causing noise.

Non-linearity

The detector, its analogue circuit or its ADC can suffer from non-linearity. This can result for example in a transfer function that can saturate with incoming flux. Non-linearity induces a global scaling and the apparition of spectral artifacts in the spectral domain.

Channel spectrum

Channel spectrum results from multiple reflections of the IR beam between the plane surfaces in the IR beam of spectrometer's optical path. Parasite reflections from the beam splitter and compensator substrate surfaces produce satellite interferograms, which may overlap the sampled region of the main interferogram. Inter-reflection effects such as the plane parallel sample itself or a liquid-cell window can induce the formation of resolvable interference fringes (channel fringes). This results in "ghost" interferograms or "echo peak" offset from the centerburst.

Skew rays

Skew rays give a different wavenumber scale for each off-axis ray. However, this does not shift ZPD.

Polarization

The polarization of the light from the scene interact with the polarization bias of the instrument and can cause radiometric errors.

Summary:

One of the biggest challenges is to move a mirror along at *constant velocity*. So in general this does not happen to the degree desired. Analog electronics can be designed to minimize the interaction of non-constant sweep speed and filter response. But it also has severe limitations of dynamic range and non-idealities like harmonic distortion, drift, non-well-behaved combination of gain and phase versus frequency. The use of broadband electronics gives frequencies of interest a "small range" in the bandwidth. This requires significant digital oversampling. Digital processing can be done (in some cases) at high precision and dynamic range.

Another big challenge is to move the mirror without changing the modulation: i.e. maintain interferometric alignment overscan. There is very little correction opportunity for this. So make it well mechanically (DA, cube corners, etc).

Each of these problems, sometimes grouped together, will be associated with a clear solution throughout the document.

2.4.5 Interferometer Modeling Equations

According to the comments made in Section 2.4, the various instrument phase contributions can be grouped in given terms, and the interferometer system can finally be viewed as follows:

1. The equivalent phase dependency of the observed scene, corresponding to the incident photon flux through the FOV of the instrument: $e^{i\phi^{ext}}$. This term combines all the phase effects proportional to the amplitude of the measured signal.
2. The phase dependency on the instrument itself, corresponding to all the light *not* coming through the scanned FOV, like the thermal emissions of the various surrounding parts of the interferometer (instrument contribution), dispersion effects and thermal emission of the beamsplitter, electronics effects, etc.: $e^{i\phi^{in}}$ (*in* superscript for *in*side or *in*strument).

   Corresponds to the sum of all contributors, summed vectorially
3. Amplitude functions proportional to each observed scene: A^x (real functions)

This analysis properly accounts for the situation in which the phase response for radiance from the instrument itself differs from the one for radiance from an external source. This model also effectively takes care of the emission of the various parts of the interferometer. The main mechanism responsible for this dual phase interferometer response is emission from the beam splitter [RD 3].

These terms indicate that the resulting phase of deep space, calibration BB, and scene measurements may vary substantially. Note: all these terms are functions of wavenumber. The following figure summarizes the situation:

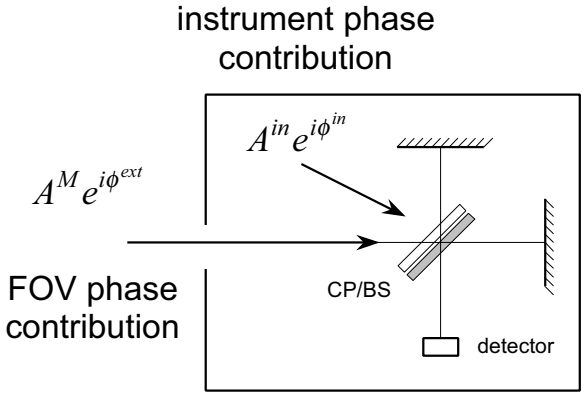

Figure 10: Phase dependencies in an interferometer

According to this model, and the notation given in Section 1.6, a given measurement can be described as follows:

$$\begin{aligned}\tilde{S}^{M} &= \underbrace{A^{M}e^{i\phi^{ext}}}_{\text{scene contribution}} + \underbrace{A^{INT}e^{i(\phi^{INT}+\delta_1)} + A^{BS}e^{i(\phi^{BS}+\delta_2)}}_{\text{instrument contribution}} \\ &= A^{M}e^{i\phi^{ext}} + A^{in}e^{i\phi^{in}}\end{aligned} \tag{6}$$

where the complex raw spectrum $\tilde{S}^M$ is built from the scene amplitude A^M affected by the sum of the various interferometer contributions $e^{i\phi^{ext}}$, on which the instrument contribution is added, composed the amplitude A^{INT} multiplied by phase $e^{i\phi^{INT}}$ plus the beamsplitter amplitude contribution A^{BS} multiplied by phase $e^{i\phi^{BS}}$. When the BS temperature remains constant (or negligible), the second and third term are combined vectorially and are considered together as $A^{in}e^{i\phi^{in}}$ to simplify analysis.

If the observed scene is much colder than the instrument ($T^C \ll T^{in}$ and sufficient high σ), then $A^C \ll A^{in}$, suggesting that this measurement can be considered as the instrument offset itself. $\tilde{S}^C \approx A^C e^{i\phi^{ext}}$. This is true for spaceborne instrument looking at the deep space ($\approx 4\ K$) as the cold reference.

Following these assumptions, the three following basic measurements can be modeled as:

Cold reference: $\tilde{S}^C = A^{in}e^{i\phi^{in}}$

Hot reference: $\tilde{S}^H = A^H e^{i\phi^{ext}} + A^{in}e^{i\phi^{in}}$

Scene Measurement: $\tilde{S}^S = A^S e^{i\phi^{ext}} + A^{in}e^{i\phi^{in}}$

2.5 CRIS CHARACTERISTICS

This section goes through some of CrIS characteristics related to the SDR Algorithms.

2.5.1 Double-Sided Interferogram Measurements

Interferograms can be recorded with the optical path difference x varying from a little less than 0 to +MPD (single-sided), or from –MPD to +MPD, as shown in Figure 11.

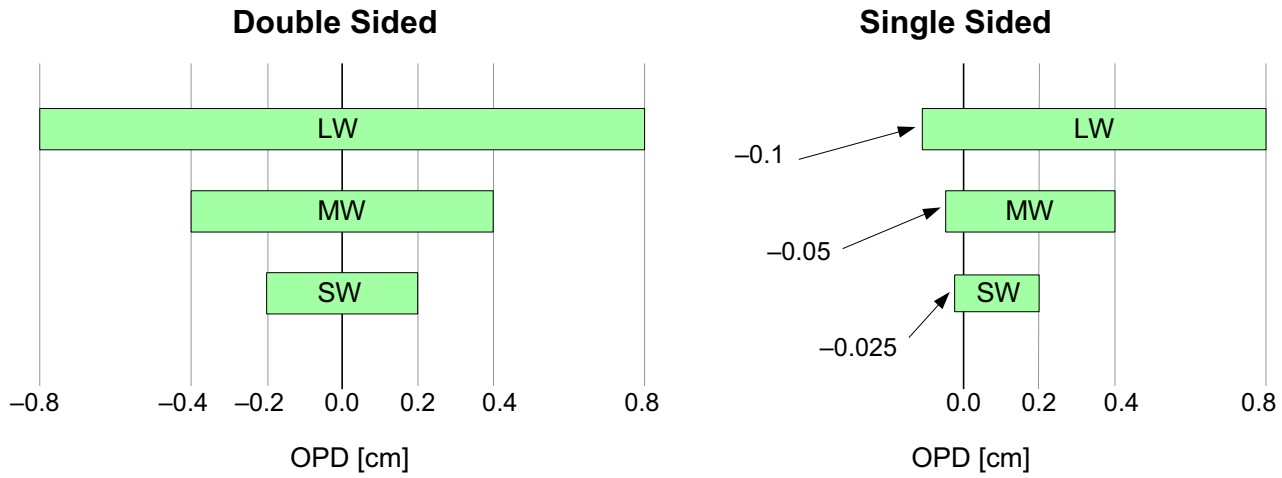

Figure 11: Double-sided versus single-sided interferograms

In theory, both halves of a sampled interferogram contain the same information, and if only a limited total path difference variation is mechanically available, only one half of the interferogram can be measured, yielding to a lower data rate. But there are in fact at least four major advantages to symmetric sampling of the interferogram [RD 4]:

1. The sensitivity of line positions to the accuracy of the phase correction is drastically reduced. For one-sided interferograms, the local instrument lineshape has as its real part the usual $2MPD\,\mathrm{sinc}(2MPD\sigma)$; but unlike the symmetric interferogram it also has an equally large asymmetric imaginary part $2MPD\sin(2\pi\ MPD\sigma)\,\mathrm{sinc}(2MPD\sigma)$. Even a very small phase error is enough to rotate a portion of this imaginary part into the real plane, producing an asymmetric apparatus function in the final spectrum. Since the phase error is often a function of wavenumber, this produces a varying apparatus function and hence a variable wavenumber scale. With two-sided interferograms, the only imaginary part comes from any slight asymmetries in the interferogram itself, and these are normally very much smaller; the sensitivity to phase error is proportionally reduced.

2. Double-sided interferogram naturally reject the linear source intensity variations.

3. The source noise of the measurement is reduced because of the increasing the sampling frequency.

4. Double-sided interferograms have a major advantage over single-sided ones for an application like atmosphere emission measurements by the CrIS instrument. As opposed to sun occultation measurements for example, emission measurements generate larger ZPD

regions, that are harder to represent in single-sided mode. Double-sided interferograms are more appropriate as they offer better phase definition, since the information is spread equally on each side of the ZPD. There can be a better control on the quality of the phase correction without any hypothesis on the ZPD neighborhood. It assures that the phase correction will be correctly performed, even taking care of slight asymmetries.

5. All path differences are sampled symmetrically about a common mean time, so that, to first order, all frequencies components refer to the same mean epoch. This results in considerably more accurate line profiles in many situations where there is a monotonic variation in source intensity during an observation. Examples of such sources include astronomical sources near the time of rising or setting (i.e. rapidly changing air mass).

The following discussions in the present document make the assumption that interferograms will be recorded double-sided, and the algorithms will process them in full width.

Characteristics

- Both the single-sided and the double-sided approaches have same spectral resolution for a fixed MPD,
- Single-sided has lower data rate (5/8 of baseline double-sided),
- Both have the same NEdN if sweep time remains the same,

→ Double-sided provides better phase calibration of instrument.

→ Double-sided is less sensitive to sweep asymmetries of hardware.

→ With double-sided interferograms, the sensitivity of line positions to the accuracy of the phase correction is drastically reduced.

2.5.2 CrIS Spectral Bands

There are three infrared spectral bands defined for the CrIS sensor: the Long Wave (LW), the Middle Wave (MW), and the Short Wave (SW). The sampling interval is defined by the 1550 nanometer laser metrology wavelength. The spectral limits corresponding to these bands and the required on-axis unapodized spectral resolution ($1/(2\ MPD)$) in each CrIS band are given in Table 2 (SRD 3.2.1.4). The CrIS interferometer sweeps difference optical path length is 0.8 cm. This results in the basic resolution of 0.625 cm^{-1}. The other 1.25 and 2.5 cm^{-1} resolutions are simply obtained by sampling a smaller number of points along this same optical path, resulting in effective MPDs of 0.4 and 0.2 cm.

Table 2: CrIS Specifications

Band	Spectral range [cm^{-1}]	Spectral range [μm]	Band width [cm^{-1}]	Resolution $\Delta\sigma$ [cm^{-1}]	MPD [cm]
LW	650 – 1095	15.4 – 9.1	445	0.625	0.8
MW	1210 – 1750	8.3 – 5.7	540	1.25	0.4
SW	2155 – 2550	4.6 – 3.9	395	2.5	0.2

Figure 12 presents each band with their array constituents. 127 oversample points are used to fill 255 tap FIR pipeline (see Section 2.2.2). The OPD lengths are fixed to accommodate the Prime

Factor FFT with decimated complex data (see Section 2.6.1). Two spare decimated samples are kept to accommodate ZPD uncertainty.

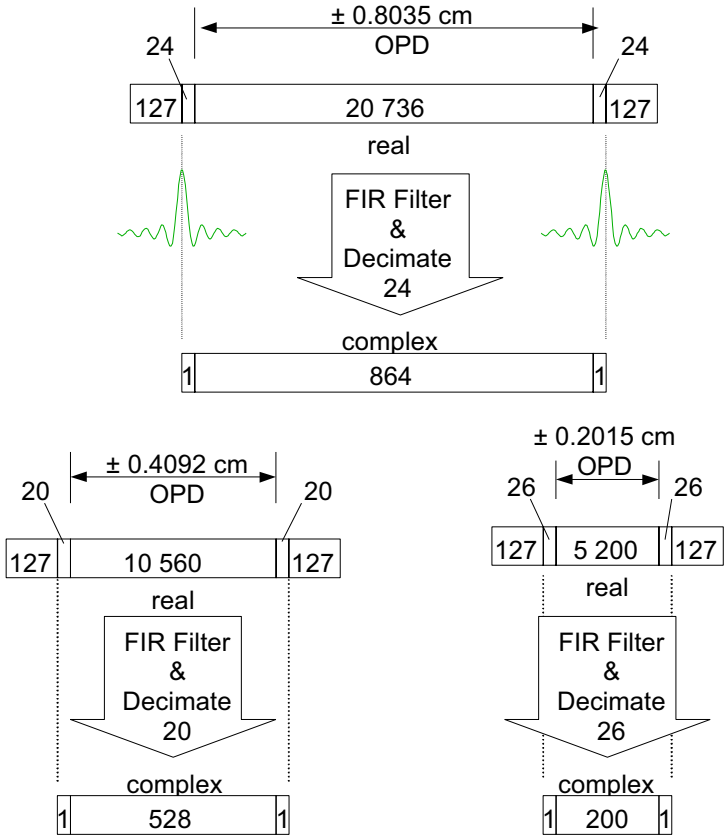

Figure 12: Long, Mid, and Short Wave IR bands

2.5.3 CrIS Field of Regard

The CrIS instrument is designed to observe the ground with an instantaneous field of view which maps to a nadir footprint of 14 km on the ground from an altitude of 833 km (corresponding to a FOV = 16.8 mrad). Figure 13 shows the Field of Regard definition (SRD 3.2.1.19)

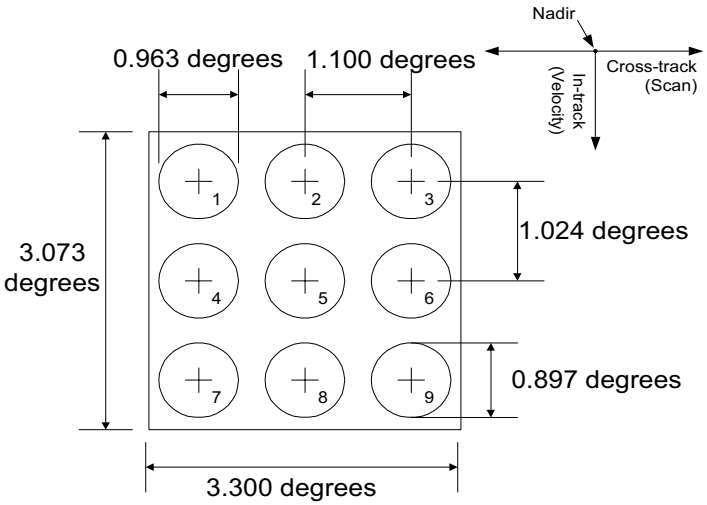

Figure 13: Field of Regard definition

2.5.4 CrIS Measurement Sequence

In order to properly calibrate the radiometric output from the instrument, it is also necessary to acquire regularly, during the course of the mission, two additional types of measurements of well-defined targets. The first one is done with an internal high-precision calibration blackbody, the internal Calibration Target (ICT). For the second measurement, the instrument is simply looking at the deep space (DS) that represents a source of low (negligible) IR radiance where the measured interferogram is related to self-emission of the instrument. This offset will be subtracted from scene measurements during on-ground data processing. These two calibration measurements will be performed once every 8 seconds in order to account for changing self-emission of the instrument due to temperature variations in the orbit.

A typical measurement scan sequence consists of 34 interferometer sweeps (see Figure 14), including 30 earth scenes plus 2 deep space and 2 ICT measurements (these numbers include both forward and reverse sweeps). One scan of the CrIS sensor will take about 8 seconds.

- The instrument can perform a new measurement (sweep) every 200 ms:
  7 ms for pointing and 33 ms for repositioning.
- A new cycle (scan) is repeated every 8 seconds:
  4×200 ms + 1.2 s + 30×200 ms.
- Each scan is comprised of 918 interferograms
  2 (sweeps) $\times$ (2 + 15) FOVs $\times$ 3 bands (detectors) $\times$ 9 pixels

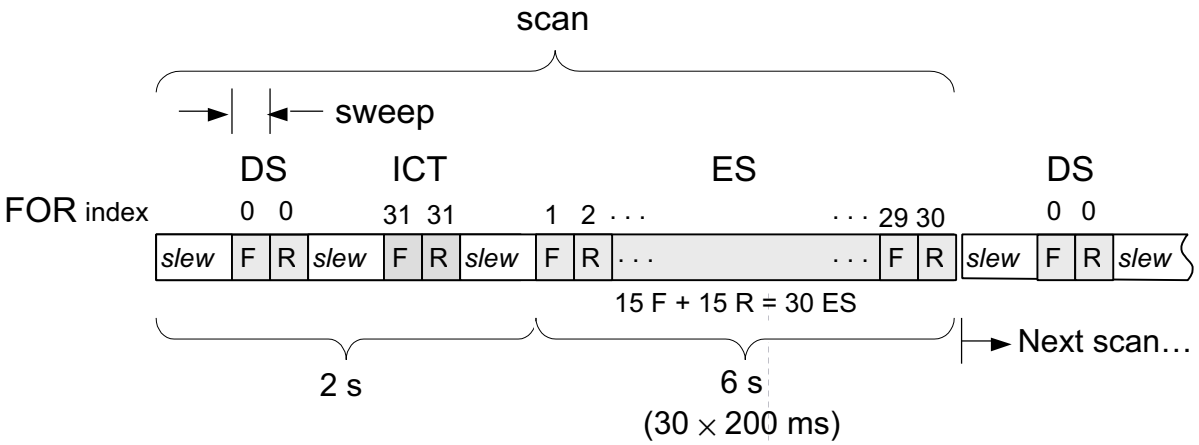

Figure 14: CrIS Measurement Sequence

The azimuth angle will be adjustable during an elevation scan sequence within a limited range, but not during an interferometer sweep. There is an image motion compensator: scan mirror that moves backward so that the spot defined on earth begins at the beginning of the sweep (saw teeth motion).

2.5.5 CrIS Signal Processing

At the satellite level, or space segment, the observed radiance is transformed into a modulated signal by the interferometer. This IR signal is detected by an HgCdTe detector and sampled with a metrology wavelength of 1550 nm. This electrical signal is then amplified and converted to a digital signal by an ADC. Taking into account guard bands, the total number of measured sampling pulses per sweep is given in the second column of Table 3, while the third columns lists the number of points strictly corresponding to the OPD sweep. Measured raw data points are then filtered and decimated to limit the bandpass in order to lower the transfer data rate. The decimation factor used in each band depends on its bandwidth. The fourth and fifth column of Table 3 list the decimation factor that can be used in each channel (see Section 2.2.2) and the resulting number of points.

A set of nominal retrieval spectral channel wavenumbers will be provided as an output by the SDR Algorithms. Radiance data from all detectors will be interpolated to this standard set of spectral channel wavenumbers for retrieval studies and other EDR validations (SRD 3.2.1.21-1). The sixth column of Table 3 gives the number of bins delivered to the EDR algorithms.

Table 3: CrIS signal dimensions

Band	Total sampling pulses per sweep	OPD samples	Decimation factor DF_b	Decimated points N_b*	Output bins
LW	21 038	20 736	24	864	713
MW	10 854	10 560	20	528	433
SW	5 506	5 200	26	200	159

* these numbers do not include an additional 2 overscan points

2.6 SIGNAL REPRESENTATION

All signals are composed of their ordinate data points array, in conjugation with a definition for their associate abscissa, together with additional relevant parameters. All spectral vector signals start at 0.0 cm^{-1}

For example, the numerical signal of a given band is composed of:

IGM:

$I_b^X[m]$	ordinate data points array.
m	spatial index, range $0 \le m \le N_b^X - 1$
N_b^X	total number of points of the array.
Δx_b^X	sampling interval, or spacing between spatial points of the array
$flags$	various flags representing the integrity of the signal
n^{ZPD}	the position of the undecimated ZPD point (TBR)

SPC:

$\widetilde{S}_b^X[n]$	ordinate data points array.
n	spectral index, range $0 \le n \le N_b^X - 1$
N_b^X	total number of points in the array.
σ_{0b}^X	spectral range lower limit (wavenumber origin) of the array.
$\Delta\sigma_b^X$	spectral interval, or spacing between spectral points of the array.
$flags$	various flags representing the integrity of the signal
n^{ZPD}	the position of the undecimated ZPD point (TBR)

2.6.1 Array dimensions

It has been chosen to process signals at *full resolution* (lengths non powers of 2) with *no zero padding* for the following reasons:

1. Incoming signals have small dimensions (less than 1000 points)
   - Dimensions can be adjusted to match lengths that are factor of small prime numbers. Thus, the processing of the Fourier transform can be executed on these signals by fast algorithms (FFT) faster than the corresponding zero-padded case.
   - Working with coarse resolution (smaller dimensions than the nominal array dimensions) would attain no real gain in speed, and the increase of processing complexity would waste the advantage.
2. Second, the processing at the original signal dimension without zero-padding is easier since:
   - It limits spectral bin mixing and avoids introducing correlation between spectral points that could be detrimental to the Level 2 algorithms, since the noise of each bin is spread around neighbors by the interpolation done by zero-padding. The effect of zero-padding causes the covariance matrix in the calibrated scene spectra to have non-zero off-diagonal elements. Otherwise the covariance matrix would have to be evaluated so that the EDR algorithms could use the information.
   - Border effects are reduced.
   - No constant DC offset removal is required to match the zero-offset of the padding in order to avoid discontinuities in the interferogram signal.

In order to compute the SDR Algorithms ground processing as fast as possible, the Prime Factors Algorithm (PFA) [RD 5 and RD 6] is suggested for the computation of Fast Fourier Transforms with non powers of 2 array dimensions.

Array dimensions that are multiple of small prime factors can be processed very rapidly by the PFA FFT, even faster than optimized standard powers of 2 FFTs, for dimensions smaller than the next power of 2 available (see Appendix 9.1.2). For example, a FFT of 560 points can be processed 60% faster by the PFA FFT, compared with a traditional optimized FFT on a vector of 1024 points, that is the next power of 2 larger than 560.

According to the latest official specifications for the CrIS instrument, the Data Rate Budget for two-sided interferogram is summarized in Table 4 through Table 6 with respect to the number of samples transmitted to ground. The values of N_{LW} = **864**, N_{MW} = **528**, and N_{SW} = **200** seem to be good choices, as they can be executed quite fast and still remain very compatible with the presently defined band widths. With this particular choice of prime factor dimensions, we get 0.52 ms with the PFA algorithm compared to the 0.87 ms obtained with optimized routines for powers of 2 algorithms, meaning that we can save 40% of processing time by using prime factor algorithm with this particular array dimension choice.

Table 4: Long Wave array dimensions

CrIS Data Rate Budget	**LW band** **min max**
Wavenumber	650 1095
Effective OPD [cm] (radiometric)	±0.8035
Sampling interval (metrology laser $\lambda/2$)	775 nm
Sampler per IGM over OPD interval	20736
Total measured samples per IGM	21038
Decimation factor DF_b	24
Samples per IGM / DF_b = PFA dimension (2^5x3^3)	**864**
RDR input spectral bins	866
SDR output spectral bins	713
Percentage of used band	82.3%

Table 5: Middle Wave array dimensions

CrIS Data Rate Budget	**MW band**
Wavenumber	1210 1750
Effective OPD [cm] (radiometric)	±0.4092
Sampling interval (metrology laser $\lambda/2$)	775 nm
Sampler per IGM over OPD interval	10560
Total measured samples per IGM	10854
Decimation factor DF_b	20
Samples per IGM / DF_b = PFA dimension (2^4×3×11)	**528**
Output spectral bins	530
SDR output spectral bins	433
Percentage of used band	81.7%

Table 6: Short Wave array dimensions

CrIS Data Rate Budget	**SW band**
Wavenumber	2155 2550
Effective OPD [cm] (radiometric)	±0.2015
Sampling interval (metrology laser $\lambda/2$)	775 nm
Sampler per IGM over OPD interval	5200
Total measured samples per IGM	5506
Decimation factor DF_b	26
Samples per IGM / DF_b = PFA dimension (2^3x5^2)	**200**
Output spectral bins	202
SDR output spectral bins	159
Percentage of used band	78.7%

With the attainable execution speeds, the FFT computation is not really a bottleneck for the SDR Algorithms. More complex operations influence the total computation time, like convolution operations required for the self-apodization removal or matrix multiplication for the self-apodization removal. This means that with fast C language algorithms, the need to execute the FFTs with the help of DSPs does not seem to be a necessity at the current time of algorithm development. This fact, together with the simplifications obtained with the use of non-powers of 2 array dimensions, significantly simplifies the SDR Algorithms. This simplified processing increases computing speed and avoids the introduction of supplementary errors. Table 7 gives the processing times for four of the fastest FFT routines described in Section 9.1.3.

Table 7: Array dimensions and computing times (PII, 350 MHz)

FFT Points	Prime Factors Decomposition	Execution time [ms]			
		Routine 1	Routine 2	Routine 3	Routine 4
189	$3^3 \times 7$		0.27	0.26	0.20
190	$2 \times 5 \times 19$		0.36	0.33	0.30
192	$2^6 \times 3$		0.21	0.15	0.21
195	$3 \times 5 \times 13$	0.06	0.34	0.31	0.26
196	$2^2 \times 7^2$		0.29	0.26	0.23
198	$2 \times 3^2 \times 11$	**0.06**	0.29	0.28	0.24
200	$2^3 \times 5^2$		0.30	0.21	0.22
203	7×29		0.42	0.49	0.39
204	$2^2 \times 3 \times 17$		0.31	0.33	0.28
207	$3^2 \times 23$		0.34	0.42	0.36
208	$2^4 \times 13$	0.06	0.29	0.27	0.29
518	$2 \times 7 \times 37$		1.18	1.54	1.27
520	$2^3 \times 5 \times 13$	0.16	0.92	0.80	0.75
522	$2 \times 3^2 \times 29$		1.01	1.28	1.03
525	$3 \times 5^2 \times 7$		1.08	0.81	0.64
527	17×31		1.25	1.61	1.28
528	$2^4 \times 3 \times 11$	**0.13**	0.77	0.71	0.71
529	23^2		1.18	1.55	1.24
532	$2^2 \times 7 \times 19$		0.97	1.08	0.91
539	$7^2 \times 11$		1.07	1.02	0.83
540	$2^2 \times 3^3 \times 5$		0.79	0.69	0.63
544	$2^5 \times 17$		0.87	0.86	0.86
546	$2 \times 3 \times 7 \times 13$	0.18	0.99	1.00	0.80
840	2^3 x 3 x 5 x 7	0.23	2.00	1.23	1.27
845	5 x 13^2		2.31	1.86	1.58
847	7 x 11^2		2.46	1.82	1.52
850	2 x 5^2 x 17		2.11	1.76	1.45
855	3^2 x 5 x 19		2.17	1.97	1.49
858	2 x 3 x 11 x 13	**0.33**	2.39	1.85	1.50
864	2^5 x 3^3		1.71	1.03	1.28
867	3 x 17^2		2.50	2.19	1.86
870	2x 3 x 5 x 29		2.33	2.29	1.89
874	2 x 19 x 23		2.56	2.52	2.12
875	5^3 x 7		2.15	1.48	1.25
880	2^4 x 5 x 11	0.28	1.95	1.36	1.43

2.6.2 Data ordering

For the storage of numerical signals, array data vectors are stored with *zero origin*, meaning that the points ordering is assumed “normal” (as opposed to the “bit reversed" sometimes seen), that is defined as follows:

If input data is a time series with linear time spacing Δx:

$$x_i = \Delta x\,[0..N-1] \tag{7}$$

then the corresponding frequencies after execution of the FFT are:

$$\sigma_i = \Delta\sigma \times \left([0..N/2],-[N/2..0[\right) \tag{8}$$

i.e., the first half of the result corresponds to positive increasing frequencies; the second half of the result corresponds to negative frequencies (decreasing in absolute value). The zero-frequency ZPD point is at the beginning of the vector (zero index).

Even if this representation is a little less “visually” attractive than vectors with the origin at the center of the array (normal ordered vectors must be swapped before display of the whole range of negative and positive frequencies), it is more straightforward for numerical implementations, as it requires no extra processing only for display effects.

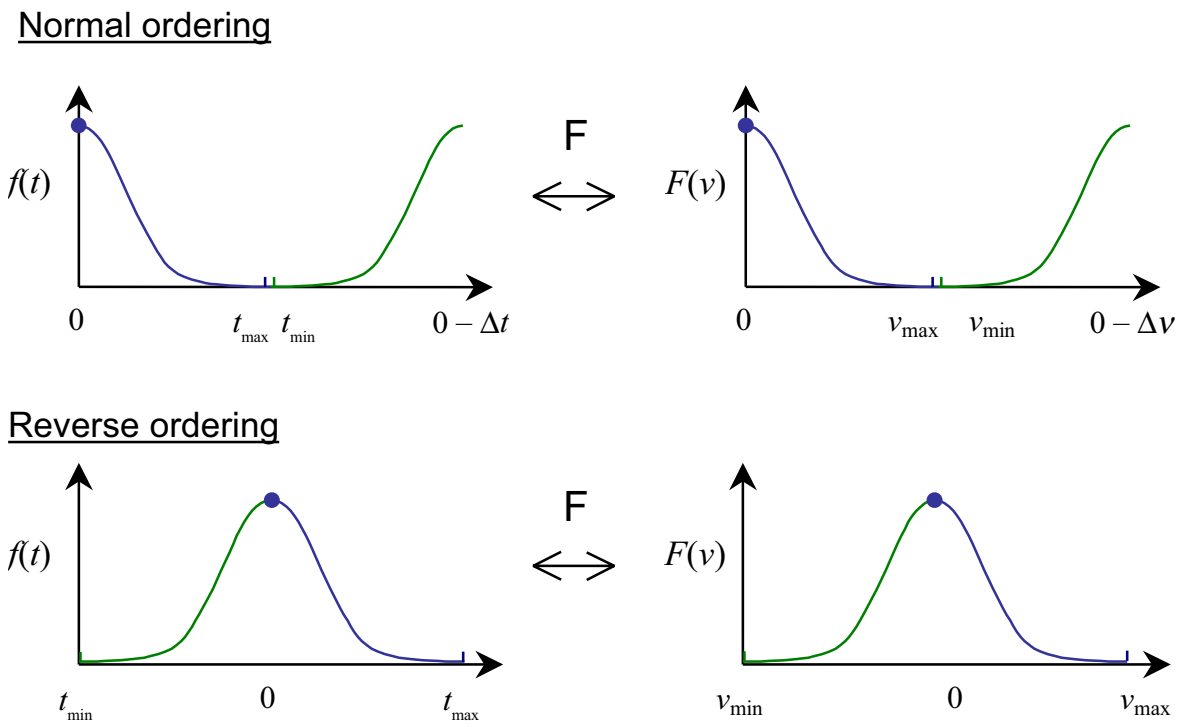

Figure 15: Numerical vectors data ordering

3. SPECIAL CONSIDERATIONS

This section presents the discussion of various effects that need to be corrected, namely spurious interferogram spikes and fringe count errors. The need to align data to a user's grid is also discussed.

3.1 NON-LINEARITY CORRECTION

Non-linearity levels are expected to be low enough with the use of PV detectors so that no non-linearity correction scheme is necessary.

3.2 SCAN MIRROR POLARIZATION COMPENSATION

The CrIS scan mirror is used to select calibration and scene targets. Rotating the scan mirror does the selection. By design, the CrIS uses a barrel-roll scan mirror (see Figure 16), so the angle of reflection θ at the surface of the mirror remains constant for all types of viewed scenes.

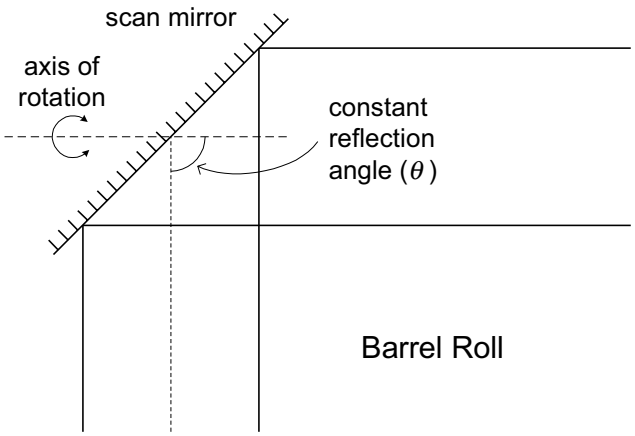

Figure 16: Barrel-roll scanner type

Reflection on an inclined surface always induces some polarization. Since the incident angle in constant, the polarization induce by the scan is constant too. However, its plane rotates with the barrel roll angle. Since the interferometer itself is expected to create a significant polarization, this will create a modulation of the signal as the scan mirror rotates. This effect will be corrected in the radiometric calibration equation by the introduction of a polarization operator. This operator is computed on ground from analysis and/or measurement during pre-flight characterization and testing. It is produced with the same spectral axes as the ones requested for the calibrated spectra in each band. Therefore no interpolations are performed with respect to the spectral axis during the application of this correction term.

3.3 FRINGE COUNT ERROR HANDLING

A fringe counting system using a reference laser source within the interferometer subsystem, determines the sampling. If, for any reason, a fringe is lost, then the current and the following interferograms are shifted with respect to previous ones. This means that the phase of subsequent measurements will be affected and if they are calibrated using a gain or offset measurement taken before the occurrence of the fringe loss, then errors will be introduced into the final spectrum. The SDR Algorithms include a method for detecting and correcting fringe losses by analyzing the residual phase of interferograms.

3.3.1 Phase analysis

With an *unfiltered and undecimated interferogram*, the fringe count error detection could be done directly on the interferogram by looking at the position of the observed ZPD.

In the best cases, when the scene contains some sort of continuous background, the ZPD position can be easily determined (one just identifies the maximal IGM observation). However, if the scene is sensibly different from a blackbody distribution, containing only sparse spectral lines for example, the strong ZPD point is no longer an available reference. Moreover, if the signal suffers from strong phase dependencies to wavenumber (see Section **2.4.1**), one could have a hard time trying to identify the true ZPD point as interferometric frequencies are spread around a larger area. Alternatively, FCE handling could be based on IGM center of gravity computation. This could be done with an auto-correlation to extract its ZPD position with sub-point precision. However, this approach is more complicated and computer intensive.

When the interferogram is *filtered and decimated*, as it is the case for CrIS, the ZPD region is further affected and the maximum intensity point can be difficult to identify. In addition, a shift by a number of points smaller than the decimation factor will produce only a small shift of the decimated interferogram. For example, the shift of a 20 times decimated interferogram will be 1/20 the effective sampling interval if the fringe error is one point. Therefore, the monitoring of the ZPD position of the decimated interferograms is not a sensitive approach to detect fringe count errors for CrIS.

The approach selected for FCE detection consists in an analysis of the linear wavenumber-dependent residual phase that comes out from comparing signals relatively to each other (ES, ICT and DS). When the OPD axis definition of the actual measurement is the same as the current gain and offset used for radiometric calibration, then the residual phase should be zero. A shift in one of them with respect to the two others produces a phase error increasing linearly with wavenumber. This can be seen using the “shift theorem”. This is explained in further details in Section 3.3.3.

As the phase extraction process must mathematically be processed in the spectral domain, the FCE detection is performed on complex spectra. The correction is done by the multiplication with a linear shifting phase, enabling the correction of fractional point shifts in the corresponding interferograms.

3.3.2 Chosen approach for detection and correction

Fringe count errors (FCE) can occur anytime. First, they can occur at turnaround between successive IGMs: the effect of such FCEs is to shift all measurements following the error by h points. If this remains uncorrected, problems will arise because all the measurements involved will not have the same sampling positions. A stable instrument is not expected to suffer from this type of error.

On the other hand, if a cosmic ray falls on the metrology system (detector, electronics, etc.), a spike could be induced and the metrology system could loose one or more fringes. This type of error can occur anywhere in the IGM. The effect of “in-sweep” fringe errors is twofold: first it shifts the last part of the interferogram in which the error occurs with respect to the first part of that interferogram.

The last effect results in a distortion of the current measurement that is very difficult to recover, in particular for scene measurements. For the moment, no correction is foreseen for that type of error. The philosophy adopted for fringe count errors detection and correction is to try to correct each affected signals, and quantify the result in order to discard unrecoverable ones. The result from the calibration process (imaginary part) will show a problem, and the complex scene will have to be discarded in order to avoid corrupting subsequent calibrated spectra. The second effect is that all subsequent measurements will be shifted with respect to any previous measurements. This latter effect is the same as if the error would have been at the turn-around. In practice, this type of FCE is expected to occur very infrequently during measurements.

For all types of measurements, the fringe count reference is the *actual* Earth scene measurement. When a FCE occurs for a given sweep with respect to the previous sweep, the associated average ICT and DS need to be shifted to match the current fringe count position, in order to match all spectra that follow. This has the advantage that all subsequent measurements will need no correction. The fact of aligning moving averaged deep space (DS) and warm blackbody (ICT) references is easier and less error inducing because they essentially are smooth blackbody distributions. This limits the error accumulation on the scene.

The following summarizes the conditions under which the FCE handling will be performed:

Because the phase is not strictly the same for forward and reverse sweeps, the fringe count error detection and correction is done independently for the two sweep directions.

Because each detector measures signals from a common sweep, FCEs affects equally each pixel: the current baseline is to compute detection on only on the central pixel in a given FOR. If a problem is encountered, the detection is redone for other pixels for confirmation. This approach with majority vote adds robustness against noisy single measurements, periodic bad IGMs, or failed detectors. However, correction is necessary to be performed on all pixels.

Since FCEs can occur in all types of measurements done by the CrIS instrument, the detection and correction approach is slightly different depending if the signal is a scene or a calibration measurement.

ZPD Synchronization

Each time the instrument is powered on or initialized, the interferogram sampling window position is re-established. The ZPD position, due to sampling noise or spectral dispersion, is subject to inaccuracies. This shift of the sampling window is not critical since it can be considered as a fringe count error and is automatically detected and corrected during the radiometric characterization and radiometric calibration process. In principle the data can be used no matter where the sampling window position is. The amount of drift can be almost arbitrary, as the IGM is sampled double-sided. Therefore, no special care has to be taken in order to avoid loosing the ZPD point, like it would be the case for single-sided IGMs for example.

3.3.3 FCE detection

The shift theorem states that a shift of a integer points in the undecimated interferogram domain corresponds to a linear phase shift in the spectrum domain:

$$I(x-a) \leftrightarrow S(\sigma)\, e^{-2\pi\, i\, a\, \sigma} \tag{9}$$

Based on this relation, the residual phase of a calibrated spectrum is the phase corresponding to the initial shift, all other phase contributors having been cancelled out by the calibration process itself (see Section 4.2). Therefore, a linear regression on the residual phase of the calibrated spectrum reveals the shift due to a fringe count error on the observed interferogram (see Figure 17).

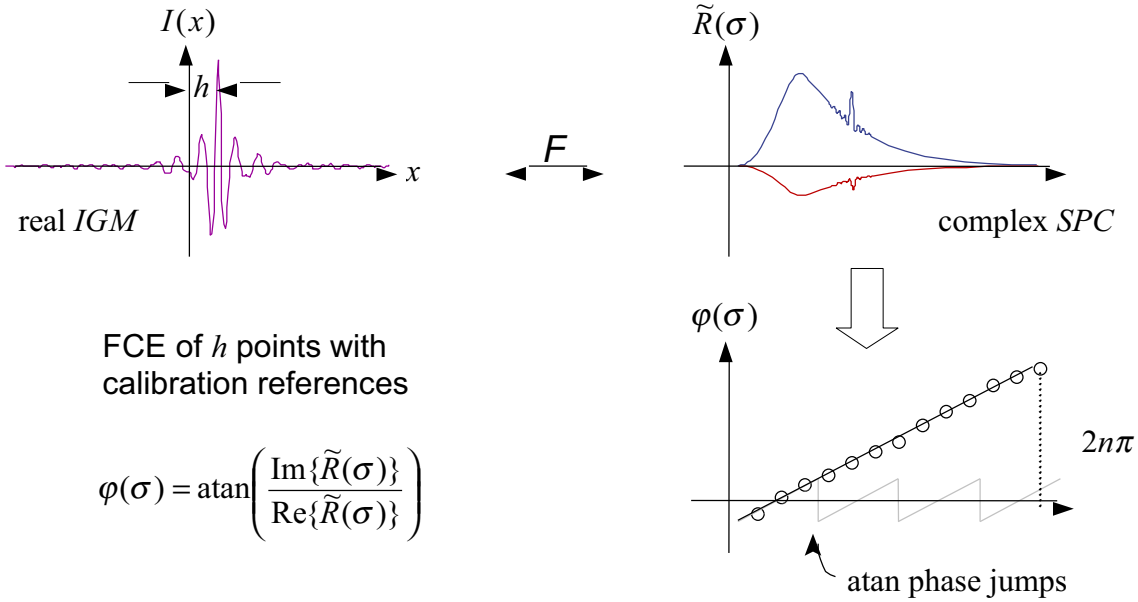

Figure 17: FCE detection scheme

In practice, this phase shift is not measured in absolute way but in a relative way to a reference spectrum. For reference calibration signals, detection is done with respect to the *previous equivalent mean* measurements. As the current and previous spectra are equivalent (always looking as the DS or at the same reference blackbody) the instrument phases are cancelled out, their ratio can be used to compute the phase extraction function $\widetilde{R}(\sigma)$ needed for linear phase extraction (here $\phi_h = -2\pi\, h\, \lambda_L$):

$$\widetilde{R}(\sigma) = \frac{\widetilde{S}^C_{b,p,d}(\sigma)}{\left\langle \widetilde{S}^C_{b,p,d} \right\rangle(\sigma)} = \frac{e^{i\phi_h}\left(0 + A^{in} e^{i\phi^{in}}\right)}{0 + A^{in} e^{i\phi^{in}}} = e^{i\phi_h} \tag{10}$$

Same thing for hot reference:

$$\widetilde{R}(\sigma) = \frac{\widetilde{S}^H_{b,p,d}(\sigma)}{\left\langle \widetilde{S}^H_{b,p,d} \right\rangle(\sigma)} = \frac{e^{i\phi_h}\left(A^H e^{i\phi^{ext}} + A^{in} e^{i\phi^{in}}\right)}{A^H e^{i\phi^{ext}} + A^{in} e^{i\phi^{in}}} = e^{i\phi_h} \tag{11}$$

As the measured earth scenes are different one to another, the previous scene can not be used as a reference as it is done with calibration measurements. Earth scene measurements $\widetilde{S}^{es}(\sigma)$ must be

processed in a particular way in order to isolate only the linear fringe count dependency. The following equations summarize the process:

$$\widetilde{P}(\sigma) = \frac{\widetilde{S}^S}{\langle \widetilde{S}^H \rangle - \langle \widetilde{S}^C \rangle} = \frac{e^{i\phi_h}(A^S e^{i\phi^{ext}} + A^{in} e^{i\phi^{in}})}{(A^H e^{i\phi^{ext}} + A^{in} e^{i\phi^{in}}) - A^{in} e^{i\phi^{in}}} = e^{i\phi_h}\left[\frac{A^S}{A^H} + \frac{A^{in}}{A^H} e^{i(\phi^{in} - \phi^{ext})}\right] \tag{12}$$

$$\widetilde{Q}(\sigma) = \frac{\langle \widetilde{S}^C \rangle}{\langle \widetilde{S}^H \rangle - \langle \widetilde{S}^C \rangle} = \frac{A^{in}}{A^H} e^{i(\phi^{in} - \phi^{ext})} \tag{13}$$

$$\widetilde{R}(\sigma) = \frac{\widetilde{P}(\sigma)}{\sqrt{|\widetilde{P}(\sigma)|^2 - \mathrm{Im}\{\widetilde{Q}(\sigma)\}^2} + i\ \mathrm{Im}\{\widetilde{Q}(\sigma)\}} = e^{i\phi_h} \tag{14}$$

Once the spectral phase extraction function $\widetilde{R}(\sigma)$ is known, its associated linear phase shift can be computed with the following relation:

$$\varphi(\sigma) = \mathrm{atan}\left\{\frac{\mathrm{Im}\{\widetilde{R}(\sigma)\}}{\mathrm{Re}\{\widetilde{R}(\sigma)\}}\right\} \tag{15}$$

In the presence of a FCE, substantial additional contribution from the signal appears in the imaginary part of $\widetilde{R}(\sigma)$. This contribution manifest itself in a signal phase increasing linearly as function of the spectral frequency (see Figure 17).

This calculation includes an "un-wrapping" of the phase in case it exceeds the range [–π, +π] (caused by the numerical atan() function). Compensations of ±2π are added to the phase where discontinuities (absolute difference greater than π) are noticed between two consecutive points.

The second step is a linear regression of the phase $\varphi(\sigma)$ versus the wavenumber σ.

$$\varphi_0, \delta\varphi = \mathrm{LinearFit}\{\varphi(\sigma), \sigma\} \tag{16}$$

The output consists of two values per band and sweep direction.

$\delta\varphi$ the slope

φ_0 the ordinate at origin

The validity of this fit is estimated by a goodness of fit computation, evaluated by means of a squared standard deviation s^2 of the data points along the fitted straight line.

$$s^2 = \frac{1}{N-1}\sum_{p=0}^{N-1}\left(\varphi(\sigma_p) - (\delta\varphi \cdot \sigma_p + \varphi_0)\right)^2 \tag{17}$$

This validity check helps to identify invalid measurements. If the s^2 value is too large, a possible confirmation could be to check with other band or other pixels, i.e.

if $s^2 > s^{thres}$, flag slope error. (18)

From this slope, can be extracted the interferogram displacement of a number of h fringes, using the metrology laser wavelength value λ_L:

$$h = \frac{\delta\phi}{2\pi\ \lambda_L} \tag{19}$$

This number is expected to be an integer, if the metrology laser optical path closely matches the IR one (see Section 2.4.1). However, if differences exist in the optical path, a fractional FCE could be measured. In that case, the fractional parts should remain constant in a given band.

This method has a weak point however. A FCE detected in Earth measurements could be caused by a multiple mismatch between DS, ICT, and ES. A priori, it is not known if DS and ICT are aligned with respect to one another. The current approach assumes they are independent. However, this uncertainty can be resolved quite easily.

A differential fringe count error between DS and ICT can only happen if the error occurs after the DS measurement but before the ICT measurement. Any other situation will produce the same FCE for the two. In consequence, if there is a difference between the FCE of the DS and the FCE of the ICT, it is because there is a relative phase between them. Knowing that, the phase between the two can be maintained equal simply by shifting the DS by *the same value* as the ICT. In practice, this situation is handled in an even simpler way: *the phase of the ICT is used* for the DS.

3.3.4 FCE correction

Once the OPD shift h is known, the correction of a shifted *undecimated* interferogram is straightforward: you simply shift it back to its correct position. This is done by removing a number of points equal to the shift at on one end of the IGM, the one corresponding to the direction of the shift. These removed points are put at the other end of the IGM, using the implicit periodicity of the Fourier transform.

The correction of a shifted and *decimated* interferogram is more difficult. This is because the shift will not be necessary an integer multiple of the decimation factor. Therefore, the decimated IGM would have to be shifted by a *fractional* number of points. This requires some sort of interpolation. The present approach is to compute in spectral domain a direct multiplication with the inverse phase function, as shown by Equation (20). As the new fringe alignment will remain present after the detection, the correction scheme brings previous signals back to this new fringe count. This explains the positive sign in the following equation, which *introduces* an equivalent FCE into the unaffected signals.

$$\widetilde{S}(\sigma)' = \widetilde{S}(\sigma)\ e^{+2\pi\, i\, h_b\ \lambda_L\ \sigma} \tag{20}$$

In the array representation of decimated signal this gives:

$$\widetilde{S}[n] = \widetilde{S}[n] \exp\left(+ 2\pi\, i \frac{h_b}{N_b\ DF_b} \left(\frac{\sigma_{0b}}{\Delta\sigma_b} \right) \right) \tag{21}$$

The corrected signals are also properly flagged as having been shift-corrected. Refer to Section 7.5 for more details about implementation of the fringe count error detection.

FCE and moving average

All the DS and ICT are aligned to the fringe count phase of the current moving average. Therefore, when a fringe count error is detected on an ES, the *current average* of the DS and ICT need to be *shifted* to match the new fringe count.

3.4 ALIGNMENT OF DATA TO A COMMON SPECTRAL GRID.

The channel centers defined for the EDR algorithm do not necessarily match the channel centers of the CrIS sensor. The wavenumber sampling is fixed by the precise laser wavelength during measurement, which does not necessarily correspond exactly to the output spectral grid and which may drift over time. Possible laser and optical alignment drifts will produce a different spectral grid on each measurement. The calibration software has thus to remap the sensor data onto a common reference grid to match the channel centers needed for the EDR algorithms. The new common resampling grid is called the "user's grid".

The total number of decimated points sent down by the instrument is given in Table 8. This number corresponds to the number of points sampled by the metrology laser, including guard bands on each side of the requested band limits. This number corresponds to a product of small prime factors, like discussed in Appendix 9.1.3. Processing will be done with this number of points. This table also gives the number of output bins in the SDR product (common user's grid dimension).

Table 8: Resampling parameters for each band

Band	OPD samples	Decimation factor DF_b	Decimated points	Output bins	$2\,MPD_b$ [cm]	λ_b [nm]
LW	20736	24	864	713	1.6	771.60494
MW	10560	20	528	433	0.8	757.57576
SW	5200	26	200	159	0.4	769.23077

A standard sinc interpolation could be used to perform alignment of data to a common spectral grid; but a different and more powerful approach is instead taken, which is described in the following. According to the sampling procedure in the interferometer, the spectra are aligned on a $n/(2\,MPD_b^s)$ spectral grid. Of course, $2\,MPD_b^s$ is dependent of the metrology laser wavelength, λ_L, the decimation factor, DF_b, and the number of points of the band, N_b, i.e.,

$$2\,MPD_b^s = N_b\,DF_b\,\lambda_L\,. \tag{22}$$

Since the laser wavelength is likely to change during the mission, or not be at the exact specific value corresponding to the requested output grid, the spectral grid and the lineshape due to interferogram truncation are not constant. We thus have to find a way to resample spectra in order to deliver them on a fixed, end-user defined, spectral grid with exactly the same $\mathrm{Sinc}(2MPD_b)$ function on each bin within the band b.

The mismatch between λ_L and λ_b comes from the fact that the number of OPD samples is fixed to a special prime factors multiple. In the LW, the target MPD_b = 0.8 cm, $\Delta\sigma = 1/(2\,MPD_b)$ = 0.625 cm^{-1} in fact differs from $\lambda_b = 2MPD_b / N_b$ =771.60494. But this is of no importance, as the **F**-matrix operator corrects for this difference.

The following relation:

$$L'_{b,p,d}[k] = \sum_{k'=0}^{N-1} F[k,k']\,L_{b,p,d}[k'] \tag{23}$$

with

$$\mathbf{F}_{\lambda_L,b}[k,k'] = \frac{\lambda_b}{\lambda_L} \frac{\mathrm{Sinc}\left(k'\frac{\lambda_b}{\lambda_L} - k\right)}{\mathrm{Sinc}\left(\frac{1}{N_b}\left(k'\frac{\lambda_b}{\lambda_L} - k\right)\right)} \qquad (24)$$

and where λ_L is the diameter of the sampling partition and λ_b is given in Table 8, transforms the spectrum aligned on a $n/(2\,MPD_b^s)$ spectral grid with a $\mathrm{Sinc}(2\,MPD_b^s)$ function on each bin to a spectrum aligned on a $n/(2\,MPD_b)$ spectral grid with a $\mathrm{Sinc}(2\,MPD_b)$ function on each bin. At the limit of $\lambda_L \to \lambda_b$, the correction matrix tends towards the identity matrix, as it should.

The **F**-matrix is a matrix enabling the calculation of the corrected spectrum with a simple product between a correction matrix and the spectrum vector. The application of the **F**-matrix will transform the spectral grid of the input signal $\sigma_{0_b}^X$, $\Delta\sigma_b^X$ into the requested user's grid defined by $\sigma_{0_b}^{req}$ $\Delta\sigma_b^{req}$, while keeping the same number of signal points. The resulting inherent sinc width will be that of the requested band, for example 0.625 cm^{-1} for the LW, corresponding to the interpolated MPD width of exactly 0.8 cm in the interferogram domain, as displayed in Figure 18.

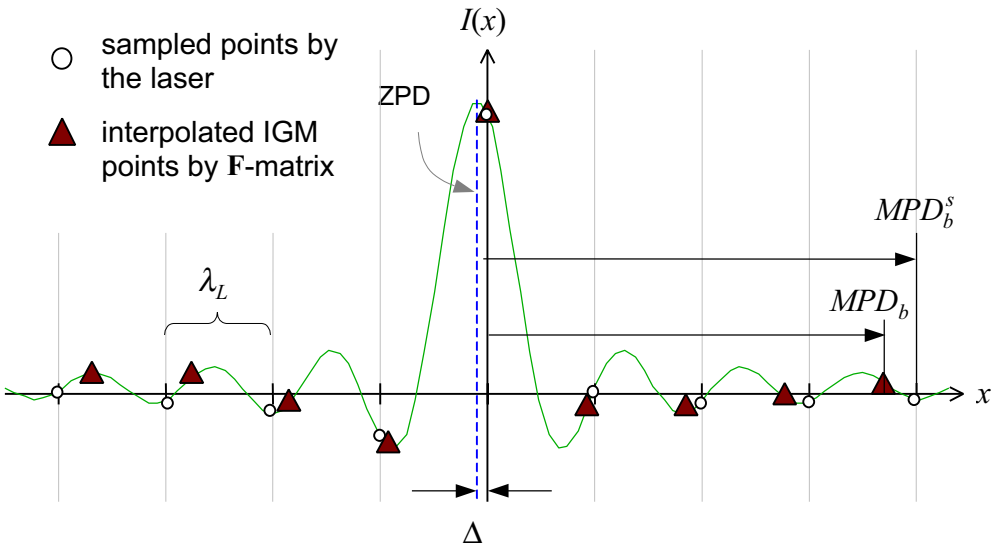

Figure 18: Effect of the **F**-matrix viewed in the interferogram domain

Wavenumbers assignation to each spectral bin is based on the laser metrology wavelength (see Section 4.1). the laser λ_L value is computed by the spectral calibration module (based on the calibration neon count). We make the hypothesis that the laser wavelength is stabilized on instrument (λ_L stable within 2 ppm). If the laser has drifted more than a given value, a recomputation of the **F** matrix is required.

This operator permits the correction to any input spectra sampled at a given wavelength onto the requested output grid with a specific fixed sinc width in each band. This is also required for the

application of the following self-apodization removal operation. This operator affects the spectral resolution, but introduces no stretching of the spectral axis.

3.5 ILS CORRECTION

When the radiation source in a Michelson interferometer is located in front of or behind the focal plane of the collimator, distortion arises in the spectral line shape. For CrIS, this well-known self-apodization induced by the instrument (ILS is distorted from a pure sinc) shall be removed from the scene radiance in each channel before being handed off to the EDR algorithms. The present section discusses an algorithm for correcting the distorted interferogram or spectrum.

The need for ILS correction is primarily driven by EDR cloud clearing algorithms, which require radiances measured in adjacent FOVs to be spectrally aligned onto the same channel center to possess the exact same ILS (here a pure sinc). Previous experiments, which used a single scanning FOV, did not experience these types of distortions since the same sensor FOV is used for every measurement.

The assumption is made that the self-apodization will remain constant over the instrument lifetime. This ILS stability assumption is based on the presence of dynamical alignment (DA) in the instrument system design. No algorithmic provision is made with respect to scene self-apodization, i.e. ILS variation with scene content (e.g. with clouds in it).

3.5.1 Introduction

In Fourier transform spectroscopy, the radiation to be examined is made to interfere in a Michelson interferometer and the interference signal is registered. The spectrum is then computed as the Fourier transform of the signal. Strictly speaking, this is true only under the assumption of a perfect instrument measuring the radiance of a very distant source. When this is not the case, the different instrument function contributors affecting the spectral lines of a data-cube spectrum which are due to effects inherent to the instrument are shown in Figure 19.

Starting from an elementary line contribution, e.g., emission from a single gas molecule, interactions between the molecules, expressed as temperature and pressure, produce a line broadening (C0 in Figure 19). This physical effect cannot be removed and reflects in fact some of the gas properties which we want to measure.

The first instrument contribution illustrated here (C1) is due to self-apodization. As the emitted energy enters the interferometer, different angles for the different fields of view produce different apparent spectral frequencies. A monochromatic signal thus produces a continuum of frequencies. The shape of this continuum is a function of the pixel geometry, the pixel position with respect to the optical axis, and the spectral frequency of the signal. The corresponding lineshape is indicated by Beam Divergence in Figure 19.

The second effect (C2) is due to perturbations like shear and tilt on the interfering beam which may fluctuate causing distortions on the measured lines. The corresponding lineshape is indicated by Modulation Degradation in Figure 19.

The third contribution (C3) is due to acquisition of interferograms which are of finite length. This third effect introduces the Sinc “dressing”. The corresponding lineshape is indicated by Sampling Window in Figure 19.

The mathematical operation for applying the contributions C2 and C3 to the gas line is expressed either by multiplication when considering the interferogram domain or by convolution when considering the spectral domain. However, the first contribution C1, i.e. self-apodization, can not be treated as a simple convolution in either domain since this effect is non-local in both domains.

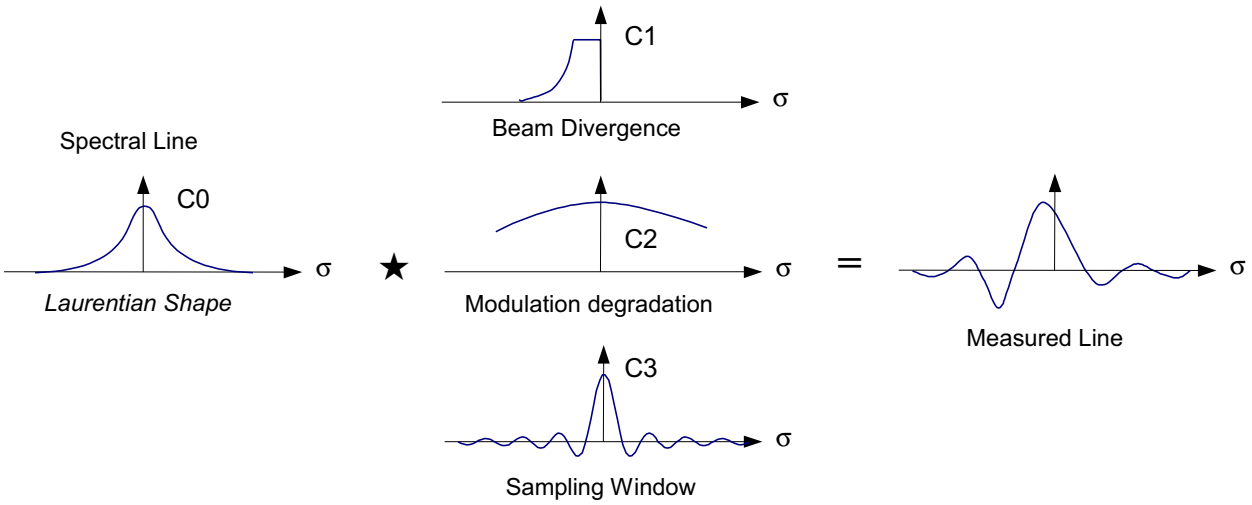

Figure 19: Instrument function contributors

To understand this self-apodization effect, consider that every monochromatic component of light traveling in the effective direction produces an interference signal that oscillates with the frequency corresponding to the correct wavenumber [RD 9]. However, as you may see from Figure 20, if the wave vector of a monochromatic plane wave component with wavenumber σ_0 makes an angle α with respect to the effective direction, its interference signal has a cosine dependence which oscillates at a frequency corresponding to the wavenumber $\sigma_0 \cos(\alpha)$. Thus, we shall call the line passing through the center of the collimator lens parallel to the effective direction the *effective* axis, as shown in Figure 20.

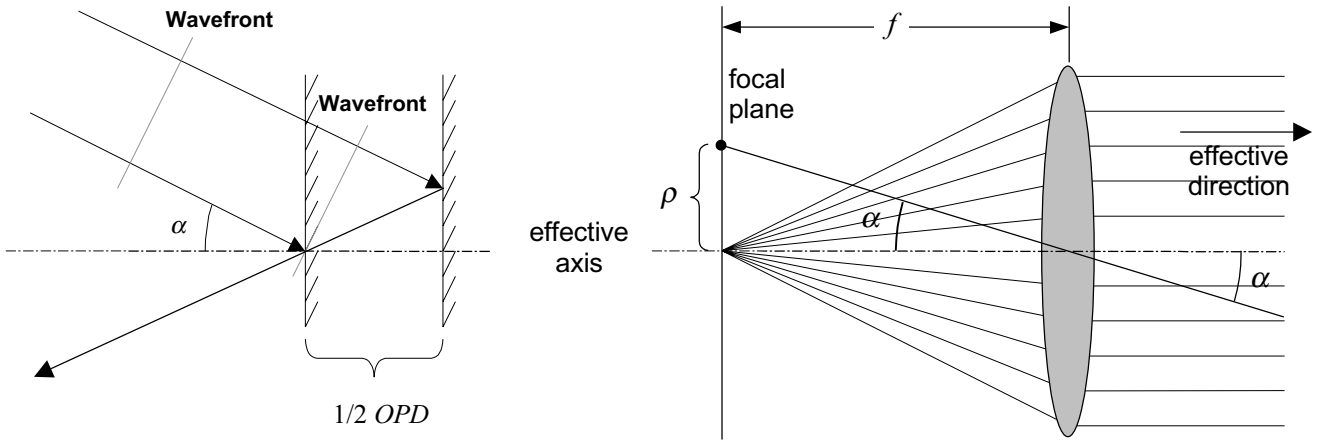

Figure 20: Off-axis geometry and rays

This figure identifies the point or the radiation source lying at the intersection of the focal plane and the effective axis. Any point in the focal plane aside from the effective axis gives a distorted spectrum, in which every wavenumber is multiplied by $\cos(\alpha)$. Therefore the presence of nonparallel light rays in the interferometer stretches the spectral lines toward the lower wavenumbers. This phenomenon is always present, unless we have a perfect point radiation source exactly at the point of the focal plane of the collimator lens (mirror), corresponding to the effective direction and an infinitely wide

interferometer aperture, so that there are no diffraction effects. When the interferometer is perfectly aligned, the effective axis passes through the center of the radiation source. If the radiation source is located exactly in the focal plane, the distance of its arbitrary point from the effective axis completely determines the angle α (see Figure 20), and thus determines the amount of spectral shift of the light emanating from that point. Let us now examine a monochromatic ($\sigma = \sigma_0$) point radiation source that is placed on a circle of radius ρ and centered on the effective axis, as in Figure 20.

The radiation is detected at the wavenumber:

$$\begin{aligned}\sigma(\rho) &= \sigma_0 \cos(\alpha) \\ &= \frac{\sigma_0}{\sqrt{1+(\rho/f)^2}}\end{aligned} \tag{25}$$

which further gives, under the paraxial approximation,

$$\sigma(\rho) \cong \sigma_0\left(1-\frac{\rho^2}{2f^2}\right) \tag{26}$$

One then sees that the line shape given by a round monochromatic radiation source which has a true line shape $E(\sigma) = \delta(\sigma - \sigma_0)$, a radius of R_0, and a shift of s from the effective axis is expressed as:

$$E(\sigma, s) = \begin{cases} \dfrac{2\pi}{\sigma} & s < R_0, \rho(\sigma) \le R_0 - s \\ \dfrac{2}{\sigma}\arccos\left(\dfrac{\rho(\sigma)^2 + s^2 - R_0^2}{2\rho(\sigma)s}\right) & \rho(\sigma) \in \left(|R_0 - s|, R_0 + s\right) \\ 0 & \text{elsewhere} \end{cases} \tag{27}$$

Here $\rho(\sigma)$ is the radius of the circle in the focal plane, whose radiation is detected at wavenumber σ, or according to Equation (25),

$$\rho(\sigma) = f\sqrt{2(1-\sigma/\sigma_0)} \tag{28}$$

In the case of the shifts $s = 0$, we obtain the well-known result that a delta peak line is seen as a boxcar line shape with the width:

$$\begin{aligned}\Delta\sigma = \sigma(0) - \sigma(R_0) &= \sigma_0 - \sigma_0\cos(\alpha) \\ &\approx \sigma_0 \frac{R_0^2}{2f^2}\end{aligned} \tag{29}$$

Figure 21 shows rays of the same wavelength (e.g. σ_0) forming different angles with respect to the optical axis and experience different effective OPDs.

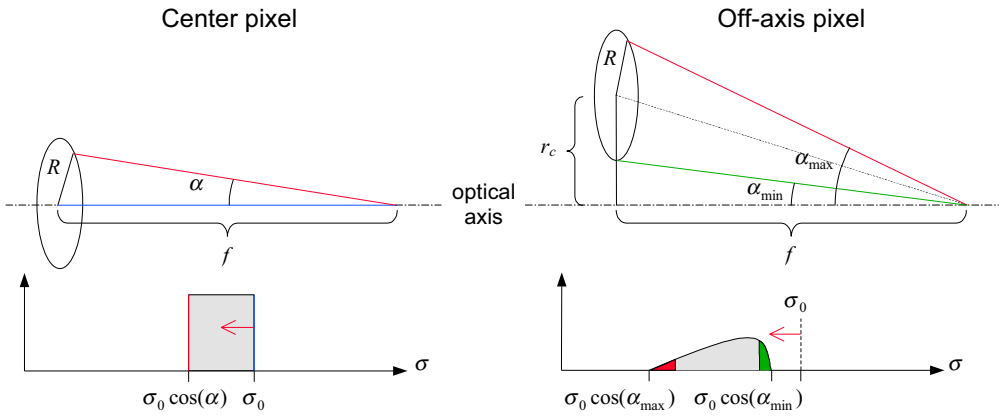

Figure 21: Self-apodization due to beam divergence in the interferometer

Self-Apodization: What it is...

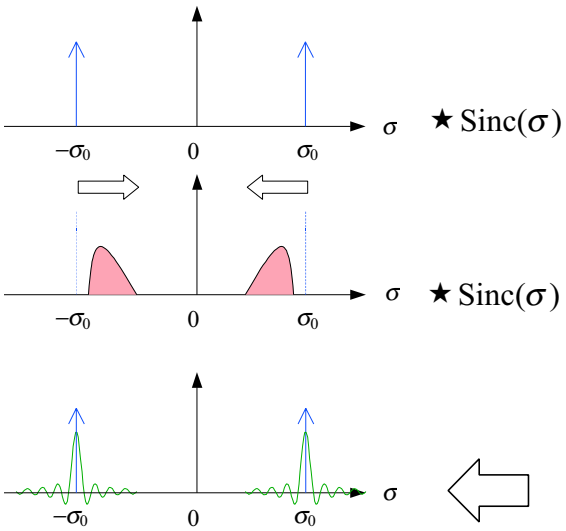

Beam divergence produces an effect corresponding to a *complex ILS*, dependent on *every* frequency contained in the incoming signal.

← Notice symmetric spectral stretching on both positive and negative frequencies

A good SA Removal algorithm should:

Remove the effects of frequency dependent line shape

Correct the stretching effect due to Self-Apodization

Provide output spectra with the same pure Sinc on each bin

Self-Apodization: What it isn't...

Not a simple convolution, nor a standard Sinc convolution by a frequency independent ILS

$$L(\sigma) = \int_{-MPD}^{+MPD} I(x)\, e^{-2i\pi x\sigma}\, dx$$

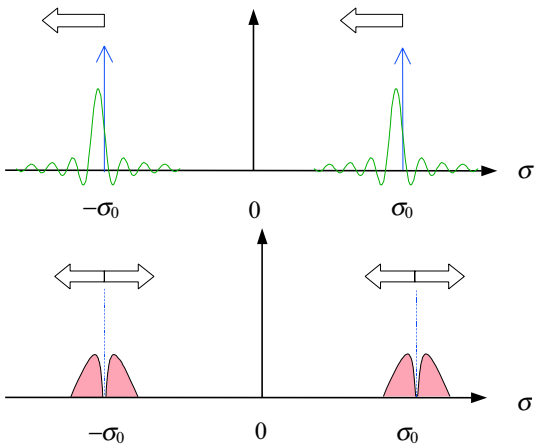

Not a simple modulation of the IGM

$$L(\sigma) = \mathrm{F}\{I(x)\cdot m(x)\}$$

Self-Apodization is more complex than that, since it is not a local operator neither only in the IGM domain, nor only in the spectral domain...

3.5.2 CrIS Off-Axis Self Apodization

As stated before, beam divergence introduced by finite field of view (extended source) produces broadening of monochromatic spectral lines. Both the detector size and its position on the focal plane define the width and the shape of the spectral lines. Due to their position, each of the CrIS FOV pixels has its own lineshape. Even though by symmetry there are only 3 basic different lineshapes, one at the center, four on the diagonal corners and four at the mid-point of the array sides, the 9 are all independent due to the fact that the instrument is not perfect and that the array will never be perfectly aligned.

Furthermore, the ILS is wavenumber dependent, because of:

- finite aperture of the interferometer,
- off-axis position of the detector in the focal plane with respect to the center of the interference pattern (9 pixels for CrIS),
- various optical, mechanical, and electrical imperfections of the interferometer system during the sweep of the optical path difference.

Figure 22 illustrates the self-apodization function normalized to the frequency of the incoming light. Note that the functions plotted in the figure also have to be normalized to unit area. The final ILS for each FOV and for each frequency could then be obtained by doing a convolution of these functions with the ideal Sinc function corresponding to the Fourier Transform of the interferometer sampling window. It can be seen that the self-apodization functions also contains the spectral stretch inherent to off-axis detectors. This spectral stretching causes each off-axis FOV to be slightly shifted in wavenumber from the on-axis FOV in the center of the array.

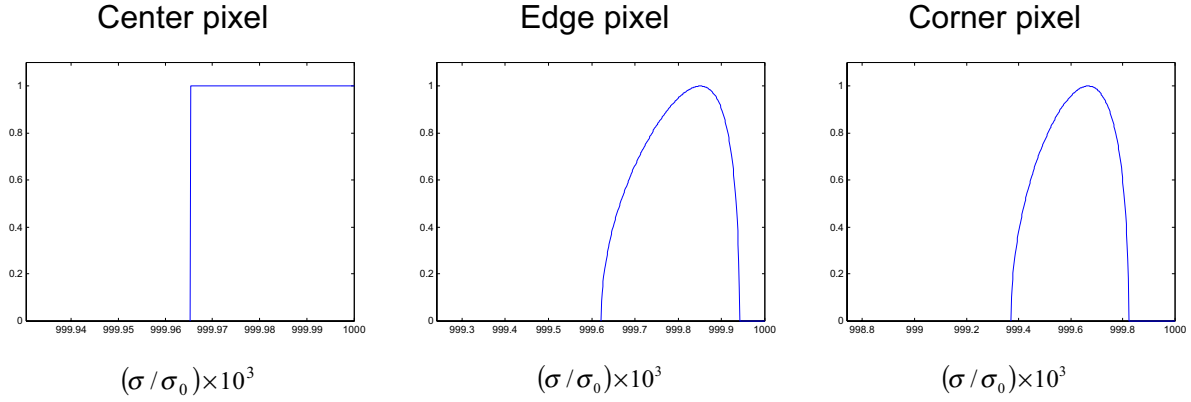

Figure 22: Self-apodization function for the three basic pixel geometry

Self-apodization within an interferometer depends upon the maximum OPD stroke, the FOV cone angle and the angular offset from the center FOV. For the results previously pictured the FOV footprint is 14 km yielding a FOV full cone angle of 0.96 degrees. The spacing between FOVs is 1.1 degree arranged in a 3×3 square pattern. The maximum OPD is 0.8, 0.4 and 0.2 cm for the LW, MW, and SW respectively. There is no telescope or other magnification in front of the interferometer to cause larger beam divergence which would worsen this self-apodization effect and make it harder to remove.

3.5.3 Self-Apodization removal

It is possible to correct and eliminate this artifact by deconvolving the instrument spectra with these functions (basically applying the inverse of the self-apodization effect). However, the difficulty arises because the apodization is different for each wavenumber across the spectral band of interest.

It is interesting to note that self-apodization removal can be combined with the spectral resampling (Section 3.4) and the apodization (Hamming or Blackman, as described in Sections 3.6.2 and 3.6.3) so that the three can be done simultaneously.

The self-apodization functions plotted in Figure 22 are computed assuming a perfectly aligned instrument. During the actual CrIS instrument build and acceptance testing there will be measurements of the ILS for each FOV to capture the effects of misalignment. These measurements can then be compared to calculations, which take into account misalignment data that will be obtained during optical coregistration tests. Each instrument is uniquely characterized in this regard so that this becomes part of the characterization database used by the SDR algorithm for that particular instrument.

Because of its position on the detector plane, each detector has its own beam divergence self-apodization. The deconvolution is applied in the spectral domain by performing a kind of frequency-dependent convolution of the analytical signal by the inverse of the original convolution matrix. This inverse matrix is tabulated for different pixel distance to the optical axis and spectral frequency. It can also include further physical instrument characteristics obtained at a future characterization stage. During deconvolution of a vector the pixel distance to optical axis remains the same for a given pixel but the frequency does change. So, for a given channel, say channel k', the effect of self-apodization on the original spectrum $L_{b,p}[k]$ is given by

$$L'_{b,p}[k'] = \sum_{k=0}^{N-1}\left[\int_0^{\sigma_s} d\sigma \int_0^{\sigma_s} d\sigma' \, 2MPD\,\mathrm{Sinc}\left(2MPD(\sigma_{k'}-\sigma')\right) ILS(\sigma',\sigma)\,\mathrm{Sinc}\left(2MPD(\sigma_k-\sigma)\right)\right] L_{b,p}[k] \quad (30)$$

or in matrix form,

$$L'_{b,p} = \mathbf{SA}\cdot L_{b,p} \quad (31)$$

with $$\mathbf{SA}[k',k] = \int_0^{\sigma_s} d\sigma \int_0^{\sigma_s} d\sigma' \, 2MPD\,\mathrm{Sinc}\left(2MPD(\sigma_{k'}-\sigma')\right) ILS(\sigma',\sigma)\,\mathrm{Sinc}\left(2MPD(\sigma_k-\sigma)\right) \quad (32)$$

In this last equation,

$$ILS(\sigma',\sigma) = \begin{cases} A & r_c < R_0, \quad \sigma\cos(\alpha_{\min}) \le \sigma' \le \sigma \\ \dfrac{A}{\pi}\arccos\left(\dfrac{\left(\dfrac{\sigma^2}{\sigma'^2}-1\right)f^2 + r_c^{\,2} - R_0^2}{2r_c f\sqrt{\left(\dfrac{\sigma^2}{\sigma'^2}-1\right)}}\right) & \sigma\cos(\alpha_{\min}) < \sigma' \le \sigma\cos(\alpha_{\max}) \\ 0 & \text{elsewhere} \end{cases} \quad (33)$$

with $$\cos(\alpha_{\min}) = \frac{f}{\sqrt{f^2 + (r_c - R_0)^2}} \tag{34}$$

and $$\cos(\alpha_{\max}) = \frac{f}{\sqrt{f^2 + (r_c + R_0)^2}} \tag{35}$$

(36)

and where A is a normalization factor used to preserve energy such that

$$\int ILS(\sigma', \sigma)\, d\sigma' = 1. \tag{37}$$

Figure 23 summarizes rays and angles geometric definitions.

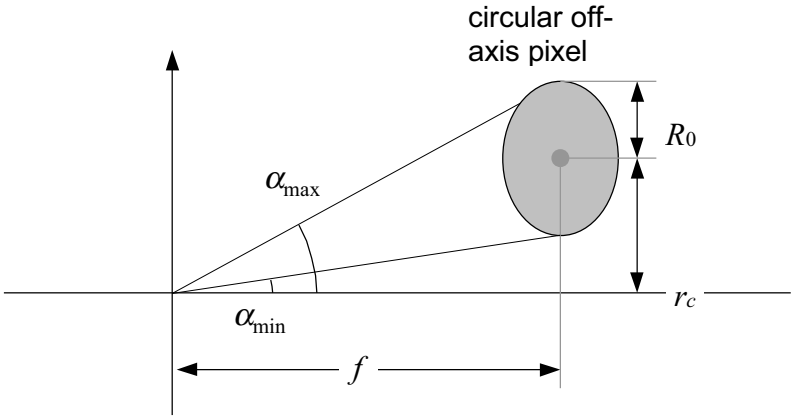

Figure 23: Off-axis geometry

Numerical evaluation of the integral

Equation (32) needs to be evaluated numerically for each matrix element (k, k'). Though not complex, this numerical procedure remains tedious even when using Gauss-Legendre integration technique (see Section 9.4). However, an approximation can be made that greatly simplifies the computation of the matrix elements while keeping excellent accuracy. This approximation consists in replacing the Sinc function in the integration over σ by a Dirac's delta, i.e.

$$2MPD\ \mathrm{Sinc}\big(2MPD(\sigma_k - \sigma)\big) \approx \delta(\sigma_k - \sigma) \tag{38}$$

which leads to the simplified form:

$$\mathbf{SA}[k', k] \approx \int_0^{\sigma_s} d\sigma' \mathrm{Sinc}\big(2MPD(\sigma_{k'} - \sigma')\big)\, ILS(\sigma', \sigma_k). \tag{39}$$

Equation (38) becomes exact as $2MPD$ tends toward infinity, i.e, when spectral resolution becomes infinite. One may analyze the limitations of this approximation within two conceptually related points of view.

First, if the signal in the interferogram is significantly high for OPDs larger than MPD then, in the incoming signal, high frequency structures are present that won't be correctly taken into account. The self-apodization effects are thus averaged over the spectral resolution size.

The second point of view considers that the self-apodization function, $ILS(\sigma',\sigma)$, does not strongly depends on the parametric frequency σ. Self-apodization is thus seen as a piecewise convolution over spectral section with size comparable to the spectral resolution.

But as seen in the following table, the error induced in the central point by the approximation of Equation (38) remains below 0.0035% for CrIS band definitions and pixels geometry.

Table 9: Error evaluation due to Dirac's delta approximation

Band	Error on Pixel in %		
	Center	Edge	Corner
LW	0.000390	–0.000012	–0.000007
MW	0.001360	–0.000270	–0.000012
SW	0.003441	–0.000600	–0.000600

Self-Apodization Removal

Since the effect of self-apodization may be included as the multiplication of the original spectrum by the self-apodization (SA) matrix, it can be as easily removed with a multiplication by the inverse of the SA matrix. The matrix

$$\mathbf{ISA} = \mathbf{SA}^{-1} \tag{40}$$

is thus the instrument lineshape correction (not a simple deconvolution) matrix that takes as input the pixel geometry and which is pre-computed for each CrIS following ground characterization tests.

This matrix is compatible in size with the incoming spectrum $L_{b,p,d}$ that has been resampled by the previous $\mathbf{F}$-matrix operator (see Section 3.4) at the exact wavenumber values corresponding to σ_k and $\sigma_{k'}$ of the $\mathbf{SA}$ matrix.

Results

Equation (39) provides on way of adding the self-apodization effects to an initial, sampled, spectrum. But to validate this procedure, a brute force technique should be used to include self-apodization in the sampled interferogram of high resolution spectra. This is achieved by summing the IGM contributions of every frequency contained in the high resolution spectrum, i.e.

$$\begin{aligned} I\left(x_n^b\right) &= \int d\sigma \left(\int d\sigma' \, ILS(\sigma',\sigma)\, e^{2i\pi\sigma' x_n^b} \right) S(\sigma) \\ &\approx \sum_{\kappa} \left(\int d\sigma' \, ILS(\sigma',\sigma_\kappa)\, e^{2i\pi\sigma' x_n^b} \right) S(\sigma_\kappa)\Delta\sigma \end{aligned} \tag{41}$$

where $S(\sigma_k)$ is a typical Earth scene spectrum, e.g. here from TIGR database, with a resolution of 0.1 wavenumbers. The IGM sampling rate was chosen according to specifications of Table 3. Upper panel of Figure 24 shows the initial TIGR spectrum (dashed line) that has been filtered to isolate CrIS LW band, along with the FFT of the self-apodized IGM (dotted line) for the corner pixel geometry.

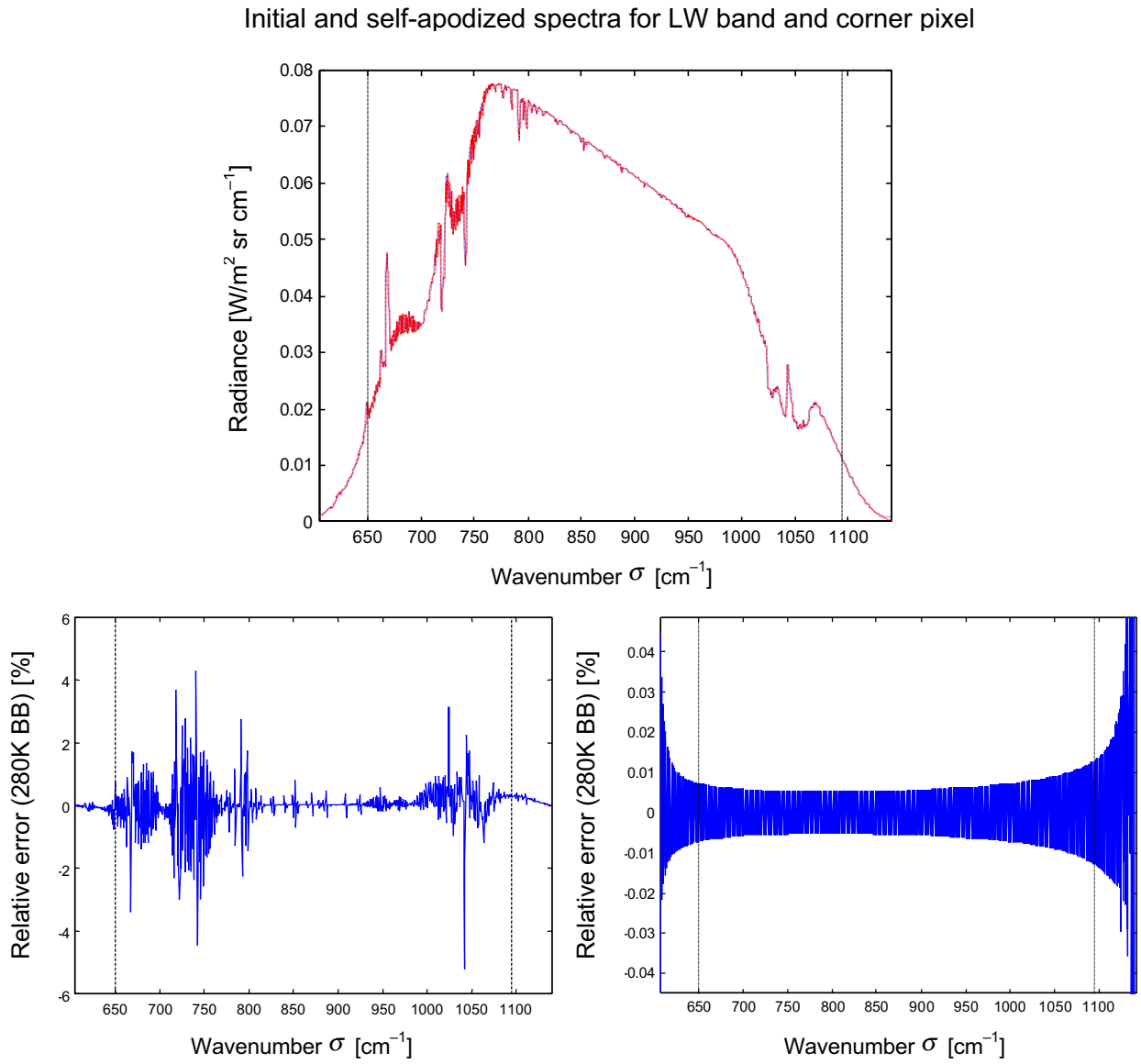

Figure 24: Self-apodization effects and correction

The radiometric errors (normalized relative to a 280K black body) that would be made if self-apodization was not corrected by SDR Algorithms is of the order of 1%, as presented in the lower left panel of Figure 24.

The corrected spectrum obtained by multiplying the self-apodized, sampled, spectrum by the inverse of the SA matrix of Equation (39) differs from the initial TIGR spectrum sampled at the same wavenumber values by only 0.01% (always normalized to a 280K black body) as can be seen in the lower right panel of Figure 24. This residual error shows that no spectral signature remains after the correction. Thus, the self-apodization removal procedure efficiently corrects the affected spectra provided that a good characterization of the instrument function, $ILS(\sigma',\sigma)$, is performed.

The impact of remaining errors due to non-precise characterization is evaluated by modifying the pixel geometry in the computation of the ISA matrix while keeping the right geometry for the construction of the self-apodized spectrum. The remaining relative errors are presented in Figure 25

for the cases where the corner pixel has been shift (left panel) or shrunk (right panel), with radiometric relative errors of 0.1% approximately.

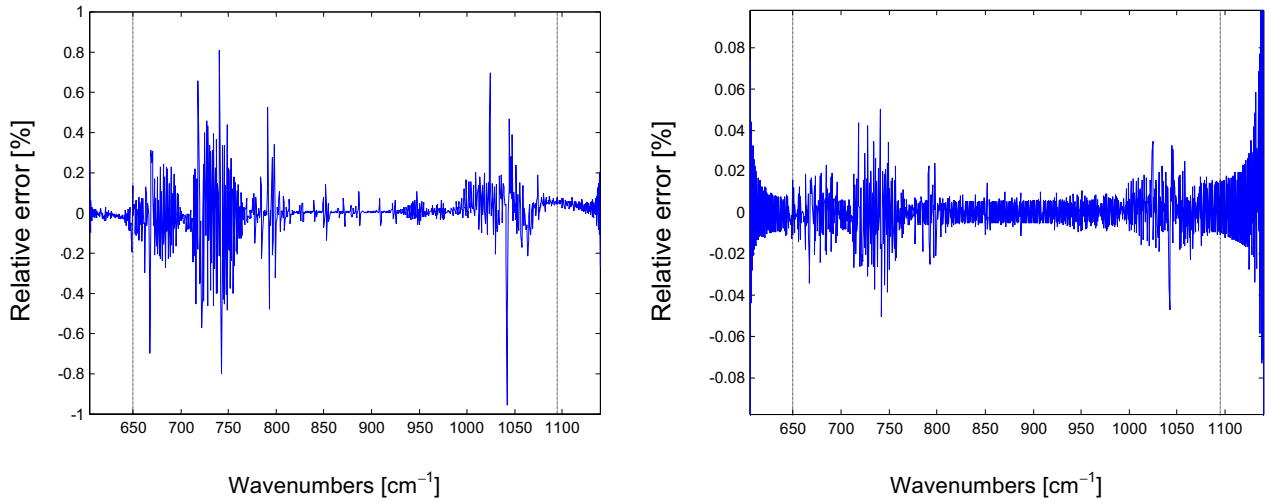

Figure 25: Errors due to non-precise characterization

Finally, as for the noise amplification effects, they have been extensively studied and no signal deterioration is expected following self-apodization removal.

Summary

The self-apodization effect (or FOV effect) introduced by beam divergence within the interferometer is corrected via a matrix multiply operation within the SDR algorithm. The matrix is derived from knowledge of the FOV size, shape, geometry and off-axis angles for each FOV obtained from instrument design and/or when characterizing the instrument on the ground. The operation corrects the spectral distortion resulting from this geometrical relationship and transforms the ILS into an ideal sinc response for all FOV's without significant error. The accuracy of this process is summarized in Table 10. Initial errors varying between 0.02% and 2% are reduced by a factor of more than 25 using this method and resulted in a residual error of less than 0.05%. This yields negligible radiometric bias errors of less than 0.1%.

Table 10: Summary of standard deviation error [%]

SA Not Corrected *SA Corrected*	Central Pixel	Edge Pixel	Corner Pixel
LW Band	3.7×10^{-2}	4.2×10^{-1}	7.7×10^{-1}
	2.6×10^{-4}	4.0×10^{-3}	6.8×10^{-3}
MW Band	1.0×10^{-1}	1.15	2.15
	2.6×10^{-3}	4.3×10^{-2}	8.5×10^{-2}
SW Band	2.1×10^{-2}	2.4×10^{-1}	4.6×10^{-1}
	9.0×10^{-5}	7.6×10^{-4}	9.0×10^{-4}

3.5.4 Residual term

Since other effects than the FOV effect (SA effect) may be not negligible for the CrIS instruments, the correction of the field of view effect discussed in the previous section may be not sufficient. For example, the modulation efficiency may vary with the optical path difference. Phenomenon like residual diffraction or mechanical imperfection may be responsible for this effect. In order to consider those effects, a modulation term over the interferogram is introduced. This modulation is modeled using a fourth order polynomial,

$$R(x) = c_0 + c_1 x + c_2 x^2 + c_3 x^3 + c_4 x^4 . \tag{42}$$

In that case, the effect is not wave number dependent and the spectrum is corrupted by a simple convolution,

$$\tilde{S}'(\sigma) = \tilde{S}(\sigma) \bigstar \mathrm{F}\{R(x)\}, \tag{43}$$

where $\mathrm{F}\{\ \}$ is the Fourier transform operator. It is possible that a more suitable form then equation (42) exists. This will be further determined following ground characterization of the CrIS instrument.

Since the application of the residual term is done via a convolution, we can easily express it in matrix form in order to include it into the CMO operator. In matrix form, the residual term can be expressed as,

$$\tilde{R}[k',k] = \frac{1}{N} \sum_{l=0}^{N-1} R[l]\, \mathrm{e}^{2\pi i l (k'+k)/N} . \tag{44}$$

3.5.5 Guard band damping

The results for the ILS correction shown previously were done using spectra damped in the guard band. The digital filter within the CrIS instrument performs two functions. It limits the band in order to decimate the signal, and it damps the signal in the guard band in order to prevent aliasing. But the digital filter is removed after the radiometric calibration, and the guard bands are no longer damped. Aliasing thus occurs since the self–apodization correction operator supposes a periodic signal. In order to correct the ILS properly, another filter is required to prevent the energy in the guard band to contaminate the precious information within the band. Also, it is important that this new filter be constant inside the band, since the correction operator is non-local. This non-locality will amplify the amplitude variation of the filter, and introduce an undesired bias into the spectra.

We have chosen to combine two Fermi steps for the simplicity and ease of use. The filter is defined by the following equation,

$$f_{\mathrm{F}}[k] = \left[\frac{1}{\mathrm{e}^{a_2 (k_0 - a_1 - k)} + 1} \right] \left[\frac{1}{\mathrm{e}^{a_4 (k - k_1 - a_3)} + 1} \right]. \tag{45}$$

Here it is the different values used for the three bands:

Table 11: Parameters for the post calibration filter f_F

	LW	**MW**	**SW**
k	[1-864]	[1-528]	[1-200]
k_0	77	49	22
k_1	789	481	180
a_1	55	22	6
a_2	0.5	1.0	2.0
a_3	55	22	6
a_4	0.5	1.0	2.0

To be independent of wave number, equation (45) is expressed in bins. It must be remarked that the bin number range begin at 1, and not at zero. In case the range starts at 0, the three k's in table 11 need to be reduced by 1.

3.6 SIGNAL APODIZATION

Both spectral characteristics and signal-to-noise are critical to retrieval accuracy of advanced IR sounders. For an unapodized (boxcar apodized) interferometer, the channel response function, given by the cosine transform of the apodization function, is a $sinc(\sigma)$ function, where σ is proportional to the frequency separation from the channel center. This function has large side-lobes that alternate in sign and fall off slowly with increasing frequency separation. Typically, interferograms are apodized (the interferogram is multiplied by a function which, in effect, smoothes the spectrum) to produce a channel response function that is localized and has small side-lobes.

When the Hamming apodization function is compare to other apodization functions found in the literature, it is found that it is a reasonable function to use for remote sensing purposes if the instrumental signal-to-noise is on the order of 1000. [RD 10] discusses the effects of apodization as they relate to sounding applications and shows that apodization should have no effect on retrieval results. In conclusion the Hamming FWHM is a reasonable value to use when describing the effective spectral resolution of the proposed IR interferometric sounders. At the opposite, when sidelobe suppression is more important than spectral resolution, the Blackman apodization is a much better choice.

3.6.1 Unapodized channel response function

The raw data product from an interferometer is a cosine transform of the incoming radiance (interferogram). The instrument has a finite maximum optical path difference, MPD. One obtains the radiance spectrum, convolved with a channel response function, by taking the cosine transform of the product of the interferogram, $I(x)$, with an apodization function, $A(x)$. The channel response function is the cosine transform of the apodization function. In the interferogram domain, the unapodized (or boxcar) apodization function is defined as:

$$A(x) = \begin{cases} 1 & \text{for } |x| \le MPD \\ 0 & \text{for } |x| > MPD \end{cases} \tag{46}$$

where x is the optical path difference. The channel response function for an unapodized interferometer is equal to

$$\frac{\sin(2\pi\, MPD\sigma)}{\pi\sigma} \equiv 2\,MPD\ \mathrm{sinc}(2\,MPD\sigma) \tag{47}$$

where σ is the wavenumber frequency. The unapodized channel radiance $S(\sigma)$ is given by a convolution of the channel response function with the monochromatic radiance at the entrance to the interferometer:

$$S(\sigma) = S_0(\sigma) \bigstar 2\,MPD\,\mathrm{sinc}(2\,MPD\sigma) \tag{48}$$

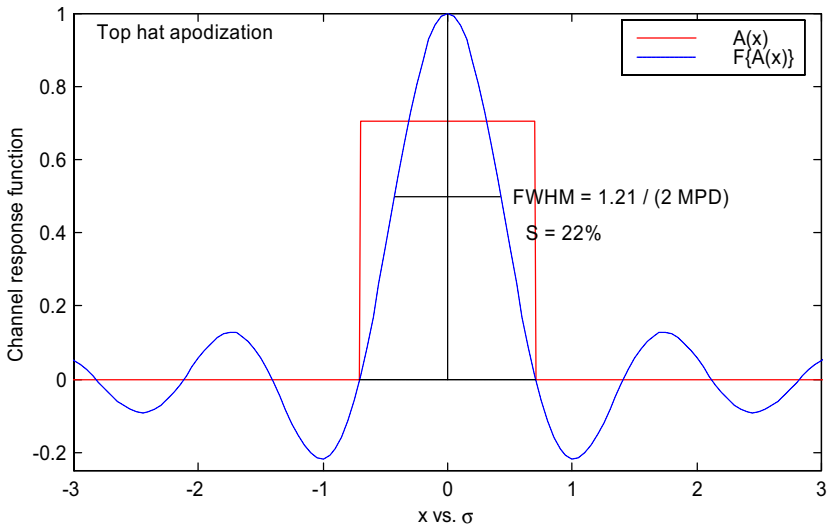

Figure 26: Boxcar apodization function and its sinc Fourier transform

The Nyquist sampling theorem states that if a spectrum is band-limited, i.e. $S(\sigma)=0$ for $|\sigma| \geq \sigma_{\max}$, then no additional information is gained by sampling the interferogram at a rate higher than $1/(2\sigma_{\max})$, although information is lost if the interferogram is sampled at a lower rate [RD 11]. The resulting unapodized spectrum is given as an array of radiance values, $S(\sigma)$ (or $S[n]$ where *n* is the channel index number).

The sinc function has large side-lobes which alternate between negative and positive values about the zeroes of the function spaced at $\sigma = \pm n/(2\,MPD)$. The first four side-lobes have heights of –21.7%, +12.8%, –9.1%, and +7.1% with respect to the central lobe (see Figure 26). The full-width-half-maximum (FWHM) of the sinc function is equal to:

$$FWHM = \frac{0.603355}{MPD} \approx \frac{1.21}{2\,MPD} \tag{49}$$

Equation (49) is used to describe the effective spectral resolution of an interferometer. Such a definition can be used to compare the resolution achievable from one interferometer to another, with different values of *MPD*. This definition is misleading, however, if one attempts to compare the spectral resolution of an interferometer to that of an instrument in which the channel response function does not have side-lobes. In typical bandpasses, only 45% of the unapodized spectral radiance comes from the central lobe. The remainder of the radiance comes primarily from the first few side-lobes, but non-negligible contributions arise from very distant frequencies within the bandpass, as the heights of the unapodized channel response function side-lobes are still above 1% at 30 zeroes from the central lobe.

In addition to not having a well defined resolution, the use of non-localized unapodized radiances produces complications in the retrieval of geophysical parameters. For multispectral retrievals (e.g., combining microwave and infrared radiances) it is convenient, but not necessary, to represent radiances in brightness temperature (i.e., the temperature of a blackbody with the same radiance). For unapodized spectra, brightness temperature is a meaningless concept due to the distortion, caused by the negative side-lobes which can produce negative channel radiances. The unapodized channel response function also produces complications in the development of efficient and accurate methods to compute channel radiances, such as the use of channel averaged transmittance functions.

3.6.2 Hamming's filter function

Many apodization functions can be applied to an interferogram which will localize the channel response function for the purpose of generation of rapid and accurate radiances. It is desirable to use an apodization function which satisfies retrieval models and also allows to return from apodized radiances into unapodized radiances, if this is required.

The apodization of an interferogram can be shown to be a linear transformation in spectral space between apodized and unapodized spectra [RD 10]. The Hamming apodization function is a reasonable and efficient function to use in atmospheric remote sensing applications with high signal-to-noise instruments, both because its channel response function has side-lobes less than 1% of the central lobe and because it has a well behaved analytic inverse transformation. The inverse transformation can be used to readily convert computed Hamming apodized spectra to spectra computed for other apodization functions (including unapodized) which may have poorer characteristics with regard to calculating channel transmittance parameters or radiances.

The Hamming cosine apodization function is given by:

$$A(x) = \begin{cases} (1-2a) + 2a\cos\left(\pi \dfrac{x}{MPD}\right) & \text{for } |x| \le MPD \\ 0 & \text{for } |x| > MPD \end{cases} \tag{50}$$

which has values of $A(x=0)=1$ and $A(x=MPD)=1-4a$.

The channel response function is given by the cosine transform of Equation (50) and is equal to:

$$H(\sigma) = 2MPD \cdot \mathrm{sinc}(2MPD\sigma)\left[(1-2a) + 2a\frac{(2MPD\sigma)^2}{1-(2MPD\sigma)^2}\right] \tag{51}$$

Apodized spectra can be shown to be equal to a 3-point running mean of unapodized spectra if the Nyquist channel spacing of $\Delta\sigma = 1/(2\,MPD)$ is used:

$$L[n] = (1-2a)\cdot L[n] + a\big(L[n-1] + L[n+1]\big) \qquad 0 < n < N-1 \tag{52}$$

Special case corresponds to both ends of the spectra, where we have:

$$\begin{aligned} L[0] &= (1-2a)\cdot L[0] + a\cdot L[1] \\ L[N-1] &= (1-2a)\cdot L[N-1] + a\cdot L[N-2] \end{aligned} \tag{53}$$

The matrix representation is similarly given by:

$$H[k,k'] = \begin{cases} a & \text{if } k = k'-1 \text{ or } k = k'+1 \\ 1-2a & \text{if } k = k' \\ 0 & \text{elsewhere} \end{cases} \tag{54}$$

The apodization operation is then simply performed by a simple matrix multiplication:

$$L'_{b,p} = \mathbf{H}\cdot L_{b,p} \tag{55}$$

The fact that the three last operators (spectral resampling, self-apodization removal, and Hamming apodization) are matrix operators permits their combination in a single operation to speed up computation:

$$\begin{aligned} L'_{b,p} &= (\mathbf{H} \cdot (\mathbf{S}\mathbf{A}^{-1}) \cdot \mathbf{F}) \cdot L_{b,p} \\ &= \mathbf{CMO} \cdot L_{b,p} \end{aligned} \tag{56}$$

where **CMO** stands for Correction Matrix Operator.

Hamming found an optimum value of a which minimizes the first side-lobe of the channel response function. He also showed that the optimum value of a was a function of the number of points in the spectrum; however, the optimum value of a converged to $a = 0.23$ for more than 100 points. With this value for a, the FWHM is equal to $1.8152/(2\ MPD)$, which is 50.4% larger than FWHM of the sinc.

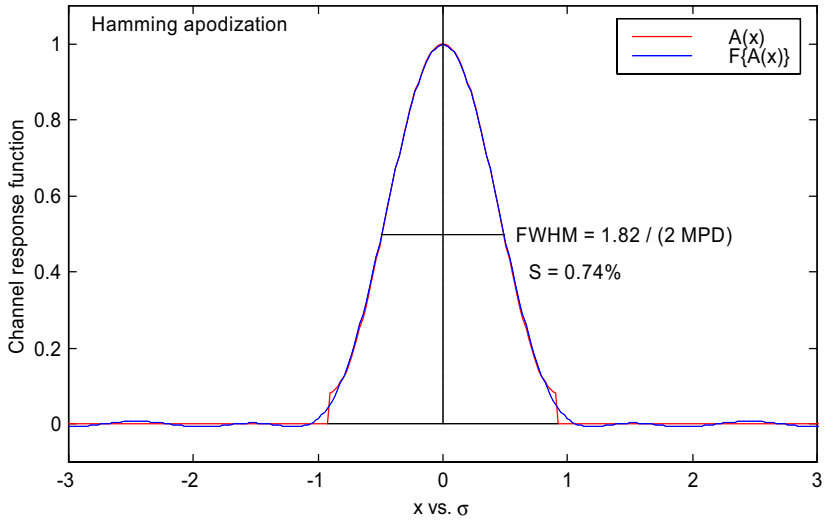

Figure 27: Hamming apodization function and its Fourier transform

The Hamming function has small side-lobes which heights for the first two equal to –0.74%, +0.27% with respect to the central lobe (see Figure 27).

One result of apodization is that the noise and signal become correlated between neighboring channels. For $a = 0.23$, the 3-point running filter reduces the noise in a given channel by a factor of 1.6; noise in adjacent channels is correlated by 62.5% and noise in channels separated by $\Delta\sigma = 1/(2\ MPD)$ is correlated by 13.3%.

In the case of the Hamming channel response function, the residuals are considerably less than the expected instrument noise levels for advanced sounders, which are on the order of 0.1°C.

The information content only depends on the value of MPD, not on the apodization function. The Gaussian apodization function has similar qualities to the Hamming function but has significant values extending to larger MPD. This implies that more information content exists in the Gaussian response function and that the small side-lobes of the Hamming channel response function actually degrade the resolution compared to the Gaussian function, so that the effective resolution of the interferometer is actually slightly poorer than $1.8/(2\ MPD)$.

The inverse transformation can be expressed as

$$L[n] = \frac{c_0}{(1-2a)}\left(L[n] + \sum_{i=1}^{N} r^i \cdot (L[n+i] + L[n-i]) \right) \quad (57)$$

With $c_0 = 1.909188309204$, and $r = -0.5590375815769$ for the Hamming case (a = 0.23).

Equations (57) and (52) express the set of unapodized radiances and cosine apodized radiances as linear combinations of each other. Hence, the information content of the complete set of radiances, including noise effects, is identical. This implies that retrieval using unapodized radiances, or cosine apodized radiances with $0 < a < 0.25$, should produce identical results provided all the channels are used. Furthermore, it implies that while the width of the central response function of an apodized function is larger than that of the unapodized function, there is no loss in "resolution" as both sets of functions contain equivalent information.

The Hamming function is a good function to use as a basis for calculating radiances and also reasonable to use in analysis of data because:

it gives a good tradeoff between spectral purity and apparent spectral resolution,

the channel noise correlation is localized,

and a simple analytic inverse exists.

In addition, radiance calculations need only to be done for the subset of channels being used in the retrieval process.

In cases where the SNR is about 1000, the Hamming side-lobes contribute less than the noise value to the radiance calculation and the Hamming radiances are indistinguishable from those radiances calculated from localized channel response functions. The inverse Hamming matrix utilizes all the Hamming channel radiances and, therefore, can be used to create radiances for apodization functions with smaller side-lobes.

3.6.3 Blackman's apodization function

The solution to the problem of leakage is to truncate the signal to be transformed less abruptly than with the rectangular cutoff. This is equivalent to finding a cutoff or apodization function with a Fourier transform which shows fewer side lobed than the sinc function. Numerous such functions exist, as the Hamming function presented in the previous section for example. An extensive overview of their individual properties can be found in the reviews by Harris [RD 12].

The width of the resulting function defines the best resolution achievable with a given apodization function. This is because if two spectral lines are to appear resolved from one another, they must be separated by at least the distance of their HWHM, otherwise no "dip" will occur between them. A sidelobe suppression always causes main lobe broadening, leakage reduction is only possible at the cost of resolution.

The choice of a particular apodization function depends therefore on what one is aiming at. If the optimum resolution of $1.21 / (2\ MPD)$ is mandatory, boxcar truncation (= no apodization) should be chosen (Section 3.6.1). The Hamming function has shown to have a resolution of $1.82 / (2\ MPD)$. Now if a resolution loss of 100% compared to the boxcar can be tolerated, the 3-term Blackman-Harris apodization is recommended. It produces one of the highest lobe suppression and can be

considered among the top performers in commonly used in FTIR apodization filters. The three- and four-terms Blackman-Harris apodization function is defined as follows:

$$A(p) = a_0 + a_1 \cos(\pi\, p) + a_2 \cos(2\pi\, p) + \left[\, a_3 \cos(3\pi\, p) \,\right] \tag{58}$$

This set of windows is a generation of the Happ-Genzel function. The coefficients given in Table 12 have been optimized numerically to trade main lobe width for sidelobe suppression. The Blackman function has very small side-lobes with heights smaller than 0.03% with respect to the central lobe, as shown in Figure 28 presenting the apodization function and its Fourier transform.

Table 12: Blackman-Harris coefficients

	a_0	a_1	a_2	a_3
3-term BH	0.42323	0.49755	0.07922	0.0
4-term BH	0.35875	0.48829	0.14128	0.01168

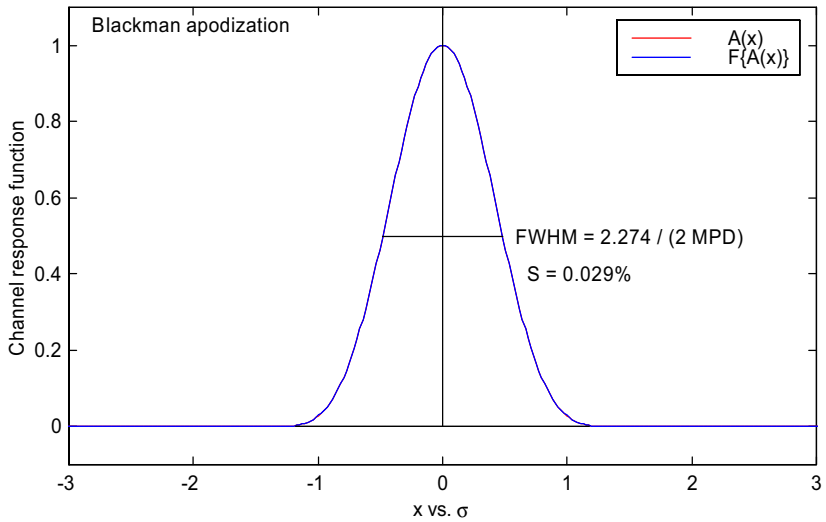

Figure 28: Blackman-Harris 3-terms apodization function and its Fourier transform

Summary

The Hamming apodization function is a reasonable function to use for analysis of interferometric data in remote sensing applications because it is suitable for rapid and accurate calculation of channel radiances. In addition, it produces a good trade-off between apparent spectral resolution and spectral purity. When comparing an interferometer to other instruments with localized channel response functions, the spectral resolution of the Hamming apodized interferogram, $FWHM = 1.8/(2\ MPD)$, is a reasonable value to use for the effective resolution of the instrument because radiances computed using only the central lobe of the Hamming channel response function agree to within the instrument noise to those using the entire Hamming response function. In addition, it offers the ability to transform from Hamming back to unapodized whereas other apodizations such as Blackman once applied do not allow the unapodized to be fully recoverable.

However, stronger apodizations such as Blackman allows for best retrieval code execution speed since it localizes the spectrum more, allowing the development of a faster forward model. Moreover, Blackman apodization has better sidelobe suppression to isolate modeling errors. It is intended to offer multiple apodization options (including unapodized) as a user selectable feature in the scientific code. The choice of apodization impacts both SDR and EDR algorithms.

4. SPECTRAL CALIBRATION

This section defines suitable algorithms for spectral calibration. Spectral calibration is the process of assigning absolute values to the wavenumber axis (x-axis spectral bins). This process shall be done for each CrIS channel with a specified accuracy of 5 ppm for all FOVs. This is a necessary step mainly because of possible variations in the metrology system, and other effects listed in Figure 29. The laser diode is prone to wavelength shifts due to junction temperature variations, injection current variations, and aging.

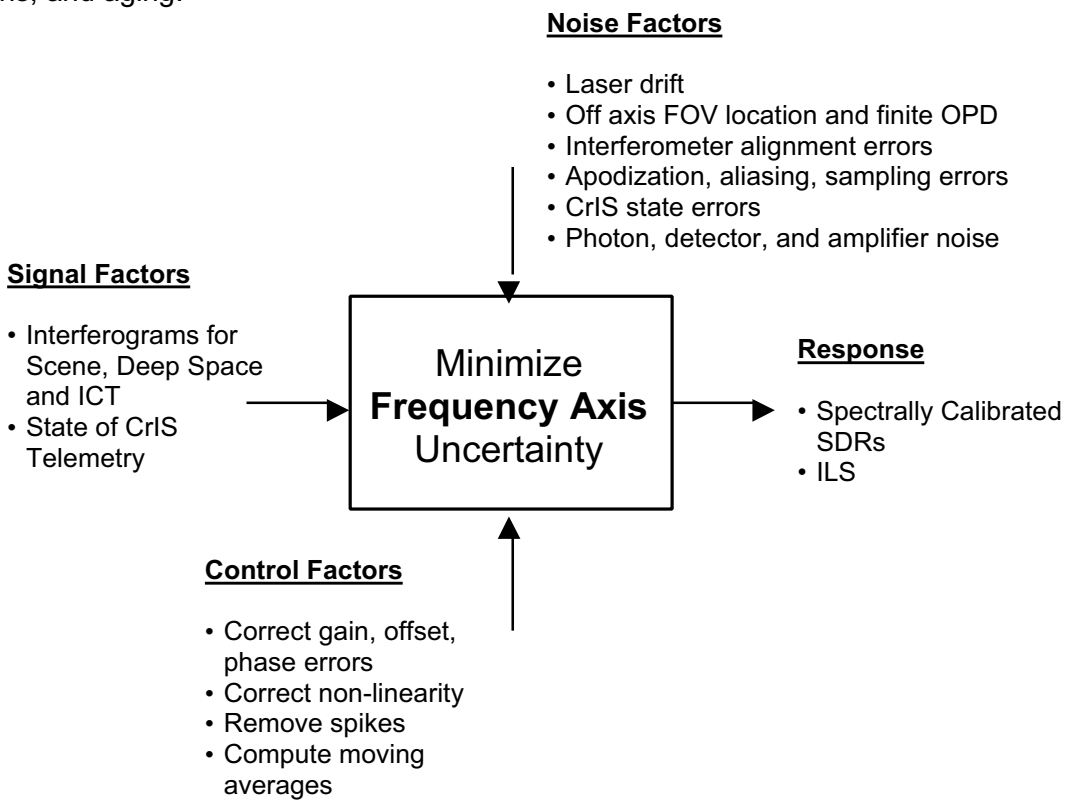

Figure 29: Spectral Calibration Parameter diagram

Before going any further, it is necessary to note that Spectral Calibration is related to the three following operations:

1– **Relabeling of the spectral axis**

The first operation is to assign correct wavenumbers to each measured bin throughout a spectral band, not taking into account other spectral effects like self-apodization. It is a simple relabeling of the spectral axis, using a neon measurement as a calibration reference. See sections 4.1, 7.3, and 9.2.

2– **Spectral resampling to common user's grid**

The second operation is to resample the spectral scale on a predefined common spectral axis definition and to fix the unapodized resolution (underlying sinc width). This is done via a spectral matrix multiplication, as described in Section 3.4

3– **ILS correction**

The third operation brings bins to their correct positions, based on the initial positions assigned by the previous modules. The ILS correction procedure is described in Section 3.

4.1 NEON-LAMP AS A SPECTRAL REFERENCE

The wavelength measurement system provides a laser wavelength measurement based on the comparison of the wavelength of the metrology laser and a filtered neon lamp [RD 13]. The filtered neon lamp is injected in the interferometer with the same optical path as the metrology laser. Metrology detectors convert the optical signal in an electrical signal. During a sweep measurement, counters are used to determine the number of fringes from both sources. The relative accuracy of the wavelength measurement depends on the interferogram length and the counting mechanism. Relative accuracy is improved by implementing interpolation at the beginning and at the end of a sweep measurement. Moreover, relative accuracy can also be improved by averaging measurements thus reducing the relative uncertainties.

This neon measurements can be used to adjust the laser operating parameters to keep the metrology wavelength of a FT-IR interferometer at a given value, or be sent as calibration data to calibrate the calculated power spectral density.

4.1.1 Wavelength Calculation

The theory of this particular wavelength determination is based on the comparison of the wavelength of the metrology laser and a neon lamp reference. During a spectral calibration sweep, counters are used to determine the number of fringes from both sources.

Number of fringes equal length ℓ of sweep divided by source wavelength:

$$N_L = \frac{\ell}{\lambda_L} \qquad N_{Ne} = \frac{\ell}{\lambda_{Ne}} \tag{59}$$

Ratio of fringes counts is equal to the inverse of the wavelength ratio:

$$\frac{N_{Ne}}{N_L} = \frac{\lambda_L}{\lambda_{Ne}} \tag{60}$$

Then, metrology wavelength:

$$\lambda_L = \frac{\lambda_{Ne} N_{Ne}}{N_L} \tag{61}$$

This basic method is improved by implementing an interpolation at the beginning and at the end of the neon count in order to estimate the neon fraction of the fringe period between the rising edges of the 2 fringe signals. Interpolation begins at the first laser fringe rising edge of the calibration sweep.

One counter is used to evaluate T and another counter for ?T. The ratio of the counters gives the fraction of the neon fringe period to be added at the beginning of the calibration sweep. The same process is applied at the first rising edge at the end of the calibration sweep. Then, the ratio calculated has to be subtracted from the neon lamp count.

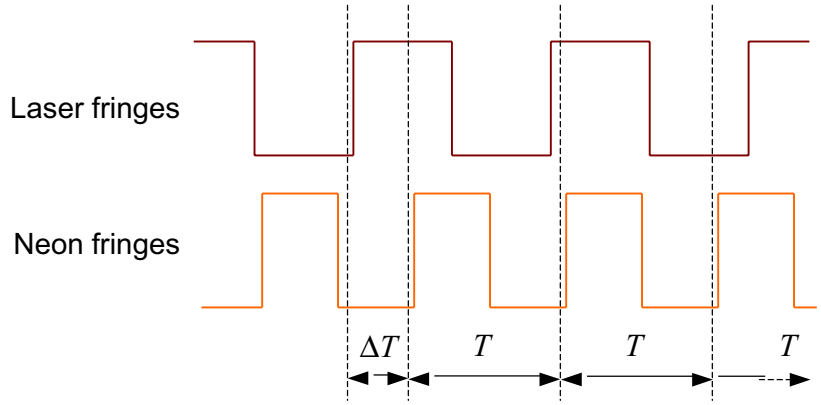

Figure 30: Neon calibration scheme using interpolation approach

The interpolated neon fringe count is then:

$$N_{Ne,Int} = N_{Neon} + \frac{\Delta T_{beginning}}{T_{beginning}} - \frac{\Delta T_{end}}{T_{end}} \tag{62}$$

The final calculated laser metrology wavelength is:

$$\lambda_L = \frac{\lambda_{Ne} N_{Ne,\,Int}}{N_L} \tag{63}$$

Operation neon baseline:

Spectral calibrations are expected to be conducted twice per orbit (at each pole),

2 seconds stabilization time: then compute correction for laser diode, then measure again for confirmation,

The characterization can be performed on both interferometer sweep directions and the results compared for verification.

Laser metrology wavelength obtained after calibration is precise within an accuracy of 0.5 ppm (for 128 sweeps at 2 cm^{-1}). The main source of error is the neon SNR. Other error contributors are the neon interpolation procedure, the laser zero crossing and the precision on the neon line position.

4.2 METROLOGY WAVELENGTH MONITORING

The SDR Science Code also monitors the laser diode wavelength between characterizations using neon lamp. The monitoring is performed with the help of a parametric model that depends on the laser diode temperature and bias current. The model is characterized on the ground prior to the launch. A correction is done for possible laser wavelength drifts and mismatch (see Section 3.4). A drift of more than 2 ppm since last CMO calculation (see Section 7.3 and Section 7.9) commands a new spectral resampling matrix generation and a new CMO calculation.

5. RADIOMETRIC CALIBRATION

Radiometric calibration is the process of assigning absolute values in physical units (usually radiance) to the intensity axis (ordinate y-axis) with a specified accuracy. For this purpose, deep space and internal calibration target (ICT - blackbody) are used as standard reference spectral radiance.

The calibration algorithm removes phase dispersion of the sensor over each IR band. Once removed, the complex spectral data is thus remapped into a cosine transform where the imaginary portion of the spectra can be discarded for a 1.41 noise factor improvement. Only the cosine transform data (real part of the calibrated spectrum) is delivered to the EDR algorithm. The sin transform data (imaginary part of the calibrated spectrum) can also be used to estimate noise.

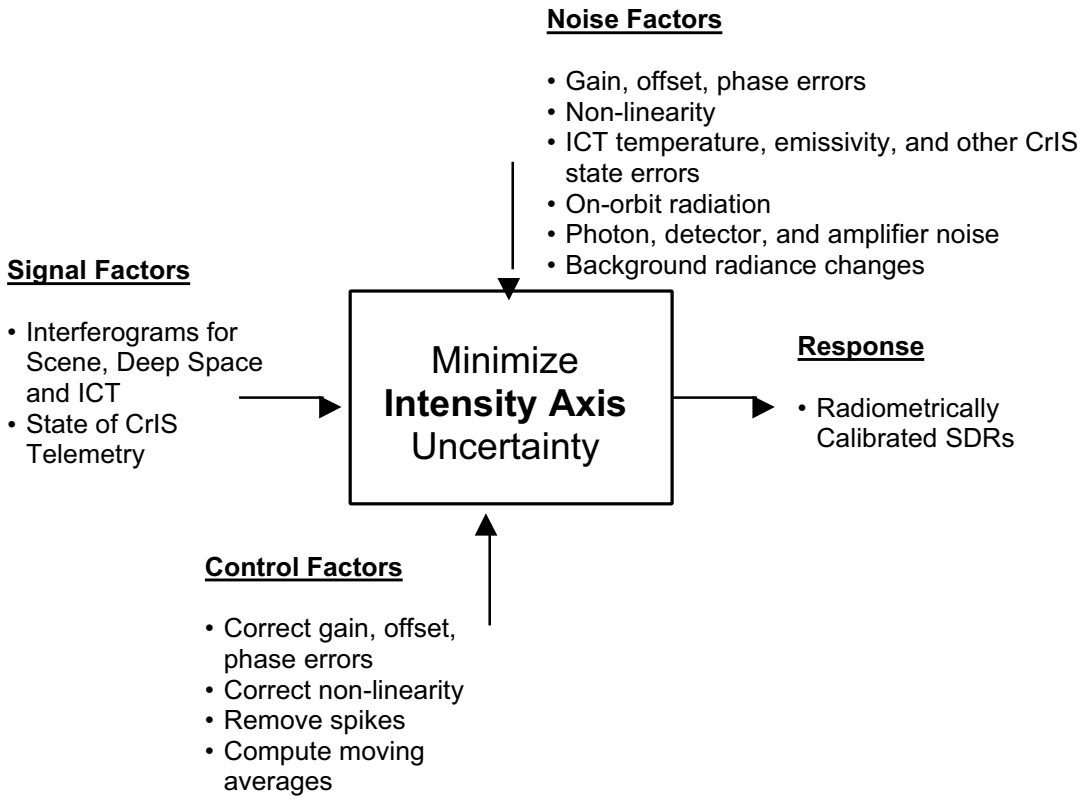

Figure 31: Radiometric Calibration Parameter Diagram

The generic term “radiometric calibration” refers to the following operations performed over each IR band:

Removal of offset and multiplication by the gain of a scene spectrum:

- Implement calibration Equation (70) with point-by-point complex multiplication.
- Use emissivity and temperature telemetry of the ICT to calculate the calibration BB radiance.
- Measure the calibration references at each scan
- Perform a moving average of the warm target data and cold target data.

Removal of sensor induced phase dispersion:

- Remove detector non-linearity (if present)
- Correct for fringe count errors
- Correct for off-axis self-apodization on each FOV
- Correct for polarization errors
- Remove orthogonal noise components (delivers real component)

5.1 BASIC RADIOMETRIC RELATIONS

The basic mathematical relation between interferograms and spectra is the Fourier transform. The general relationship between an interferogram and its equivalent spectrum can be expressed as:

$$\tilde{S}(\sigma) = \mathrm{F}\{I(x)\} \tag{64}$$

where the left side of the equation (spectral domain) denotes the spectrum as a function of wavenumber (σ), and the right side (spatial domain) denotes the Fourier transform of the interferogram as a function of the optical path (x). As the measured interferogram is not symmetrical (because of dispersions effects in the beamsplitter and electronics, among other contributors), the resulting spectrum will be complex (represented here by the over-tilde (~) notation). The thermal emission of the beamsplitter can cause contributions having repercussions in the imaginary part [RD 14] (complex filtering sends components in the real part). Thus the resulting observed phase becomes dependent on the incident photon flux, i.e. the phase of deep space, scene, and calibration blackbody spectra may vary substantially.

The computer implementation of the discrete Fourier transform uses the standard Fast Fourier Transform (FFT) algorithms. The transformation is represented as:

$$\tilde{S}[n] = FFT\{I[m]\} \tag{65}$$

When using numerical Fourier transforms, special care must be taken about special particularities of the numerical implementation (see Appendix 9.1 for more details). Also, when dealing with decimated interferograms, *alias unfolding* (also called Spectrum Unscrambling or Spectrum Re-ordering) must be performed in order to remove the down conversion to a zero IF (Intermediate Frequency) introduced at the satellite level (See Appendix 9.2 for more details).

5.2 GENERAL CALIBRATION EQUATION

The basic approach for determining absolute radiance measured by a FTIR spectrometer is the same as that used for filter radiometers and has been used successfully for other interferometric applications [RD 3]. The detectors and electronics are designed to yield in principle an output which is linear with respect to the incident radiance for all wavenumbers in the optical passband of the instrument, and two reference sources are viewed to determine the slope and offset which define the linear instrument response at each wavenumber.

The measurement obtained by the system is proportional to the spectral power distribution at the detector. The latter is composed of the emission coming from each input port, along with thermal emission of the spectrometer. Using the notation given in Section 1.6, the measurement can be expressed by the linear relation:

$$\tilde{S}^{es}(\sigma) = \tilde{G}(\sigma)\left((F_{\mathrm{ALL}} L)(\sigma) + \tilde{O}(\sigma) + \varepsilon \right) \tag{66}$$

where $\tilde{S}^{es}(\sigma)$ is the calculated complex spectrum from an *earth scene measurement* (arbitrary units, commonly referred to as digital units [d.u.]),

$L(\sigma)$ is the true incident spectral radiance from the *scene* (in [r.u.]),

$\tilde{G}(\sigma)$ is the overall spectral responsivity of the instrument, referred to as *gain*, it is a complex function to include interferogram phase dispersion/delays,

$\tilde{O}(\sigma)$ is the instrument emission, referred to as *offset,* it is the stray radiance, including all modulated radiance that does not come from the scene (in [r.u.]),

F_{ALL} is the instrument operator, which includes all effect that the instrument might introduces such as self-apodization, IGM modulation, etc. (see Section **Error! Reference source not found.**). The notation $(F_{\mathrm{ALL}} L)(\sigma)$ implies that the radiance $L(\sigma)$ has been affected by the instrument,

ε is the noise, with zero mean $\bar{\varepsilon} = 0$, and standard deviation equal to *NEdN*.

Equation (66) expresses the linear relationship between the true spectral radiance L and the measured, uncalibrated spectrum $\tilde{S}^{es}$. Two non-equivalent calibration observations are required in order to determine the two unknowns, that are the gain $\tilde{G}$ and the offset radiance $\tilde{O}$ as defined in Equation (66). The offset is the radiance, which, if introduced at the input of the instrument, would give the same contribution as the actual emission from various parts of the optical train.

Equation (66) can be solved to yield:

$$\tilde{G} = \frac{\tilde{S}^{H} - \tilde{S}^{C}}{F_{\mathrm{ALL}} L^{H} - F_{\mathrm{ALL}} L^{C}} \quad \text{[d.u./r.u.]} \tag{67}$$

and

$$\tilde{O} = \frac{\tilde{S}^{C} F_{\mathrm{ALL}} L^{H} - \tilde{S}^{H} F_{\mathrm{ALL}} L^{C}}{\tilde{S}^{H} - \tilde{S}^{C}} \quad \text{[r.u.]} \tag{68}$$

where L^C and L^H are the calculated radiances, modeled by the theoretical spectral radiance of the corresponding observed uncalibrated radiances $\tilde{S}^C$ and $\tilde{S}^H$. Those 2 references could be a hot and a cold blackbody modeled by the Planck function (Equation 3) multiplied by the emissivity of the blackbody.

By inverting Equation (66), one can derive the calibration equation used to convert a spectrum from an unknown scene into calibrated data:

$$L' = F_{\text{ALL}} L = \frac{\tilde{S}^S}{\tilde{G}} - \tilde{O} \tag{69}$$

For ideal spectra with no noise, this expression for the calibrated radiance would be purely real, since the phases of the ratioed difference spectra are the same. This cancellation of the phases avoids the square root of two (1.4142) noise amplification, which is obtained by taking the magnitude of spectra with nonzero phase. Because the phase of the ratio of difference spectra is zero to within the noise, the calibrated spectrum can equally well be defined in terms of the real part of the ratio (as shown) or in terms of the magnitude of the ratio [RD 3]. When non-linearity is present, a special correction must be applied on different interferograms coming from affected detectors.

5.3 CrIS SPECIFIC CALIBRATION EQUATION

For the CrIS instrument, because the cold reference measurement obtained by looking at the deep space (DS) corresponds to an emission at a very low temperature ($T^C \approx 4K$), one can safely make the approximation that the cold term has a negligible spectral radiance ($L^C(T^C) \approx 0$). The calibration equation can now be expressed in the simplified form

$$L = F_{\text{ALL}}^{-1}\left[\left(\frac{\tilde{S}^S - \tilde{S}^C}{\tilde{S}^H - \tilde{S}^C}\right) F_{\text{ALL}} L^H\right], \tag{70}$$

where F_{ALL}^{-1} is the inverse of the instrument operator F_{ALL} defined in the previous section. Here, the overall effect of the instrument (ILS) has been removed from the calibrated spectrum such that L is the desired calibrated and instrument corrected spectral radiance. For implementation in the SDR Algorithms, Equation (70) is the optimal choice and is the baseline for the present SDR Algorithms. There would be no real gain in computing the following equivalent:

$$\tilde{G}' = \frac{F_{\text{ALL}} L(T^H)}{\tilde{S}^H - \tilde{S}^C} \tag{71}$$

$$\tilde{O} = \tilde{G}' \tilde{S}^C \tag{72}$$

$$L = F_{\text{ALL}}^{-1}\left[\tilde{S}^S \tilde{G}' - \tilde{O}\right] \tag{73}$$

The previous computation of actual offset $\tilde{O}$ and inverse gain $\tilde{G}'$ saves a division at each calibration, but they would need to be computed at each update of the moving average and each time a FCE is detected. This fact and the extra complexity of new arrays handling make this option less attractive.

5.4 RADIOMETRIC MODEL

The radiometric model used to generate the theoretical radiance must be as accurate as possible in order to model in the most realistic way the ICT calibration source and make the calibration as close as possible to the reality. The radiometric model takes into account the emissivity and transmissions of the various elements seen by the instrument when looking at the ICT and their associated temperatures. Moreover, a radiometric uncertainty model of the instrument includes the temperature uncertainties of the ICT and the CrIS interferometer, their temperature variations with time and their emissivities.

The radiance seen by the instrument when looking at the ICT follows the relationship:

$$\begin{aligned} L^H(\sigma) &= \varepsilon^{ict}(\sigma)B(\sigma,T^{ict}) \\ &+ \sum_i (1-\varepsilon^{ict})\tau_{1..(i-1)}\varepsilon_i(\sigma)B(\sigma,T^i)\left(\sin^2\left(\theta^{i2}\right)-\sin^2\left(\theta^{i1}\right)\right) \\ &+ \sum_j (1-\varepsilon^{ict})\tau_{1..(i-1)}\varepsilon^{env}(\sigma)B(\sigma,T^j)\left(\sin^2(\theta^{j2})-\sin^2(\theta^{j1})\right) \end{aligned} \quad (74)$$

where

T^{ict} is the ICT temperature (K),

Error! Objects cannot be created from editing field codes. is the ICT blackbody effective emissivity (wavenumber dependent),

Error! Objects cannot be created from editing field codes. is the optical component i temperature (K),

Error! Objects cannot be created from editing field codes. is the optical component i emissivity (wavenumber dependent),

Error! Objects cannot be created from editing field codes. are the angular extension of the optical component i,

Error! Objects cannot be created from editing field codes. is the environment j temperature in (K),

Error! Objects cannot be created from editing field codes. is the environment j emissivity (wavenumber dependent),

Error! Objects cannot be created from editing field codes. are the angular extension of the environment component j,

Error! Objects cannot be created from editing field codes. accounts for absorption / transmission between components i and ICT,

$B(\sigma,T)$ is the Planck function (as defined in Equation 3),

The environments and components of the model are sketched in Figure 32. They are to be understood as blackbody contributors to the total radiance seen by the instrument when looking at the ICT. Here, each environment represents a collection of many components modeled by a blackbody at some average temperature. Note that all components and environments are defined by angular extension to properly account for the radiance that actually reaches the detectors.

In this model, the temperatures from the ICT, the beamsplitter and at two positions in the optical assembly are directly measured by PRT. The temperatures of the central obscuration, the dynamic alignment mirror and the porchwing mirror are estimated from nearby PRT measures. Since there is no temperature probe nearby the scene selection module and the scene selection module baffle, an estimate of their temperature should come directly from the instrument specifications (TBD).

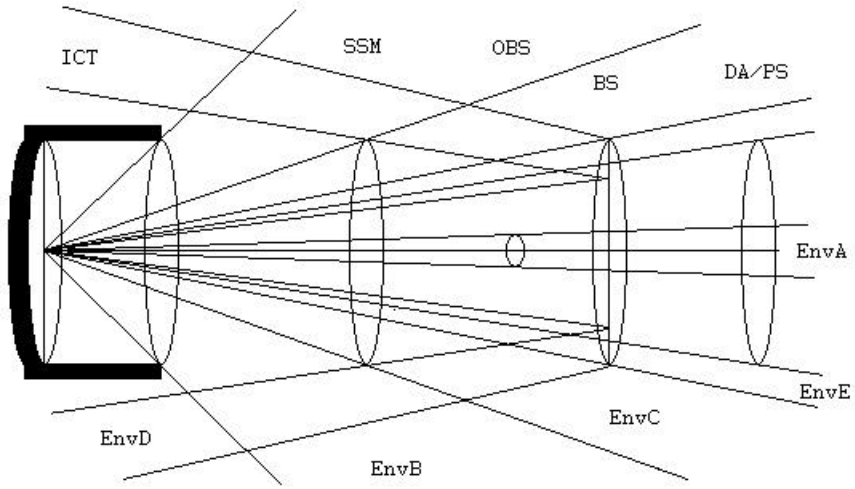

Figure 32: Radiometric model when the scene is the ICT

Table 13: Temperatures used in the ICT model

Temp	Error [K]	Description
T^{ict}	0.01	ICT (2 readings)
T^{BS}	0.01	Beamsplitter (2 readings)
$T^{oma1,2}$	0.01	Optical module assembly (2 positions)
T^{obs}	1	Obscuration
T^{DA}	1	Dynamic alignment mirror
T^{PS}	1	Porchwing mirror
T^{Env_BS}	1	Environment around beamsplitter
$T^{r\_Env\_BS}$	1	Reflected environment around beamsplitter
$T^{Env\_DA/PS}$	1	Environment around dynamic alignment and porchswing mirrors
T^{SSM}	5	Scene selection module
T^{baffle}	5	Scene selection module baffle

The emissivity and transmission values are pre-characterized on ground before launch. They are provided in RDRs within calibration data packets in the form of arrays with spectral interval defined over a pre-computed grid corresponding to the input raw vectors $\tilde{S}^X[n]$. The exact match of spectral scales is not critical as emissivities and transmissions are expected to be slow varying functions over their respective spectral ranges. No interpolation is necessary in the SDR algorithm processing.

5.4.1 Radiometric error

Some uncertainties are imbedded in the radiometric model. They are cause by the uncertainties on components temperature and emissivity. The largest source of error comes from the characterization of the emissivity of the ICT followed by the uncertainties on the temperature of the ICT. For the environment components, it is the baffle of the scene selection module and the sides of the beamsplitter, which are the principal sources of error. In those cases both temperature and emissivity are not well characterized. It should be noted that both ICT and components emissivity are expected to be known to better precision that what as been assumed here. In the following table, radiometric errors are given normalized relative to a blackbody at 287K. The value for the worst case (maximum error for all wavelength) is shown.

Table 14: Radiometric model uncertainties

Component name	T [K]	dT [K]	min angle [degree]	max angle [degree]	%flux ratio *B*(287 K)	%error by dT *B*(287 K)	%error by ε *B*(287 K)
ICT	310	0.01	0.00	29.08	**99.925**	**0.0982**	**0.18**
SSM	303	5	0.00	19.54	0.0029	0.0011	0.00029
Obstruction	311	1	0.00	2.05	0.0031	0.0002	0.0003
Beamsplitter	308	0.01	2.05	7.81	0.013	7.7e-006	0.0012
Dynamic alignment	308	1	2.05	6.26	0.00013	9.3e-006	1.3e-005
BS by DA reflect.	308	0.01	2.05	4.97	0.0023	1.4e-006	1.4e-006
Porchswing	308	1	2.05	6.26	0.00018	1.2e-005	1.8e-005
BS by PS reflect.	308	0.01	2.05	4.97	0.0036	2.2e-006	0.00035
Baffle of SSM	303	5	19.54	29.08	**0.06**	**0.02**	**0.0059**
Env. Side of BS	311	1	7.81	19.54	**0.23**	**0.014**	**0.022**
Reflection of Env. side of BS	311	1	7.75	7.81	0.00032	2.1e-005	3.1e-005
Env. Side of DA/PS	311	1	6.26	7.81	0.0094	0.00058	0.00092

5.4.2 Temperature Computation

Temperature readings are expected to be given directly in Kelvin from the CrIS instrument within RDRs calibration packets. If it is not the case, ACD counts representing the PRT readings will be downloaded as calibration data. Besides the actual measurement reading R^X in [d.u.], two additional readings of calibration resistors R^X_{ref1} and R^X_{ref2} will be transmitted in order to perform a precise calibration of the temperature measurement. The exact values of these standard resistors Ω^X_{ref1} and Ω^X_{ref2} are also known as calibration data.

The following calibration constants must first be computed:

$$k_1^X = \frac{\Omega^X_{ref1} - \Omega^X_{ref2}}{R^X_{ref1} - R^X_{ref2}} \tag{75}$$

and

$$k_2^X = \frac{R^X_{ref1}\,\Omega^X_{ref2} - R^X_{ref2}\,\Omega^X_{ref1}}{R^X_{ref1} - R^X_{ref2}} \tag{76}$$

Then the measured resistance in ohms can be extrapolated as:

$$\Omega^X = k_1^X R^X + k_2^X \tag{77}$$

And finally the temperature in Kelvin is obtained from a pre-characterized polynomial expansion:

$$T^X = \sum_{i=0}^{N^t} P_i^X (\Omega^X)^i \tag{78}$$

5.5 SIGNAL COADDITION

The common practice of coaddition of interferograms is valid for the reduction of true noise (short-term random fluctuations). However, it is not valid for dealing with instability and drift, as it produces a hange of interferometric modulation analogous to optical pseudo-coherence effects [**RD 15**, **RD 16**]. This also jeopardizes the multiplex advantage of FTS. The quantitative structure of the modulus spectrum of a shifted interferogram is unchanged. A better practice is to average spectra. Hence spectra can be averaged validly. This and the fact that FCE detection is easier to perform in the spectral domain have favored SDR Algorithms design to opt for this approach on raw spectra.

In order to achieve the requested radiometric accuracy, calibration measurements (cold DS and hot ICT) must be coadded together in order to increase the SNR. The chosen method is a moving average that coadds the N^{ma} (= 30 or less) closest in time equivalent measurements in order to estimate background radiance and gain.

5.5.1 Moving Average

The moving average is defined as follows:

$$\langle T_j \rangle = \frac{1}{N^{ma}} \sum_{i=j-N^{ma}/2}^{j+N^{ma}/2-1} T_i \,, \tag{79}$$

that is, a simple averaging inside a small moving window.

Before the coaddition is performed, individual interferograms of a sequence need to have a common fringe count alignment. This is why a FCE detection/correction is applied to each spectrum before being inserted into the moving average.

The moving average concept can be summarized as follows:

keep in memory N^{ma} (= 30 as a baseline) different sweeps, and sequentially update each one of these window elements,

recompute the mean of all window elements when requested.

The complete re-updating of the calibration moving window takes 4 minutes.

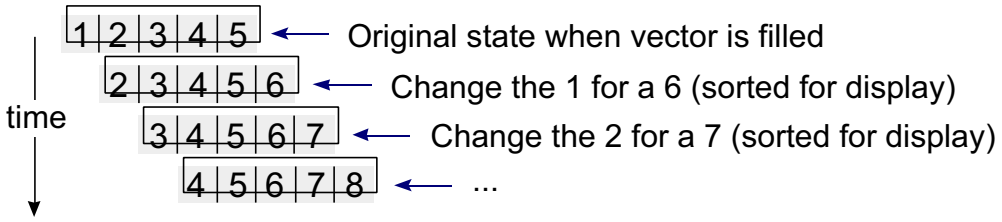

Figure 33: Moving average window updating (example case N^{ma} = 5)

Moving windows are considered un-weighted (each element has an equal importance) in order to maintain an equal signal to noise ratio.

The spectral coaddition is a simple point-by-point addition and is expressed by:

$$\left\langle \tilde{S}^{X}[n] \right\rangle = \frac{1}{N^{ma}} \sum_{i=0}^{N^{ma}-1} W\_\tilde{S}^{X}[i][n] \tag{80}$$

where the various terms are described in Section 7.6.

The coaddition should also take into account the moving average of the temperature parameters. This is done as follows:

$$T^{Y} = \frac{1}{N^{ma}} \sum_{i=0}^{N^{ma}-1} W\_T^{Y}[i] \tag{81}$$

What should be averaged is in reality the blackbody radiance corresponding to each ICT measurement. But, for simplicity of the processing, we make the following linearity hypothesis:

$$\frac{1}{N} \sum_{i=0}^{N-1} B(T_i) \approx B\left(\frac{1}{N} \sum_{i=0}^{N-1} T_i \right) \tag{82}$$

which is valid in the case of monotonous functions like the Planck distribution for narrow range of temperatures, and wave-numbers. The SDR Algorithms therefore average temperatures, computed from raw instrument readings as described in Section 5.4.1.

5.5.2 Impact of temperature drift

In the CrIS instrument, the ICT is not thermally stabilized. Temperature variations will be present in the moving average window, introducing deviation from the real expected values for the averaged ICT. In order to estimate the error, we computed the difference between the average of blackbodies and a blackbody at the average temperature of those blackbodies, i.e.

$$\varepsilon[\sigma] = 100\,\frac{\frac{1}{N}\sum_{i=1}^{N} B[\sigma, T_i] - B[\sigma, \langle T \rangle]}{B[\sigma, 287]}. \tag{83}$$

We compute also the error on the radiance using the following equation,

$$\mathrm{e} = 100\,\frac{\sum_{\sigma}\left(\frac{1}{N}\sum_{i=1}^{N} B[\sigma, T_i] - B[\sigma, \langle T \rangle]\right)}{\sum_{\sigma} B[\sigma, 287]}. \tag{84}$$

Considering a drift of 0.08 K/min, maximal temperature of 310 K, and a number a samples between 8 and 30, we compute the error caused by the temperature drift. We have assumed a linear temperature drift, which is the worst case. It must be remarked that for ICT temperatures lower than 310 K, the error will be even smaller.

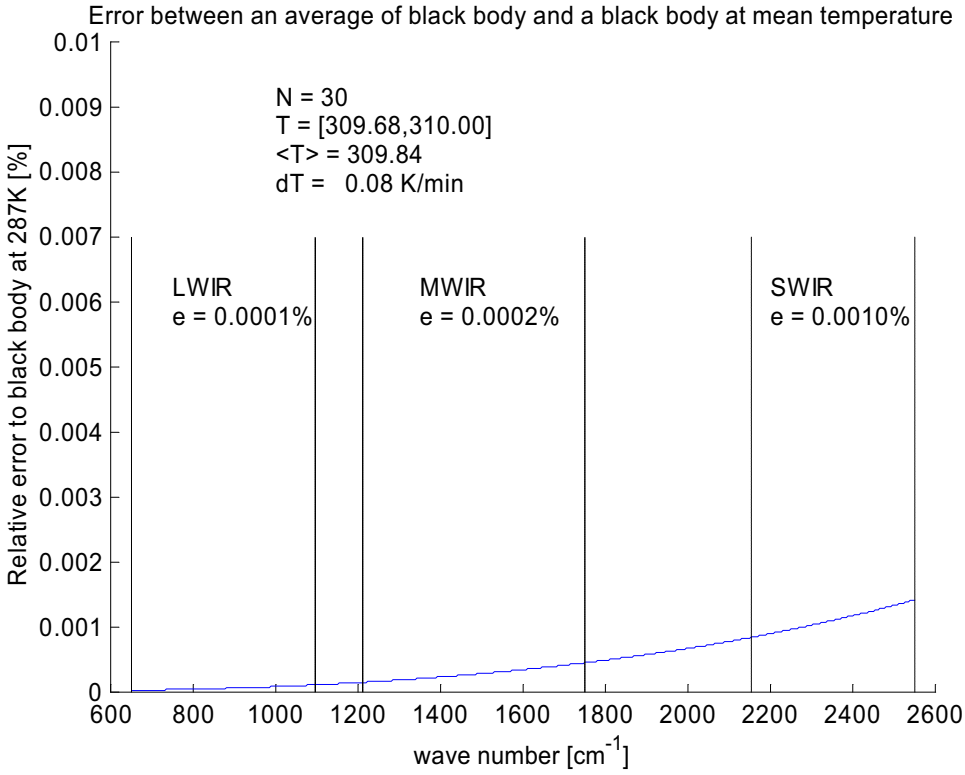

Figure 34: Relative error causes by combining many blackbodies (N=30)

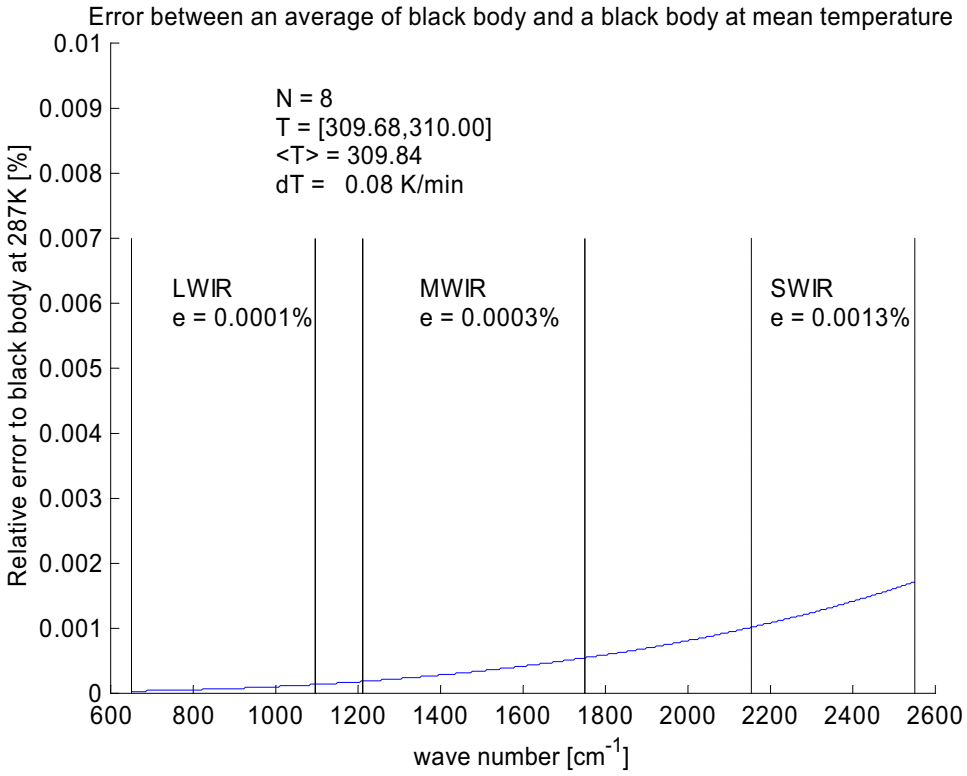

Figure 35: Relative error causes by combining many blackbodies (N=8)

Few remarks must be made about the impact of the temperature drift:

The number of sample has negligible impact on the error,

The error depends primarily on the temperature variation (min/max) inside the moving window,

The error has a quadratic dependency over the temperature differences.

The quadratic dependency of the error over the temperature differences comes from the second order term in the Taylor expansion. In our temperature range, only the linear term dominates. As the temperature differences increase, the quadratic term in the Taylor expansion becomes more important, increasing the error of the linear approximation.

Figures 34 and 35 show clearly the negligible impact of the temperature drift in the radiometric calibration. The worst case is in the SW band, in which the error over the radiance is 13 ppm. We can see that the error is almost the same with 8 or 30 samples.

5.5.3 Throughput delay

The present concept is to pipeline the processing so that SDRs and EDRs are processed in parallel, thus allowing a near full 20 minutes to be allocated to each function. A “throughput delay” of one minute maximum has been defined for the SDR Algorithms and one minute maximum for the EDR algorithms. Throughput delay is the maximum latency occurring by processing an earth scene through the algorithm from input to output. These latencies can be caused by the need to process four minutes worth of on-orbit data that encompass calibration measurements and apply all of these measurements to the single earth scene being processed. Allowing for a one minute throughput delay

in SDR Algorithms and a one minute throughput delay in EDR algorithms leaves 18 minutes of time left for processing the entire block of 1.25 orbits of data.

According to current acquisition plan (see Section 2.5.4) the CrIS collects 34 Fields of Regard (FOR) during each 8-second scan sweep. Four of these are calibration data, while 30 are earth scenes. Each FOR contains 9 Fields of View (FOV). 1.25 orbits of data will thus result in 290 000 FOVs to be processed by the SDR Algorithms within 18 minutes. This then computes to a faster than real-time processing speed of 3.7 ms per FOV for the SDR Algorithms.

The 1.25 $\times$ 101 minutes of orbit data (946 scans) will be transmitted down in 10 minutes, corresponding to a factor 10 faster than real-time processing constant. The N^{ma} moving average window elements need to be filled completely before the computation of the earth scenes calibration begins, in order to reach the proper SNR threshold. Waiting for 30 scans in real-time would take 4 minutes, at 8 sec/scan. But in the faster than real-time processing scheme, this takes 24 seconds. In order to account for the process and loading, this throughput delay is rounded up to 1 minute.

During this waiting time, no SDR outputs are generated. After the pipeline is filled, the SDR Algorithms will hand out calibrated spectra at the requested interval.

Figure 36 summarized the throughput delay in measurement sequence. The mean calibration spectra and associated ICT mean temperatures are computed from a mean of $N^{ma}/2$ before and $N^{ma}/2$ after the requested time, where the middle is the most representative of the true status of the calibration target.

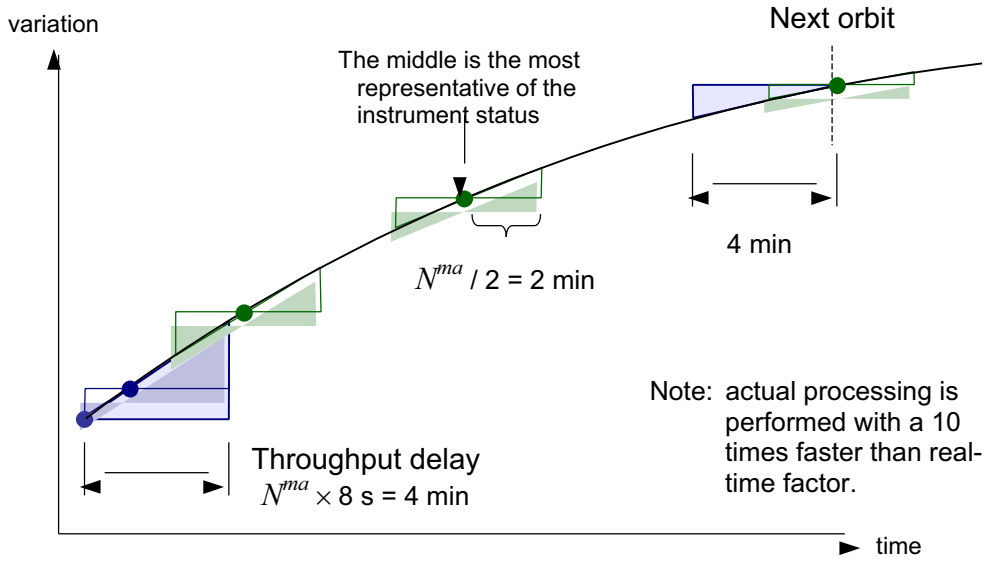

Figure 36: Throughput delay in measurement sequence with $N^{ma}=30$

The moving average of N^{ma} = 30 deep space looks and 30 Internal Calibration Target (ICT) averages are performed 15 samples prior to the earth scene and 15 samples after earth scene. This centering of the calibration averaging is most representative of the instrument background around the time of earth scene measurement. At the beginning of the processing, special mode is commanded for the filling of all the moving average window elements by reading ahead the calibration measurements scans of the orbit.

With a moving window size of $N^{ma}=30$, it takes approximately four minutes of on-orbit data collection to span this ±15 samples of calibration information to support this computation. The present CrIS baseline instrument design is being engineered to maintain better than 0.1% change in instrument radiometric background radiance over four minute intervals such as this. Should this stabilization of the instrument background prove impractical from a cost standpoint, then mathematical interpolation techniques will be added to the averaging algorithms to account for changes in the instrument thermal conditions and/or detector responsivities. The opposite is more likely to happen, where a high stability enables the moving average window to be of a larger size (to increase the SNR).

6. GEOMETRIC CALIBRATION

Geometric calibration is the process of assigning an absolute line of sight (latitude and longitude) pointing values to a given atmospheric spectrum with a specified accuracy. The outputs of the SDR calibration algorithms will therefore be atmospheric spectra (intensity versus frequency) corresponding to precisely known locations.

It is to be expected that the bulk of the geolocation algorithm will be performed once by the TSPR and used for all instrument payloads. The SDR algorithm will merely take lat/long nadir ground tracks and modify this by simple geometry for scan angle, mounting offsets, etc. (TBC). If it is not the case, a generic geolocation algorithm will be used such as described below.

Geometric units are degrees. Navigation, attitude, horizon, and geodetic data are standards.

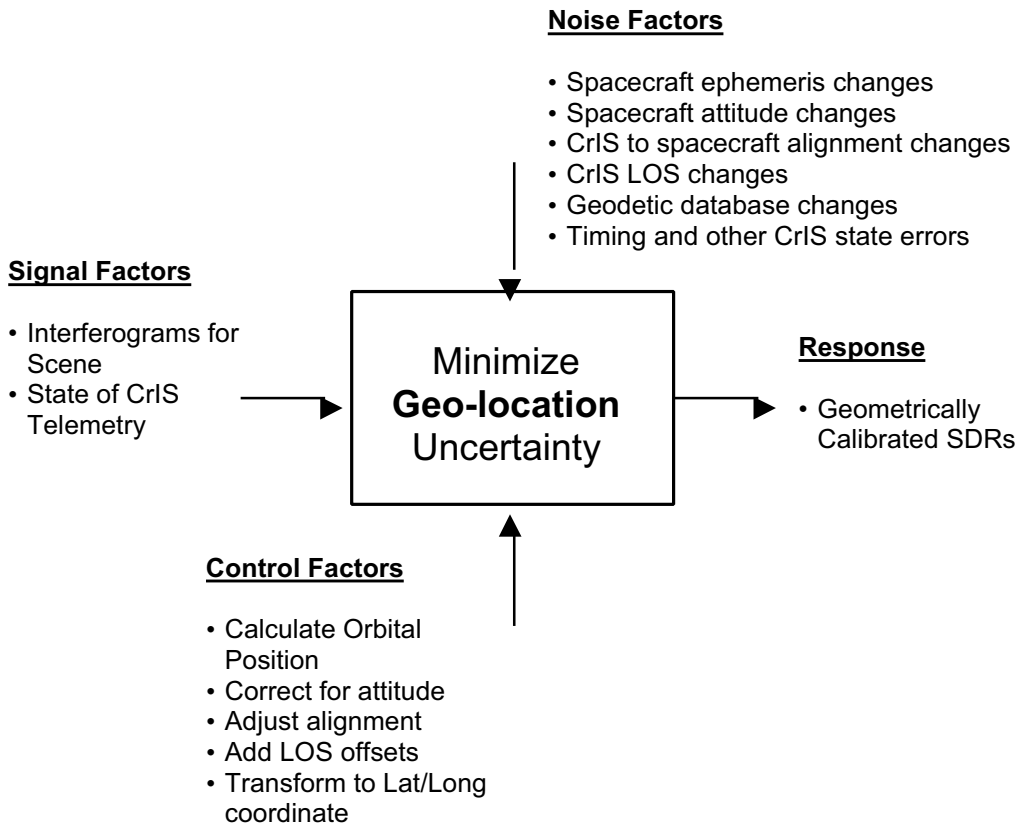

Figure 37: Geometric Calibration Parameter diagram

The main objectives of geometric calibration are:

Compute longitude Λ_C and geodetic latitude Φ_C of the Earth located center of each FOV,

Compute the LOS slant angle Γ of the located measurement (scan angle Θ will also be provided as output),

Compute the geolocation footprint at the surface (pixel size semi-minor and semi-major axes),

Provide the above measurements for each FOV, at sea level (position of each footprint):

- SDR Algorithms concentrate more on sensor calibration,

– This provides an unambiguous output for all users,

– Ground terrain correction is performed at EDR level using an altitude digital map grid.

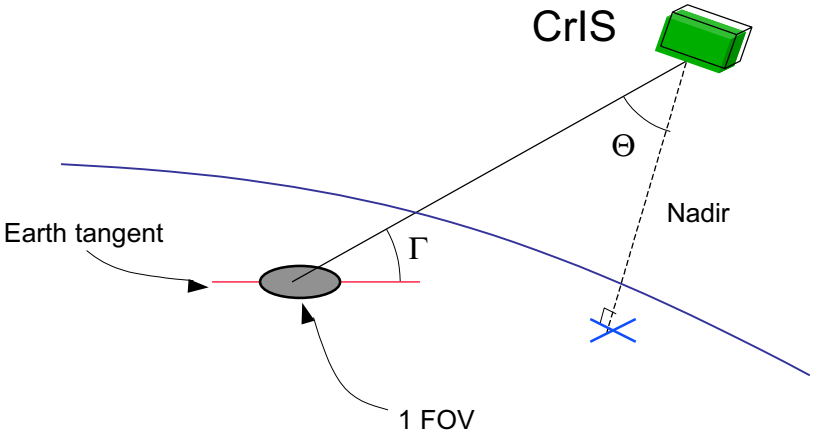

Figure 38: CrIS viewing angle on Earth's surface

The angle Γ is different from scan angle Θ because curvature of the Earth.

6.1 SYSTEM CHARACTERISTICS

The CrIS instrument will have external optical alignment references to define the mechanical reference axes and establish the orientation of the mechanical reference axes relative to the spacecraft primary mechanical axes. For a proper computation of the pointing correction, these mounting angles of the instrument with respect to the spacecraft must be taken into account. The CrIS line-of-sight (LOS) will be defined by the location of the center of the Instantaneous Field-of-Regard with respect to the reference axes defined above.

The line-of-sight pointing knowledge shall be less than or equal to 758 microrads per axis degree for all scan angles relative to the reference axes and less than or equal to 379 microrads per axis degrees for all scan angles relative to each other in both in-track and cross track directions (SRDK3.2.1.37.5-1).

The projection of the CrIS FOVs onto the earth surface constitutes the CrIS FOV ground footprint. Motion of this footprint is a combination of CrIS LOS jitter and the in-track spacecraft tangential motion. The FOV ground footprint motion will be compensated so that the residual motion is less than 0.3% (TBR) of the FOV size (SRDK3.2.1.37.6-1).

The ephemeris (orbit propagator) and attitude generation are the responsibility of the Flight Operating Center and Platform Prime Contractor. Ephemeris data will be available at a 1 second interval, with a precision of 1 ms. Spacecraft ephemeris data (roll-pitch-yaw) will also be available at a 1 second interval and will have to be interpolated between IGM measurements, starting at the beginning of sweep. The corresponding S/C binary time will be given for each of these parameters. There is a 5 km expected accuracy on ground positions, but SDR Algorithms will output a 1 km accuracy (coming from the absence of elevation correction).

Required input:

– S/C ephemeris (1 Hz)

- S/C roll, pitch, yaw (1 Hz)
- S/C binary time (1 Hz)
- UTC at start of interferogram
- CrIS scan angle
- CrIS to S/C alignment
- Ellipsoid model of Earth

6.2 FIELD-OF-VIEW LOCATION

It is essential in interpreting the CrIS radiance measurements that the geographic location falling within the detector field of view be accurately determined for each measurement. The input data required to perform the geolocation procedure include the spacecraft ephemeris and attitude, the detector pointing knowledge, an ellipsoid model of the Earth, and the time [RD 17]. First, the spacecraft position vector and the detector pointing vector are transformed into an Earth fixed coordinate system. The equation of the line passing through the spacecraft position and parallel to the detector pointing vector is then determined and combined with the Earth ellipsoid equation to form a system of equations. Finally, the solution of the system determines the points of intersection between the line and the ellipsoid. The geometry of the procedure is illustrated in Figure 39. The geographic location observed in the detector field of view is the intersection point closest to the spacecraft. The alternate intersection solution on the far side of the Earth is also shown.

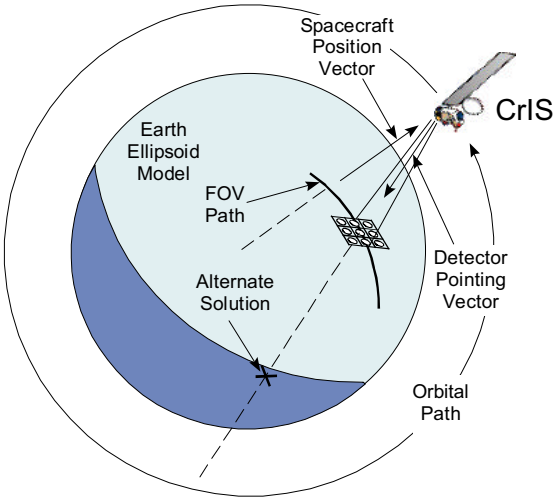

Figure 39: Geometry of the detector field of view and Earth ellipsoid intersection.

The orientation of the Earth's equatorial plane with respect to the plane of its orbit about the Sun is illustrated in Figure 40. The axes of the geocentric-equatorial coordinate system (designated by X_I, Y_I, and Z_I) are defined with respect to these planes. The X_I-axis is the intersection of the planes, and the Z_I-axis is normal to the equatorial plane. The positive direction of the X_I-axis is from the Sun to the Earth during the autumnal equinox, as illustrated in Figure 40. The positive direction of the Z_I-axis is from the Earth's center to the north pole. The positive Y_I-axis completes a right handed coordinate system. This coordinate system does not rotate with the Earth and makes up the inertial frame that is used to report the spacecraft ephemeris. The position vector for the spacecraft reported in the ephemeris data is designated by X_I, Y_I, and Z_I.

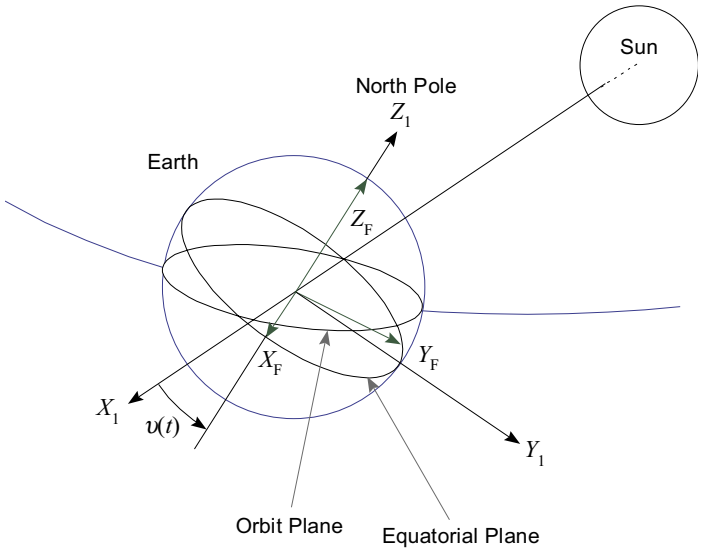

Figure 40: Orientation of the inertial and Earth fixed coordinate systems with respect to the equatorial and orbital planes.

The Earth's rotation causes the Earth fixed coordinate system (designated by X_F, Y_F, and Z_F) to rotate with respect to the inertial system as a function of time. The rotation of the Earth fixed frame is illustrated in Figure 40. The spacecraft position vector is transformed into Earth fixed coordinates by

$$\begin{bmatrix} X_F \\ Y_F \\ Z_F \end{bmatrix} = \begin{bmatrix} \cos(\nu(t)) & \sin(\nu(t)) & 0 \\ -\sin(\nu(t)) & \cos(\nu(t)) & 0 \\ 0 & 0 & 1 \end{bmatrix} \begin{bmatrix} X_I \\ Y_I \\ Z_I \end{bmatrix} \tag{85}$$

which is a rotation about the Z_I-axis, where $\nu(t)$ is the time dependent rotation angle of the Earth fixed frame with respect to the inertial frame and is given by

$$\nu = 99.6909833° + 36000.7689°t + 0.00038708°t^2 + 360.9856463°\Delta d \tag{86}$$

where t is in Julian centuries since 1900 and Δd is fractional days between the measurement time and midnight universal time.

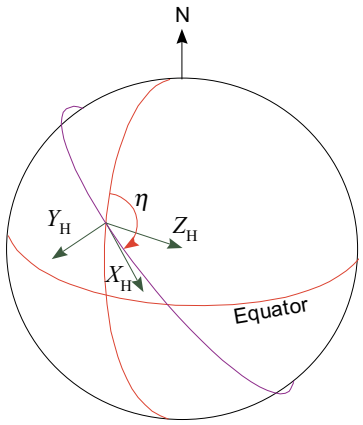

Figure 41: Orientation of the detector field of view with respect to the spacecraft and local horizon coordinate systems.

The orientation of the instrument in the spacecraft coordinate system (designated by X_S, Y_S, and Z_S) is illustrated in Figure 41, for the crosstrack mode, at the instant of nadir viewing. During nominal operations, the spacecraft coordinate system is aligned with the local horizon coordinate system (designated by X_H, Y_H, and Z_H). Therefore, X_S and X_H point along the projection of the spacecraft velocity vector in the local horizon plane, Z_S and Z_H point to the geodetic nadir, and Y_S and Y_H complete the right handed coordinate systems, pointing along the negative orbit momentum vector. The detector has two degrees of freedom relative to the instrument. The instrument is aligned during integration with the spacecraft so that values of zero for the azimuth and elevation angles will point the detector along the orbit momentum vector of the spacecraft. If the alignment is done perfectly, the detector pointing vector in spacecraft coordinates is given by:

$$\begin{bmatrix} X_S \\ Y_S \\ Z_S \end{bmatrix} = \begin{bmatrix} \cos(\alpha) & -\sin(\alpha)\cos(\beta) & -\sin(\alpha)\sin(\beta) \\ \sin(\alpha) & \cos(\beta)\cos(\alpha) & \sin(\alpha)\cos(\alpha) \\ 0 & -\sin(\beta) & \cos(\beta) \end{bmatrix} \begin{bmatrix} 0 \\ -1 \\ 0 \end{bmatrix} \tag{87}$$

where α is the azimuth angle and β is the elevation angle. The orientation of the detector as shown in Figure 41 is for α = 180° and β = 90°.

The roll, pitch, and yaw angles of the spacecraft in orbit will not generally be zero, so the spacecraft will be rotated with respect to the local horizon. The equation that transforms the detector pointing vector from the spacecraft coordinate system to the local horizon coordinate system is

$$\begin{bmatrix} X_H \\ Y_H \\ Z_H \end{bmatrix} = \begin{bmatrix} \cos q \cos r - \sin p \sin q \sin r & -\sin r \cos p & \sin p \sin r \cos q \\ \sin r \cos q + \sin p \sin q \cos r & \cos p \cos r & \sin q \sin r - \sin p \cos q \cos r \\ -\sin q \cos p & \sin p & \cos p \cos q \end{bmatrix} \begin{bmatrix} X_S \\ Y_S \\ Z_S \end{bmatrix} \tag{88}$$

where p, q, and r represent roll, pitch, and yaw angles of the spacecraft about the X_H, Y_H, and Z_H axes, respectively.

The CrIS will use the coordinate system for the vertical reference axis (Z) and perpendicular azimuth axes shown in the Figure 42. $+Z$ is the nadir (or spacecraft yaw) axis, $+Y$ is the anti-sun (or spacecraft pitch) axis, and $+X$ is the velocity (or spacecraft roll) axis. These axes will be used for alignment of the CrIS LOS and the overall alignment of the CrIS to the NPOESS spacecraft.

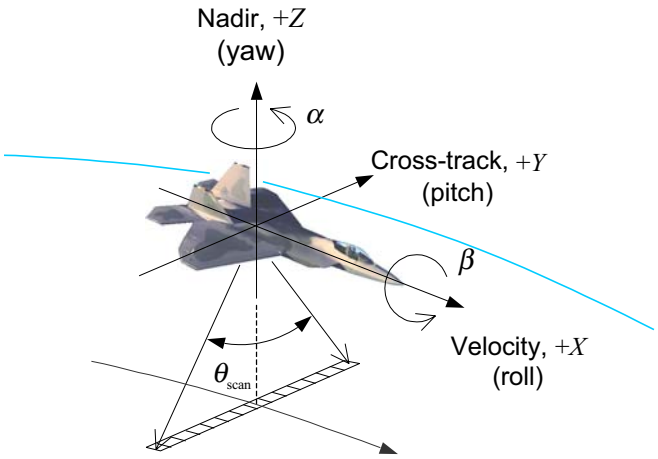

Figure 42: Reference Axes and Attitude definition

The local horizon coordinate system is rotated about nadir with respect to the local geodetic coordinate system as a result of the inclination of the orbit, as shown in Figure 42. The rotation angle η, called the heading angle, is the angle between geodetic north and the projection of the spacecraft velocity vector onto the local horizon coordinate system. The detector pointing vector is both rotated by the heading angle and transformed to the Earth fixed geocentric-equatorial coordinate system by

$$\begin{bmatrix} X_F \\ Y_F \\ Z_F \end{bmatrix} = \begin{bmatrix} -\cos\eta\cos\Lambda\sin\Phi_G + \sin\eta\sin\Lambda & -\sin\eta\cos\Lambda\sin\Phi_G - \cos\eta\sin\Lambda & -\cos\Lambda\cos\Phi_G \\ -\cos\eta\sin\Lambda\sin\Phi_G - \sin\eta\cos\Lambda & -\sin\eta\sin\Lambda\sin\Phi_G + \cos\eta\sin\Lambda & -\sin\Lambda\cos\Phi_G \\ \cos\eta\cos\Phi_G & \sin\eta\cos\Phi_G & -\sin\Phi_G \end{bmatrix} \begin{bmatrix} X_H \\ Y_H \\ Z_H \end{bmatrix} \quad (89)$$

where Λ and Φ_G are the Earth fixed longitude and geodetic latitude of the spacecraft. The Earth fixed longitude and geocentric latitude are derived from Equation (85). The geodetic latitude is determined from the geocentric latitude Φ_C by:

$$\Phi_G = \tan^{-1}\left(\tan\Phi_C \frac{R_e^2}{R_p^2}\right) \quad (90)$$

where R_e and R_p are the equatorial and polar radii, respectively.

The Earth ellipsoid model is given by:

$$\frac{X^2}{(R_e+h)^2} + \frac{Y^2}{(R_e+h)^2} + \frac{Z^2}{(R_p+h)^2} = 1 \quad (91)$$

where h is a top of atmosphere reference height above the Earth of 30 kilometers (can be put to $h = 0$, TBC). The equation for the line passing through the spacecraft position and parallel to the detector pointing vector is

$$\frac{X - X_0}{a} = \frac{Y - Y_0}{b} = \frac{Z - Z_0}{c} \quad (92)$$

where a, b, and c are the components of the detector pointing vector from Equation (88), and X_0, Y_0, and Z_0 are the Earth fixed coordinates of the spacecraft from Equation (85). The solutions of system of Equations (91) and (92) are the Earth fixed coordinates of the detector FOV intersection point (designated as X_F, Y_F, and Z_F) and an alternate intersection point on the far side of the Earth ellipsoid from the spacecraft.

Finally, the latitude and longitude of the Earth located measurement in Earth fixed geocentric coordinates are:

$$\Phi_C = \sin^{-1}\left(\frac{Z_F}{|\vec{R}_F|}\right) \tag{93}$$

$$\Lambda_C = \tan^{-1}\left(\frac{Y_F}{X_F}\right) \tag{94}$$

6.3 SEQUENCE OF TRANSFORMATIONS

Considering that we can associate to every interferogram:

State Vector

the S/C position in geocentric-equatorial coordinate system

$$\mathbf{R}_I = \begin{pmatrix} X_I \\ Y_I \\ Z_I \end{pmatrix},$$

the S/C velocity in geocentric-equatorial coordinate system

$$\mathbf{V}_I = \begin{pmatrix} V_{X_I} \\ V_{Y_I} \\ V_{Z_I} \end{pmatrix},$$

the S/C attitude, i.e. roll (p), pitch (q) and yaw(r),

CrIS viewing angles

- α cross-track angle around instrument X-axis
- β elevation angle around instrument Z-axis,

and determine during ground characterization:

LOS unit vector $\mathbf{U}_p$ for each of the nine (9) pixels,

CrIS mounting offset X-convention Euler angles (ϕ,θ,ψ) bringing instrument coordinate system on S/C coordinate system,

then, the following sequence of operations provide the output values required for the geometric calibration module.

1. LOS of pixel p with respect to instrument coordinate system:

$$\mathbf{LOS}_I = \begin{pmatrix} \cos(\alpha) & -\sin(\alpha)\cos(\beta) & -\sin(\alpha)\sin(\beta) \\ \sin(\alpha) & \cos(\beta)\cos(\alpha) & \sin(\alpha)\cos(\alpha) \\ 0 & -\sin(\beta) & \cos(\beta) \end{pmatrix} \mathbf{U}_p \tag{95}$$

2. LOS with respect to S/C coordinate system (dropping index p for clarity):

$$\mathbf{LOS}_{\mathrm{S/C}} = \begin{pmatrix} \cos\psi\cos\phi & -\sin\psi\cos\phi & \sin\theta\sin\phi \\ -\cos\theta\sin\phi\sin\psi & -\cos\theta\sin\phi\cos\psi & \\ \cos\psi\sin\phi & -\sin\psi\sin\phi & -\sin\theta\cos\phi \\ +\cos\theta\cos\phi\sin\psi & +\cos\theta\cos\phi\cos\psi & \\ \sin\theta\sin\psi & \sin\theta\cos\psi & \cos\theta \end{pmatrix} \mathbf{LOS}_I$$

3. LOS with respect to local horizon coordinate system:

$$\mathbf{LOS}_{\mathrm{H}} = \begin{pmatrix} \cos q\cos r & -\sin r\cos p & \sin p\sin r\cos q \\ -\sin p\sin q\sin r & & \\ \sin r\cos q & \cos p\cos r & \sin q\sin r \\ +\sin p\sin q\cos r & & -\sin p\cos q\cos r \\ -\sin q\cos p & \sin p & \cos p\cos q \end{pmatrix} \mathbf{LOS}_{\mathrm{S/C}} \tag{96}$$

4. Heading angle evaluation:

   Projection of S/C velocity in local horizon plane:

$$\mathbf{V}_{P\cdot LH} = \frac{(\mathbf{R}_I \times \mathbf{V}_I)\times \mathbf{R}_I}{|\mathbf{R}_I|^2} \tag{97}$$

$$\eta = \arccos\left(\frac{V_{Z_{P\cdot LH}}}{|\mathbf{V}_{P\cdot LH}|}\right) \tag{98}$$

5. S/C position in Earth-fixed coordinate system:

$$\begin{pmatrix} X_F \\ Y_F \\ Z_F \end{pmatrix} = \begin{pmatrix} \cos\nu(t) & \sin\nu(t) & 0 \\ -\sin\nu(t) & \cos\nu(t) & 0 \\ 0 & 0 & 1 \end{pmatrix} \begin{pmatrix} X_I \\ Y_I \\ Z_I \end{pmatrix} \tag{99}$$

6. S/C longitude and geodetic latitude in Earth-fixed coordinate system:

$$\Lambda = \arctan\left(\frac{Y_F}{X_F}\right) \tag{100}$$

$$\Phi_G = \arctan\left(\frac{R_e^{\,2}}{R_p^{\,2}}\tan\left(\arcsin\left(\frac{Z_F}{|\mathbf{R}_F|}\right)\right)\right) \tag{101}$$

7. LOS in Earth-fixed coordinate system:

$$\mathbf{LOS}_F = \begin{pmatrix} -\cos\eta\cos\Lambda\sin\Phi_G + \sin\eta\sin\Lambda & -\sin\eta\cos\Lambda\sin\Phi_G - \cos\eta\sin\Lambda & \cos\Lambda\cos\Phi_G \\ -\cos\eta\sin\Lambda\sin\Phi_G - \sin\eta\cos\Lambda & -\sin\eta\sin\Lambda\sin\Phi_G + \cos\eta\cos\Lambda & -\sin\Lambda\cos\Phi_G \\ \cos\eta\cos\Phi_G & \sin\eta\cos\Phi_G & -\sin\Phi_G \end{pmatrix} \mathbf{LOS}_H \tag{102}$$

8. Compute FOV for the given pixel:

Given

$$\begin{aligned} a &= (\mathbf{LOS}_F)_X \\ b &= (\mathbf{LOS}_F)_Y \\ c &= (\mathbf{LOS}_F)_Z \end{aligned} \tag{103}$$

and

$$\begin{aligned} A &= \frac{a^2}{R_e^{\,2}} + \frac{b^2}{R_e^{\,2}} + \frac{c^2}{R_p^{\,2}} \\ B &= \frac{2aX_F}{R_e^{\,2}} + \frac{2bY_F}{R_e^{\,2}} + \frac{2cZ_F}{R_p^{\,2}} \\ C &= \frac{X_F^{\,2}}{R_e^{\,2}} + \frac{Y_F^{\,2}}{R_e^{\,2}} + \frac{Z_F^{\,2}}{R_p^{\,2}} - 1 \\ \Delta &= \frac{-B \pm \sqrt{B^2 - 4AC}}{2A} \end{aligned} \tag{104}$$

and since $|\Delta|$ is the distance between S/C and FOV, choosing the sign for the smallest $|\Delta|$ determines the FOV position:

$$\begin{aligned} X_{FOV} &= X_F + a\Delta \\ Y_{FOV} &= Y_F + b\Delta \\ Z_{FOV} &= Z_F + c\Delta \end{aligned} \tag{105}$$

9. FOV center latitude and longitude in Earth-fixed geocentric coordinate system:

$$\begin{aligned} \Phi_C &= \arcsin\left(\frac{Z_{FOV}}{|\mathbf{R}_{FOV}|}\right) \\ \Lambda_C &= \arctan\left(\frac{Y_{FOV}}{X_{FOV}}\right) \end{aligned} \tag{106}$$

10. Cosine director for FOV position vector ($\mathbf{R}_{FOV}$), S/C position vector ($\mathbf{R}_F$) and FOV to S/C vector ($\mathbf{R}_{FOV} - \mathbf{R}_F$):

$$\begin{aligned} l_{FOV} &= \frac{X_{FOV}}{|\mathbf{R}_{FOV}|} \\ m_{FOV} &= \frac{Y_{FOV}}{|\mathbf{R}_{FOV}|} \\ n_{FOV} &= \frac{Z_{FOV}}{|\mathbf{R}_{FOV}|} \end{aligned} \tag{107}$$

$$\begin{aligned} l_{\mathrm{S/C}} &= \frac{X_F}{|\mathbf{R}_F|} \\ m_{\mathrm{S/C}} &= \frac{Y_F}{|\mathbf{R}_F|} \\ n_{\mathrm{S/C}} &= \frac{Z_F}{|\mathbf{R}_F|} \end{aligned} \tag{108}$$

$$\begin{aligned} l_{FOV-\mathrm{S/C}} &= \frac{X_{FOV} - X_F}{|\Delta|} \\ m_{FOV-\mathrm{S/C}} &= \frac{Y_{FOV} - Y_F}{|\Delta|} \\ n_{FOV-\mathrm{S/C}} &= \frac{Z_{FOV} - Y_F}{|\Delta|} \end{aligned} \tag{109}$$

11. Viewing angle (Θ):

$$\Theta = \arccos\left(l_{\mathrm{S/C}} l_{FOV\text{-}\mathrm{S/C}} + m_{\mathrm{S/C}} m_{FOV\text{-}\mathrm{S/C}} + n_{\mathrm{S/C}} n_{FOV\text{-}\mathrm{S/C}}\right) \tag{110}$$

12. Slant angle (Γ):

$$D = \left| l_{FOV} X_F + m_{FOV} Y_F + n_{FOV} Z_F - |\mathbf{R}_{FOV}| \right| \tag{111}$$

$$\Gamma = \arcsin\left(\frac{D}{\Delta}\right) \tag{112}$$

6.4 PIXEL SIZE COMPUTATION

The pixel size computation is done according to a specific geometrical calculation done by ITT and it is not reproduced here.

6.5 TIME REPRESENTATION

Different time definitions are needed to fulfill the SDR computation requirements within the ground segment. A continuous time, like the elapsed time (ET) or the International Atomic Time (TAI), is needed for the S/C orbital motion computation in the GEI coordinate frame. Moreover, for data time tagging in the EDR database, a universal time, e.g. the Universal Time Coordinated (UTC), stating the year, month, day and time of day of every measurement has to be used. Finally, for S/C positioning in earth-fixed reference frame and FOV definition purpose, Universal Time 1 (UT1) is also needed. UT1 is a time reference that conforms, within a close approximation, to mean diurnal motion of the Earth.

Thus, all time stamps giving the On Board Time (OBT) of every measurement process are given within the Satellite Binary Time (SBT) reference. The time counter of each instrument is thus synchronized with the S/C SBT time counter.

Since all measurement events should be time referenced using the Modified Julian Day format, the UTC and SBT stamps of the beginning of the data transfer is necessary for time conversion of all registered events.

Auxiliary time data in the ground segment should contain the leap second insertion schedule updated with the *Special Bulletin C* of the International Earth Rotation Service (IERS). And since the UTC is piecewise uniform and continuous, i.e. the time difference between UTC and ET or TAI is equal to an integer number of seconds and is constant except for those occasional jumps from inserted leap seconds, a trivial back conversion to TAI will allow the computation of S/C orbital propagation.

$\Delta\mathrm{UT1} = \mathrm{UT1} - \mathrm{UTC}$ is the increment to be applied to UTC to give UT1, expressed with a precision of 0.1 seconds, and which is broadcast, and any change announced in a *Bulletin D*, by the IERS. $\Delta\mathrm{UT1}$ usually changes 1–2*ms*

Table 15: Various time definitions

Time reference	Definition
ET or TAI	True elapsed time
UTC (Universal Time Coordinated)	Used for reference on earth (previously called Greenwich Mean Time)
UT1	Used as time reference for all orbit state vectors.
SBT (Satellite Binary Time)	S/C time counter coded on a series of bits and incremented at a given frequency.
OBT (On-Board Time)	Generic term to represent any instrument time counter. Usually synchronized on SBT
MJD (Modified Julian Date)	Time format giving the interval of time in days and fraction of day since 2000 January 1 at 00:00:00.000000

7. MODULES DEFINITION

This chapter describes the current implementation details of each module required to perform the CrIS SDR Algorithms. The overall processing chain, divided into its high-level functions, is partitioned as shown in Table 16. The detailed architecture presented in this section is under revision and will be updated in the next SDR ATBD release.

Initialization
- Spectral calibration
  - Laser wavelength calculation from 128 neon fringe count measurements
- CMO calculation

Pre-processing
- Load and sort data
  - CCSDS unpacking
  - Bit Trimming decoding
  - Dual ADC electronic calibration/reconstruction
- Metrology wavelength monitoring
- Spectra computation
  - FFT
  - Spectral re-labeling
  - Alias unfolding

Quality Control
- Identifiers
- Quality control flags
- Noise estimates
- Fringe count error handling

Radiometric Calibration
- Moving average
- Complex calibration equation
- Polarization correction

Spectral Correction
- Correction matrix operator

Geolocation

Postprocessing
- SDR Data Output

Table 16: List of SDR Algorithms Partitions and Modules

The “Spectral calibration module” module calculates the laser diode wavelength based on neon lamp observations as soon as the first calibration data packet is received. It calls the "CMO

calculation" module when it happens that the calculated wavelength differs from some nominal value by more than a specified quantity.

The “CMO calculation” module calculates the correction matrix operator (CMO) used to resample, correct and apodize the calibrated spectra. This module is called whenever appropriate by the "Spectral calibration" module and the "Metrology wavelength monitoring" module.

The “Load and sort data” module extracts packets sequentially from on-board instrument data packages and constructs complete interferograms (decommutation). These are sorted according to scan, FOR, FOV (pixel) and band, before being sent to the proper function depending on the type of data.

The “Metrology wavelength monitoring” module monitors the laser diode wavelength with the help of a temperature and bias current dependent parametric model. It commands CMO recalculation if laser wavelength has drift more than a specified value.

The “Spectra computation” module generates spectra from incoming interferograms. Fourier transforms are computed, followed by spectral axis definition and alias unfolding.

The “Fringe Count Error handling” module handles fringe count errors detection and correction between calibration and scene measurements. FCEs are computed from the extracted phase from raw spectra. A validity check is performed on each processed signal. When a FCE is detected, signals are corrected by the multiplication by a phase correction.

The “Radiometric Calibration” module performs the processing of the scene measurements and generates a radiometrically calibrated spectra. This function makes usage of current mean of calibration measurements (moving average). Polarization and scan mirror gain correction is performed at the same time.

The “Spectral Correction” module performs spectral interpolation, self-apodization removal, and signal apodization with a single matrix multiplication (the CMO).

The “Health Monitoring” module performs ensures that the output spectra are exempt from remaining uncorrected phase errors. Analysis of the imaginary part of the calibrated signal is also performed, and statistics are accumulated to give a low resolution NESR estimate of each spectrum.

The “Geometric Calibration” module computes the latitude and longitude of the LOS associated with each FOV. In addition, it computes the slant path angle and the pixel size at the earth surface.

The “SDR Data Output” module writes SDRs to files in a well defined format such that SDRs are ready to be load and used by EDR algorithm.

7.1 GENERAL FLOW DIAGRAM

The assumed functions and the processing flow of the CrIS Ground Segment are illustrated in Figure 43. The detailed description of the major functions and sub-functions including the objectives, the detailed structure, the computational sequence, the definition of variables, and the algorithms, is given in the following sections.

The conventions used in all the flowcharts of this document are described below:

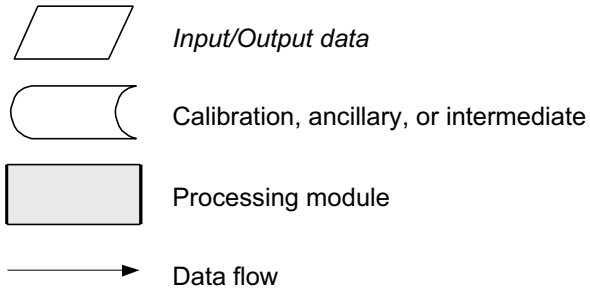

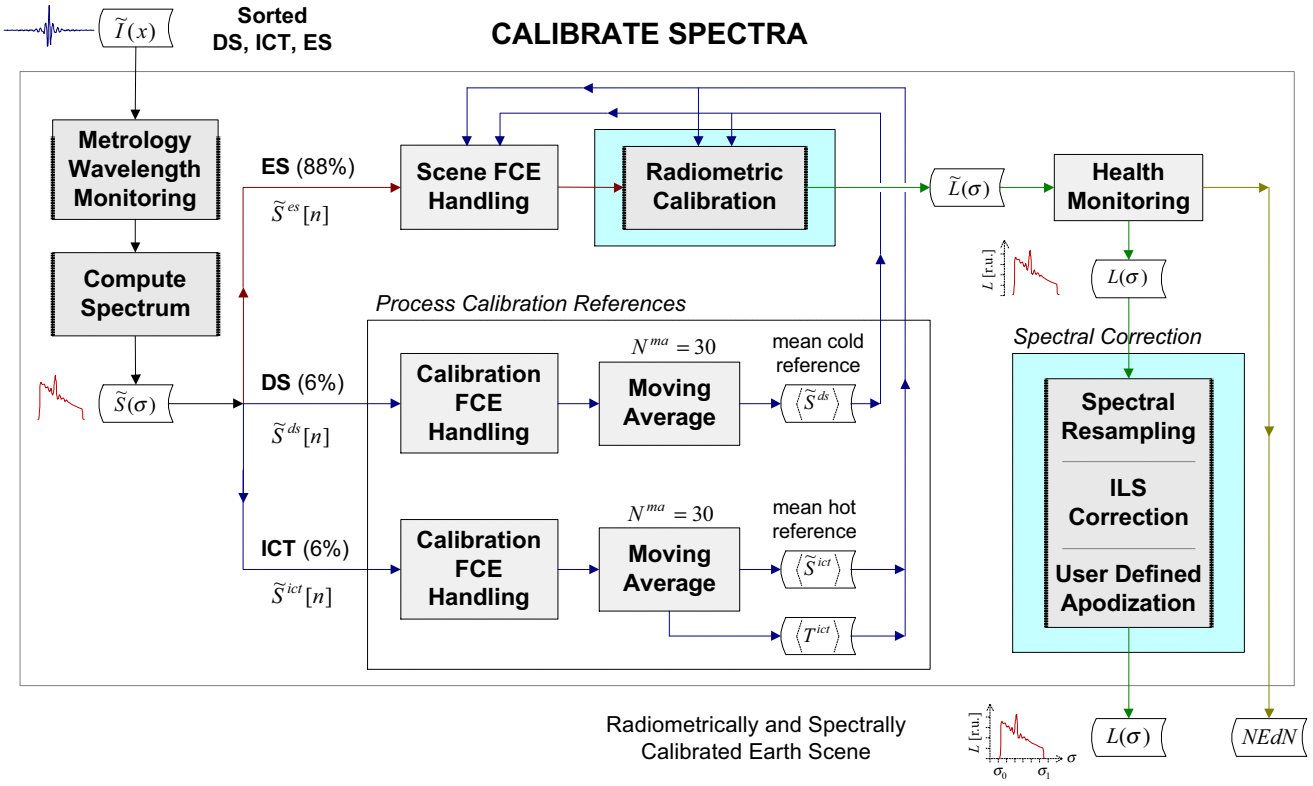

Figure 43: General flow diagram for the Radiometric and Spectral calibration

7.2 LOAD AND SORT DATA MODULE

The purpose of the *Load Data* function is to perform initial processing of all incoming instrument data packets which have to be decoded, demultiplexed, and time ordered. The decoded packets are sequentially extracted and converted into single measurements properly identified and grouped, i.e. the function constructs complete interferograms or calibration measurements. The extracts packet operation performs de-packetizing (unpacking), and decompresses interferograms from bit trimming. Transmission error correction is part of the ground segment system and is not discussed here.

Data are separated according to data type of (DS, ICT, ES measurements, calibration, or data, geometric data), IR band (LW, MW, SW), and IGM sweep direction (forward or reverse) before being sent to the respective SDR algorithm modules. Figure 44 summarizes the corresponding data flow.

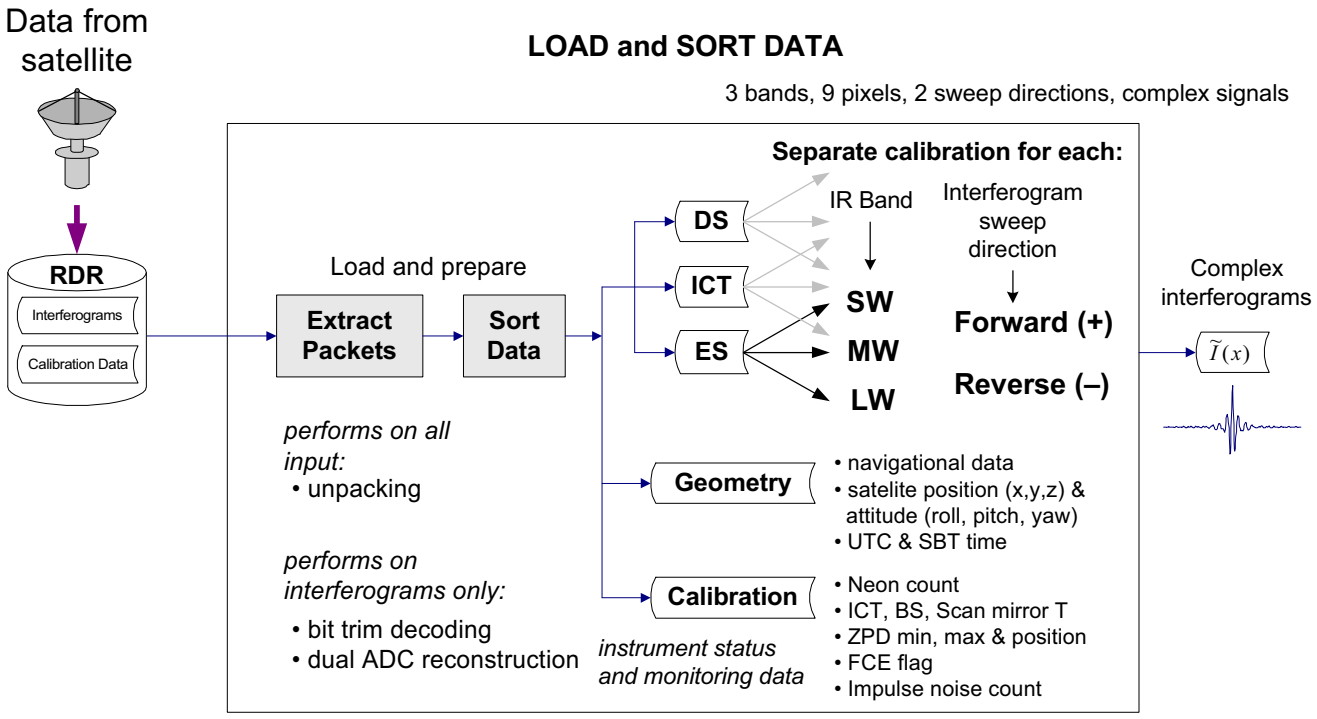

Figure 44: Load and Sort Data Module Flow Chart

Each incoming interferograms will have two extra points used for ZPD position imprecision. This module decides which two points to drop, being either the 2 first, the 2 last, or the first and the last. This procedure is still TBD.

7.3 COMPUTE SPECTRUM MODULE

The Compute Spectrum module performs the Fourier transform of incoming interferograms. This operation is followed by the definition of the corresponding spectral axes. Alias unfolding is performed with the purpose of re-ordering spectra computed from decimated interferograms. A general description of the process is given in Chapter 4. The computational sequence of this function is illustrated by the flowchart of Figure 45.

The fast Fourier transform (FFT) of a sampled interferogram provides a set of spectral radiances uniformly spaced by the *spectral bin* size across the band. The numerical discrete FFT is performed according to an appropriate prime factor algorithm (see Section 9.1). As signals are numerically stored in normal order (see Section 2.6.2), no unswapping is required for adequate phase computation, as the zero frequency corresponds and remains at the first point of the arrays.

The module removes the zero IF offset introduced in space by the sensor prior to filtering and decimation. This is the alias unfolding operation that re-orders spectra computed from decimated interferograms. Appendix 9.2 describes this procedure in details. Relabeling of the spectral axis is also performed, by assigning correct spectral origin and interval special to the current measurement.

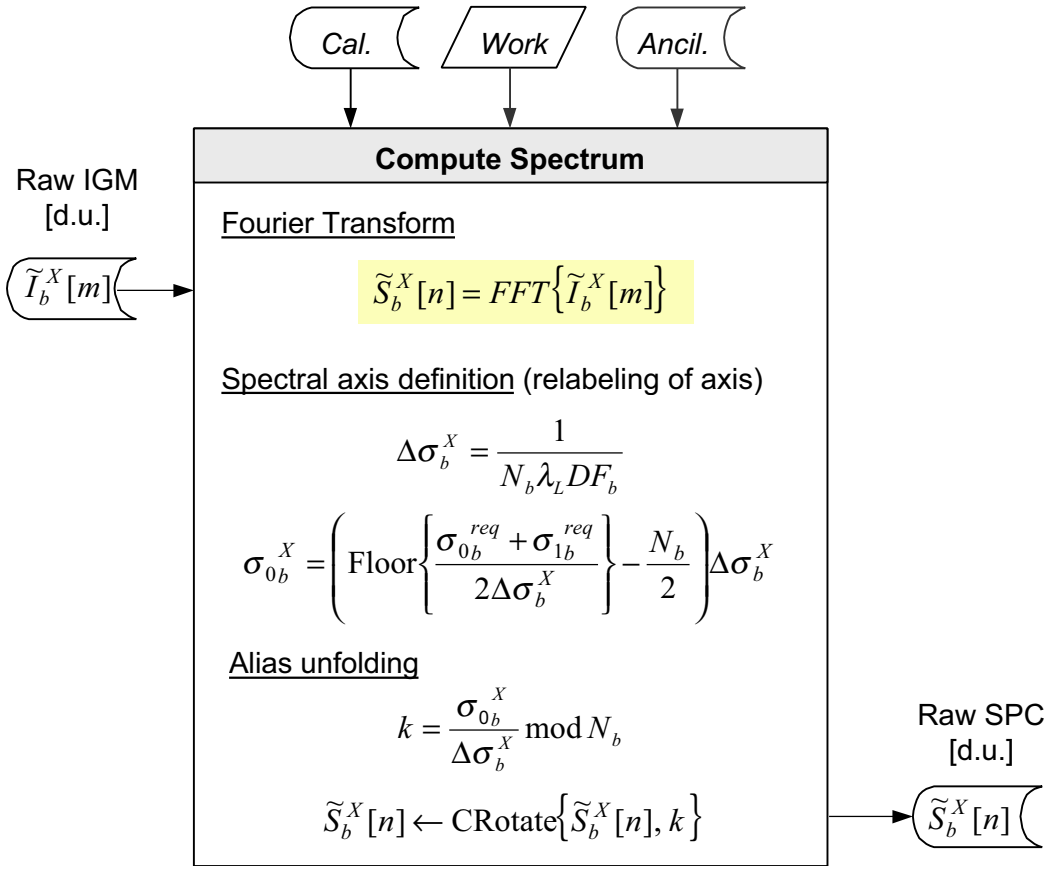

Figure 45: Compute Spectrum Flowchart

The sampling wavelength λ_L value used as a work variable in this module is the last one computed during metrology wavelength calibration.

Figure 46 presents the process for evaluation the laser wavelength at the time of neon calibration, operation performed once per orbit. If it is found that the wavelength has drifted, a recomputation of the CMO matrix is commanded, as described in Section 3.4.

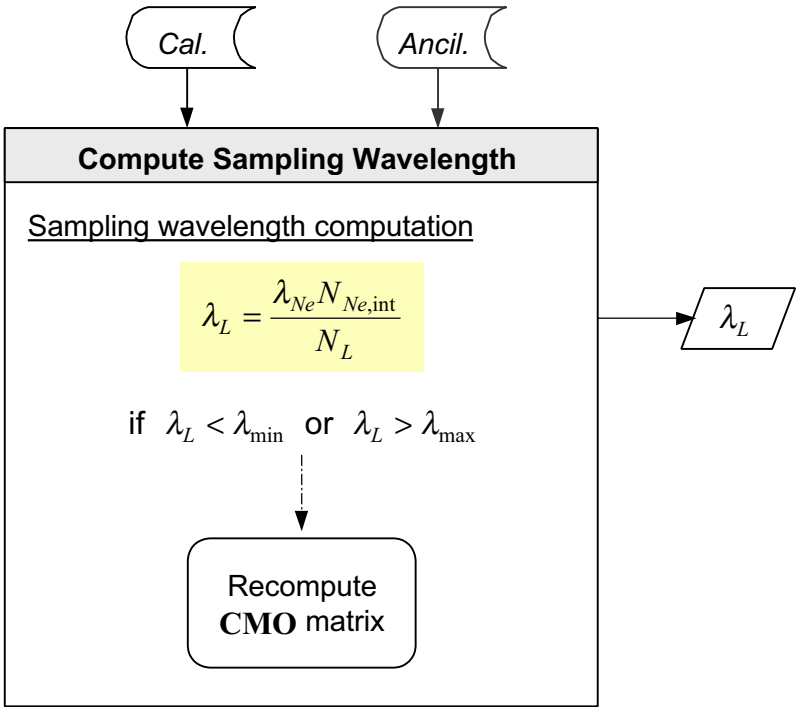

Figure 46: Compute Sampling Wavelength Flowchart

7.3.1 Definition of variables

Input variables

$\tilde{I}^X_{b,p,d}[m]$ raw complex interferogram in [d.u.], corresponding either to X = DS, ICT, or ES.

Calibration data

$N_{Ne,\text{int}}$ interpolated neon fringe count (obtained during last neon spectral calibration).

N_L reference laser fringe count (obtained during last neon spectral calibration).

L_{bc} Laser bias current (obtained during last neon spectral calibration).

T_L Laser temperature (obtained during last neon spectral calibration).

Ancillary data

$\sigma_{0_b}^{req}$ requested minimum band wavenumber value [cm^{-1}].

$\sigma_{1_b}^{req}$ requested maximum band wavenumber value [cm^{-1}] (corresponding to filter limits).

DF_b decimation factor of band b.

λ_{Ne} reference neon wavelength [703.24127 nm].

$\lambda_{\min/\max}$ bracket of valid sampling laser wavenumber (typically 775 nm ±5 nm).

Local variables

k origin point of alias, used as a rotation pivot

Output variables

$\widetilde{S}^{X}_{b,p,d}[n]$ raw complex spectrum in [d.u.], corresponding either to DS, ICT, or ES.

σ^{X}_{0b} signal wavenumber origin for band b [cm^{-1}]

$\Delta\sigma^{X}_{b}$ signal spectral interval [cm^{-1}]

λ_L calculated laser sampling wavelength, outputted for FCE Computation module. $\approx$ 775 nm.

Operators

$\mathrm{CRotate}\{V, k\}$ rotates a complex numerical vector V according to given pivot point k. Rotation is performed to the right for positive values of k.

7.3.2 Exception handling

Computed laser wavelength exceeds expected limits, where the spectral correction matrix CMO must be recomputed. This operation is performed if required just after spectral calibration by the neon subsystem, occurring once per orbit.

7.4 FRINGE COUNT ERROR DETECTION MODULE

The Fringe Count Error handling modules analyzes incoming raw spectra to ensure their phase compatibility before the computation of radiometric calibration. It is necessary to detect fringe count errors before the coaddition of equivalent signals, and before the combination of calibration measurements to the scene measurement. Thus, the detection procedure interacts with the moving average procedure. In the case where a fringe count error is detected, previous signals are shifted to the current signal. This way, all the following interferograms will have the same fringe count ordering. With its validity checks, this robust method is independent of the inherent signal decimation, and works for any pixel. As a baseline, the FCE detection is performed first for the central pixel in a given FOR, as each pixel will be affected by the same linear interferogram shift. If a problem is encountered, the detection is redone for another pixel to check if the problem is real and if the whole sweep should be discarded, or if the problem is local and only the pixel should be discarded. This multiple pixels approach with majority vote provides adds robustness against noisy single measurements, periodic bad interferograms, or failed detectors. The detection is done independently in each band, as FCE can occur in theory at different places in interferograms, affecting for example the LW, but not the SW and MW bands where acquisition stop is at smaller MPDs.

The global variable h_b^{cur} is the fringe count alignment reference for the calibration measurements. It is used to keep the alignment deficiency between the current instrumental FCE and the moving window elements. After the resetting of the moving window elements for a given calibration category, this variable is reset to zero. This correction scheme is devised in order to minimize the re-shifting of the moving average windows, which need to be aligned only during the moving average updates.

The FCE detection module analyzes the phase of raw spectra to establish if there was a fringe count error. It performs the low level computation of linear phase extraction from a complex input function $\widetilde{R}_b[n]$. A general description of the process is given in Section 3.3.3. The computational sequence of this function is illustrated by the flowchart of Figure 47. This algorithm is function of $\widetilde{R}(n)$ as well as the current laser metrology sampling wavelength λ_L.

In order to improve the accuracy of the linear fitting, data points with a too low SNR must be rejected. The present method selects points with a pre-defined amplitude threshold A^{thres} parameter, as indicated in Figure 47.

An optional refinement of the algorithm can be useful when dealing with signals having small SNR, helping to reject erroneous points and to pinpoint the exact FCE within noisy signals. This method identifies the valid data points by recursively computing the standard deviation of the points distribution $Q[p]$ around the computed linear fit, and by discarding those that differ by more than s_h^{thres} standard deviations. The following equations summarize this approach; but this operation is not part of the baseline.

$$\sigma_p = \sigma_{0_b} + p \cdot \Delta\sigma_b \tag{113}$$

$$Q[p] = \phi[p] - (\delta\phi \cdot \sigma_p + \phi_0) \tag{114}$$

$$s_h[p] = \mathrm{Stdev}\{Q[p]\} \tag{115}$$

$$p = \mathrm{Index}\left\{s_h[p] < s_h^{thres}\right\} \tag{116}$$

where s_h^{thres} is the standard deviation threshold rejection limit (typically 1 to 2), and $\mathrm{Stdev}\{\}$ computes the standard deviation, according to Equation (5).

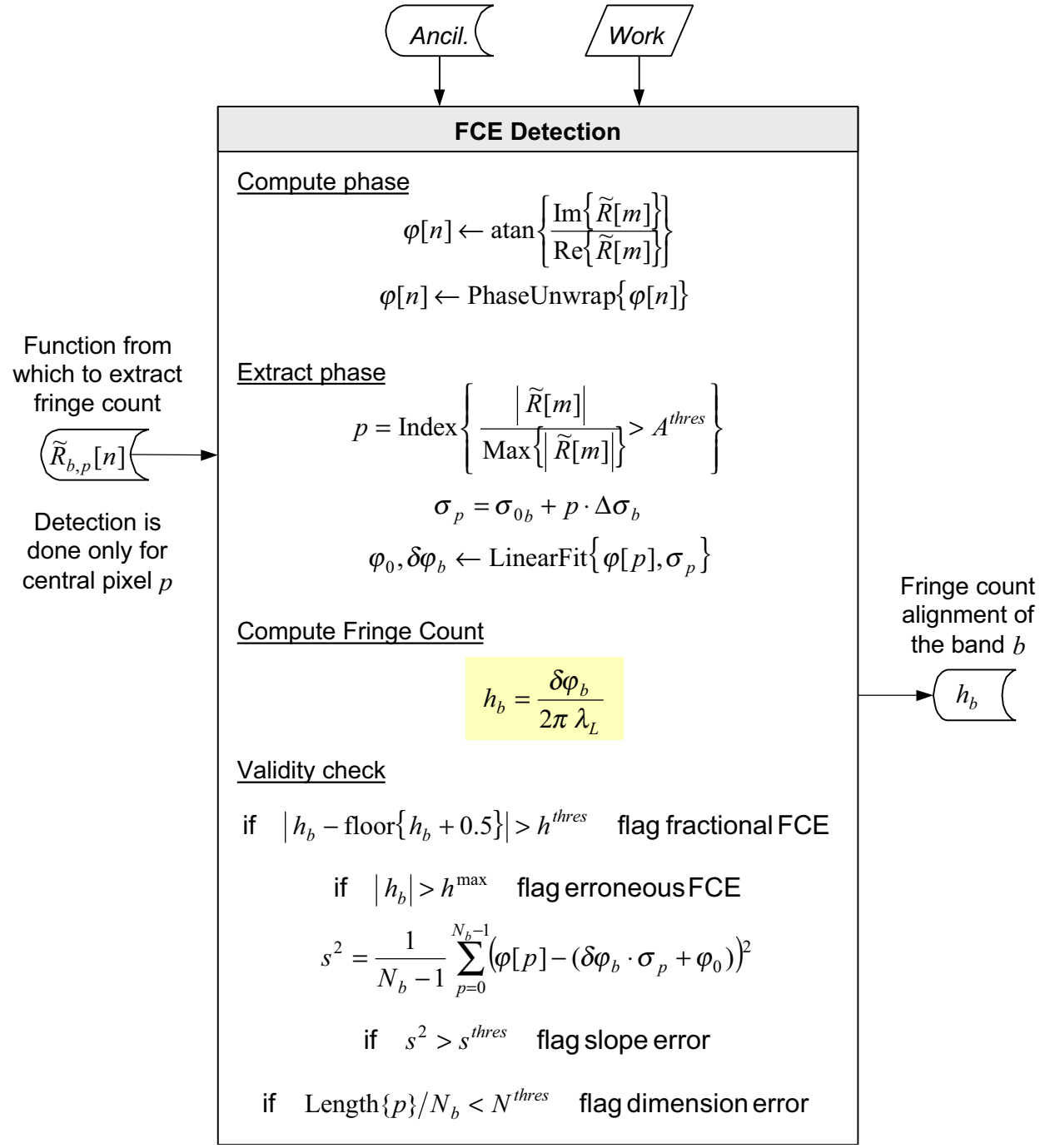

Figure 47: Fringe Count Computation Flowchart

7.4.1 Definition of variables

Input variables

$\widetilde{R}[n]$ phase extraction function from which linear phase dependency is computed. The exact form of $\widetilde{R}[n]$ is given in each following specific FCE modules.

Calibration data

None required for this function.

Ancillary data

A^{thres} amplitude threshold rejection limit (typically 0.1 or 0.2).

h^{thres} fractional FCE threshold limit (typically 0.1).

$h^{\max}$ maximum expected FCE (typically DF_b).

s^{thres} goodness of linear fitting threshold limit (typically 1.0).

N^{thres} Relative number of points to fit inferior limit (typically 0.5).

DF_b Decimation factor of the band b.

Work variables (from Compute Spectrum module)

λ_L calculated laser wavelength.

Local variables

$\varphi[n]$ linear phase function of $\widetilde{R}[n]$ [rad].

p index points where to compute slope.

φ_0 linear phase function ordinate at origin (not used as such).

$\delta\varphi$ linear phase function slope.

s^2 squared standard deviation goodness of fit indicator.

Output variables

h_b fringe count alignment of input signal.

Operators

$\mathrm{Index}\{\}$ gives index values of non-zero input argument

$\mathrm{PhaseUnwrap}\{\}$ removes phase jumps in signal in case it exceeds the range [–π,+π]. Compensations of $\pm 2\pi$ are added to the phase where discontinuities (absolute difference greater than π) are noticed between two consecutive points.

$\mathrm{LinearFit}\{y, x\}$ computes a linear fit on data points of array y, given together with its associated abscissa wavenumber values x (not uniformly distributed). See Appendix 9.3.

In the case of slope error, the signal is flagged appropriately for the subsequent functions in order to avoid processing invalid data. For example, this avoids corrupting moving average with a calibration signal in which a fringe count error happened in the middle of the measured interferogram. The ZPD_{pos} can be used for debugging and for the special case handling of to suspicious flagged errors. Other pixels than the central one can also be used for that purpose, or in the case where the central pixel is not available, but the exact procedure is still TBD and needs a further study with typical signals. A robust majority vote in the case of suspicious signal will be designed for that purpose.

7.4.2 Exception handling

This module allows the handling of the following exceptions:

Fractional FCE: computed h_b differs from an integer

Erroneous FCE: computed h_b is larger than expected values ($|h_b| > h^{\max}$)

Slope error indicating a non-linear phase residual ($R^2 > R^{thres}$)

Dimension error (can be caused by too much noise):

- Only a few points are higher than A^{thres}
- Only a few points are below s_h^{thres}

Incoherence detected with N^{ZPD} (TBD)

The module assigns these flags to the processed signal. For non-major detected errors, the processing continue and flags are transferred into calibrated spectra to identify in which of the constituents FCE were found (ICT, DS, ES, or combinations)

7.5 FRINGE COUNT ERROR CORRECTION

This module detects and corrects FCE in raw spectrum measurements. If the input is a calibration measurement, the ratio is taken between this spectrum and the corresponding current mean. In the case of an earth scene measurement, a slightly different, but equivalent, approach is taken.

In the case of a detected FCE mismatch, the current means are shifted back to the present measure which defines the current FCE alignment. If a slope error is flagged in a calibration measurement, indicating a mismatch of some sort, no corrective approach is taken. This is done in order to avoid contaminating the moving average with a single erroneous event.

A general description of the process is given in Section 3.3.4. The computational sequence of this function is illustrated by the flowchart of Figure 48. While detection is performed only for the central pixel, the correction is done on all pixels of the FOR of the current band. As said earlier, if a problem is encountered, detection is performed on other pixels in order to confirm or refute the glitch.

For each one of these modules, the input spectral function $\widetilde{R}[n]$ is defined as follows (see Section 3.3):

For *Calibration Measurements* (X = ICT or DS)

$$\widetilde{R}[n] = \frac{\widetilde{S}^{X}[n]}{\left\langle \widetilde{S}^{X} \right\rangle [n]} \tag{117}$$

For *Earth Scenes* (X = ES)

$$\widetilde{P}[n] = \frac{\widetilde{S}^{es}[n]}{\left\langle \widetilde{S}^{ict} \right\rangle [n] - \left\langle \widetilde{S}^{ds} \right\rangle [n]} \tag{118}$$

$$\widetilde{Q}[n] = \frac{\left\langle \widetilde{S}^{ds} \right\rangle [n]}{\left\langle \widetilde{S}^{ict} \right\rangle [n] - \left\langle \widetilde{S}^{ds} \right\rangle [n]} \tag{119}$$

$$\widetilde{R}[n] = \frac{\widetilde{P}[n]}{\sqrt{\left|\widetilde{P}[n]\right|^2 - \mathrm{Im}\left\{\widetilde{Q}[n]\right\}^2} + i\ \mathrm{Im}\left\{\widetilde{Q}[n]\right\}} \tag{120}$$

For this last computation, it is assumed that the calibration measurements are aligned on the same ZPD count. This wouldn't be the case in the very unlikely case where a fringe count error would occur between the very first two calibration measurements. Even if this would occur, the health monitoring module will detect the non-linear result and problematic calibrated scenes will be flagged accordingly.

After having performed the FCE detection, the global variable h_b^{cur} is updated to account for the new fringe count status of the instrument.

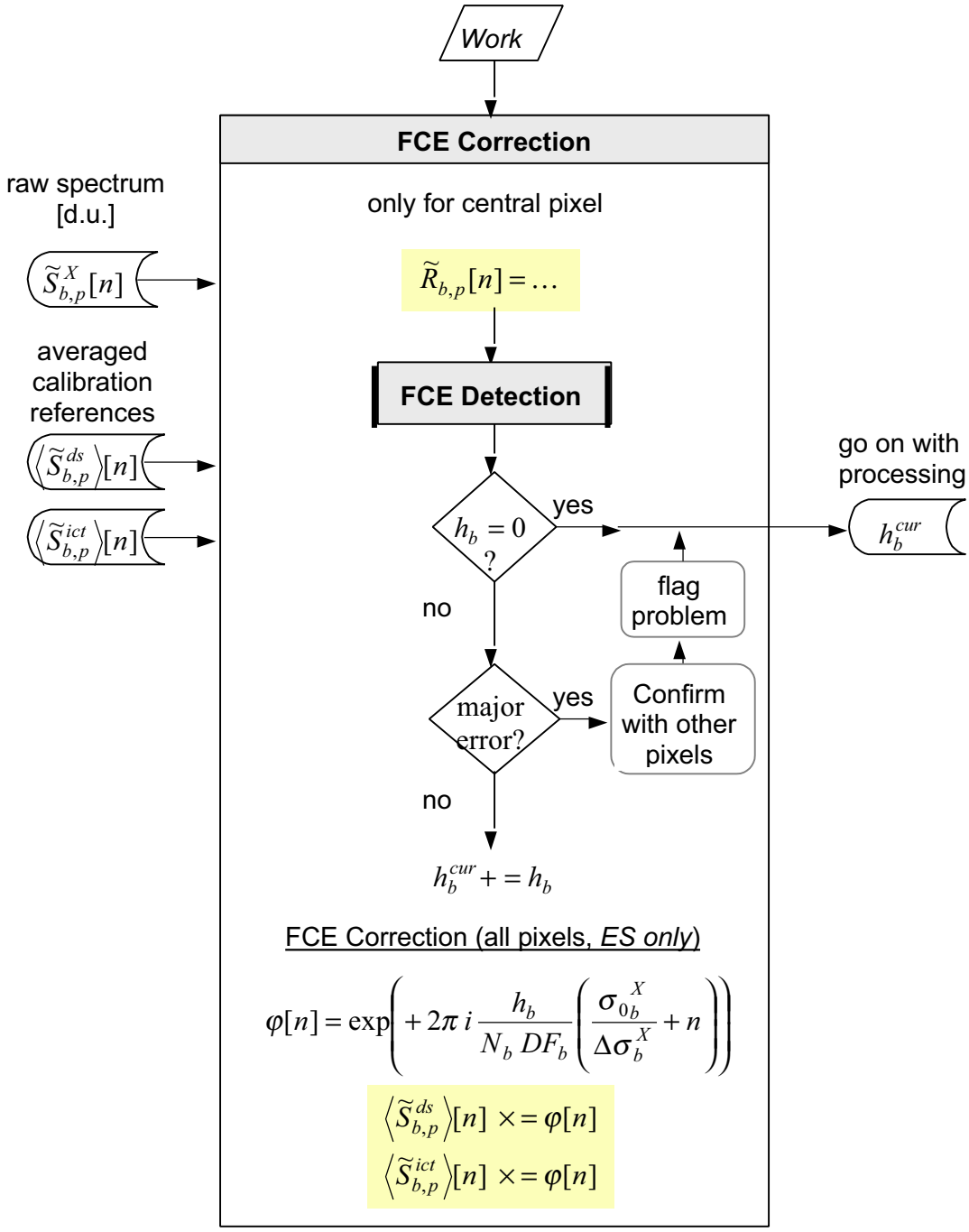

Figure 48: Fringe Count Error Correction Flowchart

7.5.1 Definition of variables

Input variables

$\widetilde{S}^{X}_{b,p,d}[n]$ raw complex spectrum, corresponding either to X = DS, ICT, or ES., expressed in [d.u.] at wavenumber σ_n.

Calibration data

None required for this function.

Ancillary data

None required for this function.

Work variable

h_b^{cur} current fringe count alignment reference (global nature).

$\left\langle \widetilde{S}^{ds}_{b,p,d} \right\rangle [n]$ raw complex spectrum of space look (DS) averaged over N^{ma} measurements, expressed in [d.u.] at wavenumber σ_n.

$\left\langle \widetilde{S}^{ict}_{b,p,d} \right\rangle [n]$ raw complex spectrum of internal calibration target (ICT) averaged over N^{ma} measurements, expressed in [d.u.] at wavenumber σ_n.

σ_{0b}^{X} signal wavenumber origin for band b [cm^{-1}]

$\Delta\sigma_b^{X}$ signal spectral interval [cm^{-1}]

Local variables

$\widetilde{P}, \widetilde{Q}$ phase extraction arrays, function of wavenumber.

$\widetilde{R}[n]$ phase extraction function

$\varphi[n]$ linear phase shift term.

h_b fringe count misalignment between previous and current input signal.

Output variable

No actual value is outputted by this function, but other work variables are modified (realigned to current FCE) when a mismatch is detected.

Operators

$\mathrm{FCE\ Detection}\{\ \}$ See Section 3.3.3

7.5.2 Exception handling

Slope error handling.

7.6 MOVING AVERAGE MODULE

This module handles the moving average of calibration raw scene measurements. The global shifting of the moving window is handled solely in this module, in order to avoid frequent or even unnecessary tables shifts that could slow down the computing process. Temperature computation and the moving average handling of these temperatures is also performed inside this module. A general description of the process is given in Section 5.5.1. The computational sequence of this function is illustrated by the flowchart of Figure 49.

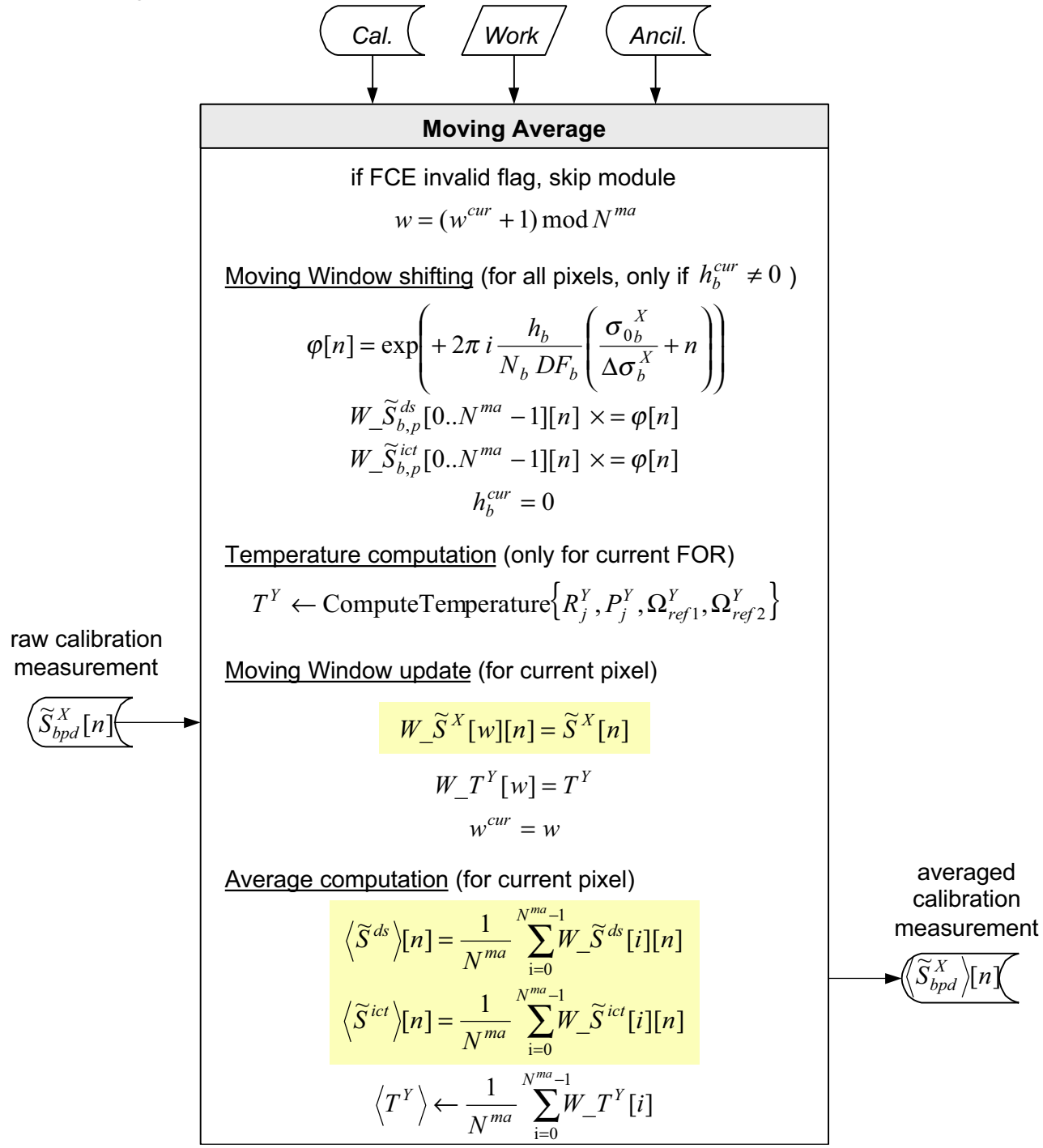

Figure 49: Moving Average Flowchart

Note: Operations on temperature variables (T^Y, W_T^Y) are performed only if incoming spectrum correspond to X = ICT. Y refers to each temperature monitored elements (Y = ict, BS, etc. as given in Table 13 of Section 5.2). This is computed for the whole scan, globally for the whole pixels.

Special processing occurs during the initial filling of moving window, where the average computation can be skipped.

7.6.1 Definition of variables

Input variables

$\widetilde{S}^X_{b,p,d}[n]$ raw calibration complex spectrum in [d.u.], corresponding either to X = DS or ICT

Calibration data

R^{ict}_j ICT PRT resistance temperature readings (3 values j = 0..2) given in raw instrument digital counts [d.u.]

R^{env}_j environment PRT resistance temperature readings (3 values j = 0..2) given in raw instrument digital counts [d.u.]

Ancillary data

N^{ma} moving average window size (baseline is 30)

P^{ict}_i polynomial coefficients used for ICT temperature computation.

P^{env}_i polynomial coefficients used for ICT temperature computation.

Ω^{ict}_{refN} two ICT precision resistance values [Ω]

Ω^{env}_{refN} two environment reading precision resistance values [Ω]

Work variables (global nature)

h^{cur}_b current fringe count alignment reference (global nature).

w^{cur} current position in moving average window.

$W\_\widetilde{S}^{ds}_{b,p,d}[i][n]$ moving window values ($i = 0..N^{ma}$) for DS spectrum calibration measurements.

$W\_\widetilde{S}^{ds}_{b,p,d}[i][n]$ moving window values ($i = 0..N^{ma}$) for ICT spectrum calibration measurements.

$W\_T^Y[i]$ moving window values ($i = 0..N^{ma}$) for monitored temperature readings.
Y corresponds to one of the temperatures given in Table 13 of Section 5.2.

σ^X_{0b} signal wavenumber origin for band b [cm^{-1}]

$\Delta\sigma^X_b$ signal spectral interval [cm^{-1}]

Local variables

w new index position in moving average window.

$\varphi[n]$ linear phase shift term.

T^Y computed monitored temperature [K]

Output variable

$\left\langle \widetilde{S}^{X}_{b,p,d} \right\rangle [n]$ raw complex spectrum of calibration measurements (DS and ICT) averaged over N^{ma} measurements, expressed in [d.u.] at wavenumber σ_n.

$\left\langle T^{Y} \right\rangle$ mean calculated monitored temperature in [K]

Operators

$\mathrm{ComputeTemperature}\{\}$ See Section 5.4.1.

7.6.2 Exception handling

If FCE Detection module identifies an abnormal FCE in a calibration measurement, which can be caused for example by an in-interferogram FCE, then this signal is invalid and must be discarded and not be inserted in moving average in order to avoid corrupting the moving average window.

Computed temperatures exceed expected values.

7.7 RADIOMETRIC CALIBRATION MODULE

The Radiometric Calibration module performs the processing of the scene measurements and generates radiometrically calibrated spectra. This module makes usage of current mean of calibration measurements (DS and ICT measurements). Polarization and scan mirror gain correction is performed at the same time. A general description of the process is given in Section 4.2. The computational sequence of this function is illustrated by the flowchart of Figure 50.

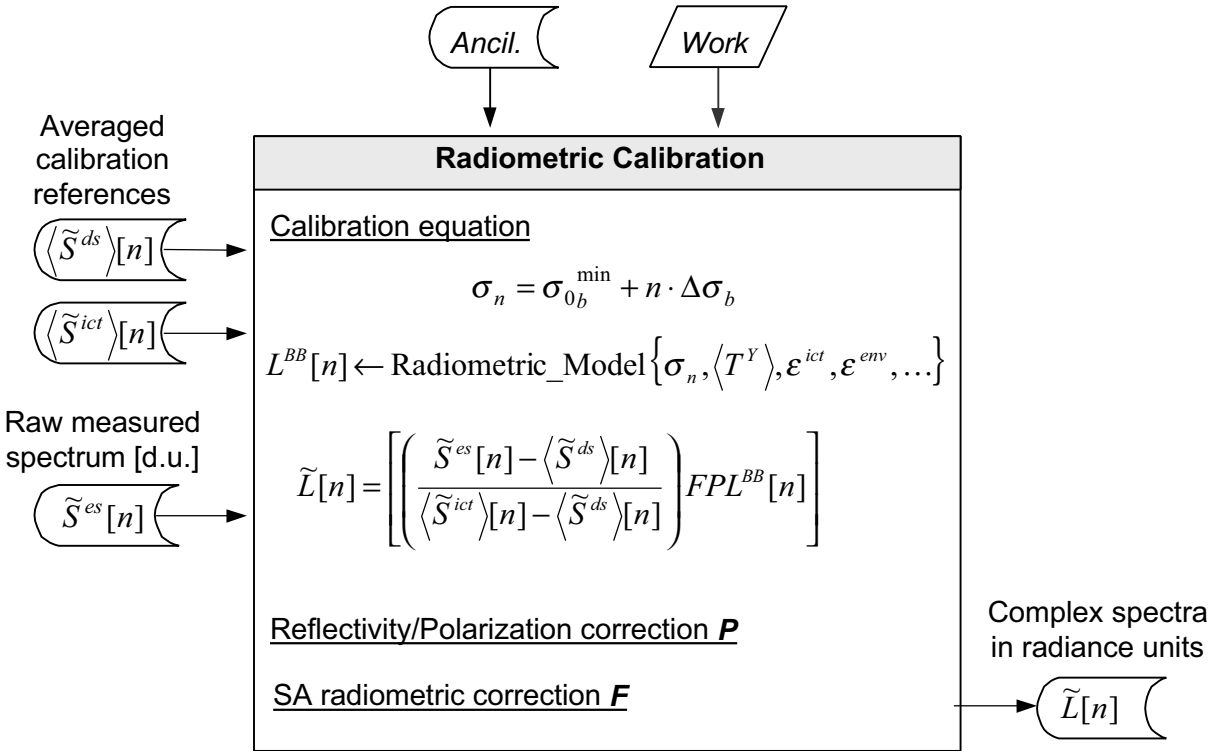

Figure 50: Radiometric Calibration Flowchart

Figure 50 illustrates the relationships between the calibration module's input parameters and specifically the computation performed. The radiometric calibration block performs its processing in the spectral domain rather than the interferogram domain. Radiometric calibration is essentially the computation of Equation (70), corresponding to a subtraction of the offset and a multiplication by the overall gain, as described in Section 5.3. The radiometric calibration is a point-by-point complex operation. All spectral arrays processed are complex, thus accounting for both magnitude and phase effects when performing this type of calibration.

7.7.1 Definition of variables

Input variables

$\left\langle \widetilde{S}^{ds}_{b,p,d} \right\rangle[n]$ raw complex spectrum of deep space (DS) averaged over N^{ma} measurements, expressed in [d.u.] at wavenumber σ_n.

$\left\langle \widetilde{S}^{ict}_{b,p,d} \right\rangle[n]$ raw complex spectrum of internal calibration target (ICT) averaged over N^{ma} measurements, expressed in [d.u.] at wavenumber σ_n.

$\widetilde{S}^{es}_{b,p,d}[n]$ raw complex earth scene (ES) atmospheric spectrum measurement, expressed in [d.u.] at wavenumber σ_n.

Calibration data

None required for this function.

Ancillary data (known from instrument characterization)

$\varepsilon^{Y}[n]$ spectral emissivity as a function of wavenumber (database).

$\tau^{Y}[n]$ self-emissivity of CrIS element.

$R_b^{45}[n]$ scan mirror reflectivity as a function of wavenumber (database).

$K_b^{\theta}[n]$ optional angle/polarization gain correction table (see discussion in Section 3.2). The range n corresponds to the requested spectral axis definition $n = 0 \ldots N^{req} - 1$

Work variables (from Moving Average module)

$\left\langle T^{Y} \right\rangle$ mean of calculated monitored temperatures in K.

Local variables

σ_n wavenumber scale corresponding to numerical arrays

$L^{BB}[n]$ calculated real ICT radiance at wavenumber σ_n.

Output variables

$\widetilde{L}[n]$ calibrated complex (real and imaginary parts) spectrum in radiance units [r.u.] at wavenumber σ_n.
→ transfer FCE flags from DS, ICT, ES to output.

Operators

F instrument operator describing the self-apodization effect and the residual term

P polarization and reflection operator describing the effect of polarization and reflection of the SSM

$\mathrm{Radiometric\_Model}\{\}$ computes radiance from model inputs (see Equation (74) in Section 4.2) for more details). Radiance calculation according to ICT theoretical model.

7.7.2 Exception handling

Incompatible sizes of signals: number of points does not match between DS, ICT, and ES. Should not happen, only internal checks.

7.8 HEALTH MONITORING MODULE

In the absence of error the resulting imaginary part of the calibrated spectrum should contain only white noise, meaning that no phase errors remain uncorrected by the calibration process. The CrIS data quality monitor uses the imaginary part of the recovered spectra as a measure of data quality for detecting possible errors. The computational sequence of this function is illustrated by the flowchart of Figure 51.

Quality control

Identifies slow phase dependence that may not have been removed by calibration (e.g. BS temperature drift) with a sinc smoothing function (see Section 9.6). A goodness of fit (see Section 9.5) then checks if the resulting low frequency DC signal contains structure or is only noise by a comparison with the null slope abscissa axis. If the correlation coefficient exceeds a given threshold, the calibrated signal is flagged as corrupted.

NESR evaluation

The health monitoring module also analyze the imaginary part of each calibrated spectrum to get a global Noise Equivalent Spectral Radiance (NESR). This global NESR is the standard deviation (see Equation (5)) of the calibrated signal on all wavenumber. This provides sensor noise estimate to EDR algorithms that need it to define covariance matrix and to fix the convergence limit iteration of the retrieval process. The low frequency DC dependence previously obtained is first removed from the imaginary part and the NESR is computed as the standard deviation on all bins. This NESR evaluation will need a pre-launch confirmation between measurements and model.

A similar analysis is performed bin-by-bin on the moving average elements of the raw DS and ICT spectra to assess the spectral structure of the noise in the case of a cold (C) and hot (H) references. This can be useful to determine the channel EMI. The obtained signals are uncalibrated, but the process for NESR evaluation is exact in the presence of true calibration sources, like the DS or ICT which are noise independent. This is not truly exact in the case of calibrated LW which is detector noise limited, nor for SW and MW which depend on level of signal. When sensor noise is proportional to signal, a ground characterization would be required, as a correction for signal amplitude versus noise. The scalar value of radiance noise can be used to scale these noise structures.

Imaginary part removal

In the case where no error was found, the imaginary part is finally removed and only the real part of the complex spectra is kept for the remaining modules. Removal of this imaginary part leads to a 1.41 factor noise improvement. A switch is available for archiving this imaginary part.

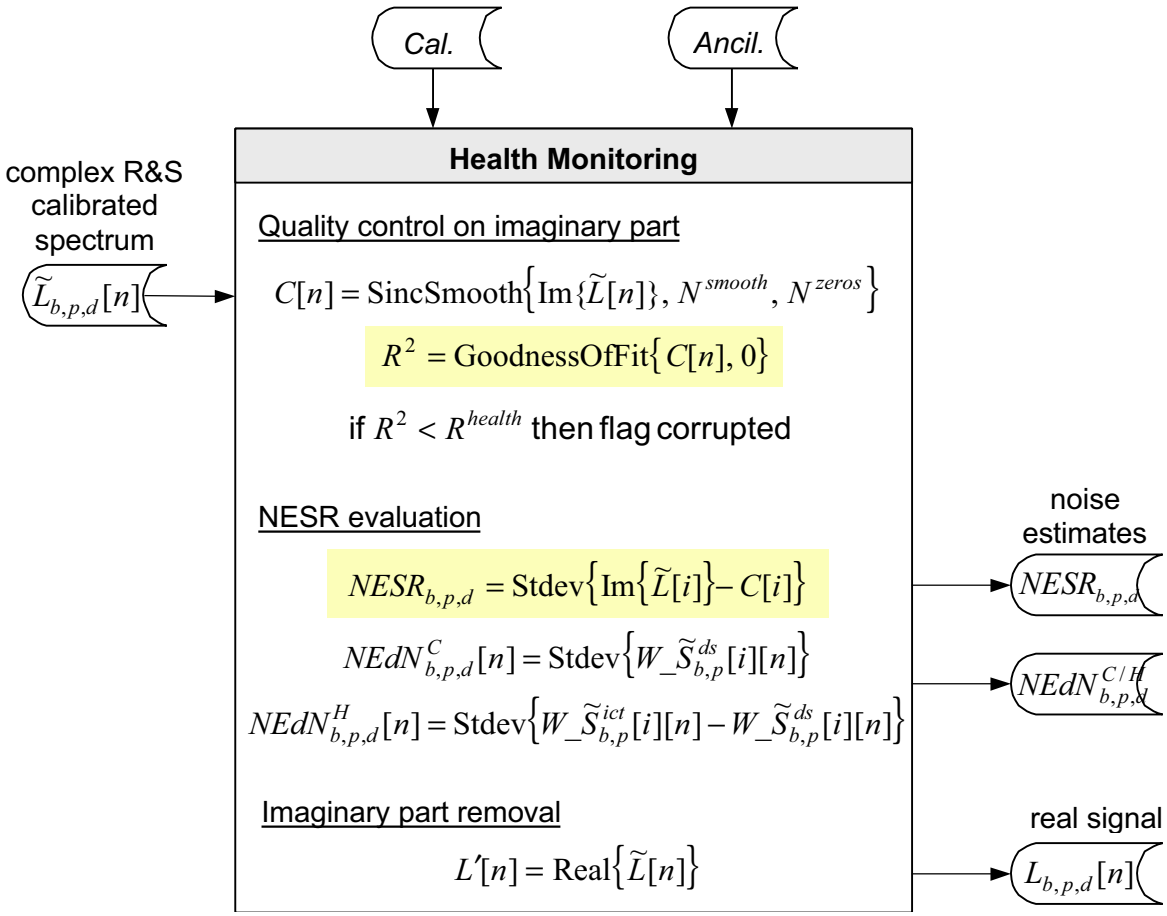

Figure 51: Health Monitoring Module Flowchart

7.8.1 Definition of variables

Input variables

$\tilde{L}_{b,p,d}[n]$ complex radiometrically and spectrally calibrated spectrum of earth scene.

Calibration data

None required for this function.

Ancillary data

N^s determines the amount of smoothing (typically 20).

N^z the number of zeroes used in the sinc smoothing function (typically 10).

N^{ma} moving average window size (baseline is 30)

Local variables

$C[n]$ low frequency inherent signal of the imaginary part

Work variables (global nature)

$W\_\widetilde{S}^{ds}_{b,p,d}[i][n]$ moving window values ($i = 0..N^{ma}$) for DS spectrum calibration measurements.

$W\_\widetilde{S}^{ds}_{b,p,d}[i][n]$ moving window values ($i = 0..N^{ma}$) for ICT spectrum calibration measurements.

Output variables

$L_{b,p,d}[n]$ real radiometrically and spectrally calibrated spectrum of earth scene.

$NESR_{b,p,d}$ scalar global radiance noise estimate.

$NEdN^{ds}_{b,p,d}[n]$ spectral noise structure computed from DS.

$NEdN^{ict}_{b,p,d}[n]$ spectral noise structure computed from ICT.

7.8.2 Exception handling

Non-zero mean detected in imaginary part.

7.9 SPECTRAL CORRECTION MODULE

This module performs the combination of three different operations combined into a single matrix multiplication. The first operation is a spectral interpolation to resample calibrated spectra over a pre-defined user's grid. The second operation is to remove the self-apodization of the instrument. Finally, the third operation is an optional signal apodization by a Hamming or Blackman function. A specific description of each of these processes is given respectively in Section 3.4, Section 3, and Section 3.5.4. The computational sequence of this function is illustrated by the flowchart of Figure 52.

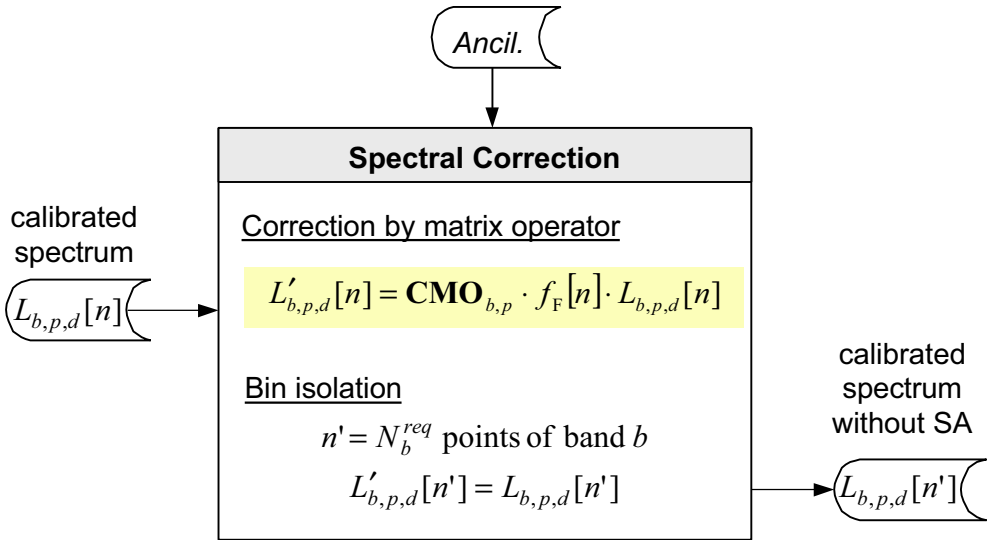

Figure 52: Spectral Correction Flowchart

7.9.1 Definition of variables

Input variables

$L_{b,p,d,i}[n]$ real radiometrically and spectrally calibrated spectrum of earth scene.

Calibration data

CMO correction matrix operator

N_b^{req} number of output bins for each band

f_F post calibration filter defined for each band

Ancillary data

None required for this function

Local variables

n' indices of bins within the user's grid

Output variables

$L_{b,p,d,i}[n]$ spectrally corrected spectrum

7.9.2 Auxiliary CMO computation

This subsection describes the computation of the **CMO** auxiliary correction matrix. The **ISA** and **H** intermediate matrices are computed during instrument characterization and stored on disk. The **F** matrix is computed at the beginning of the process, with the first available wavelength characterization, and the **CMO** matrix is then subsequently computed with or without the apodization matrix according user's request. It may have to be recomputed due to the required change of the **F** matrix in the special case where the sampling wavenumber changes more than a pre-defined threshold (see Section 7.3). Each computed **CMO** matrix has a specific ID for proper processing follow-up.

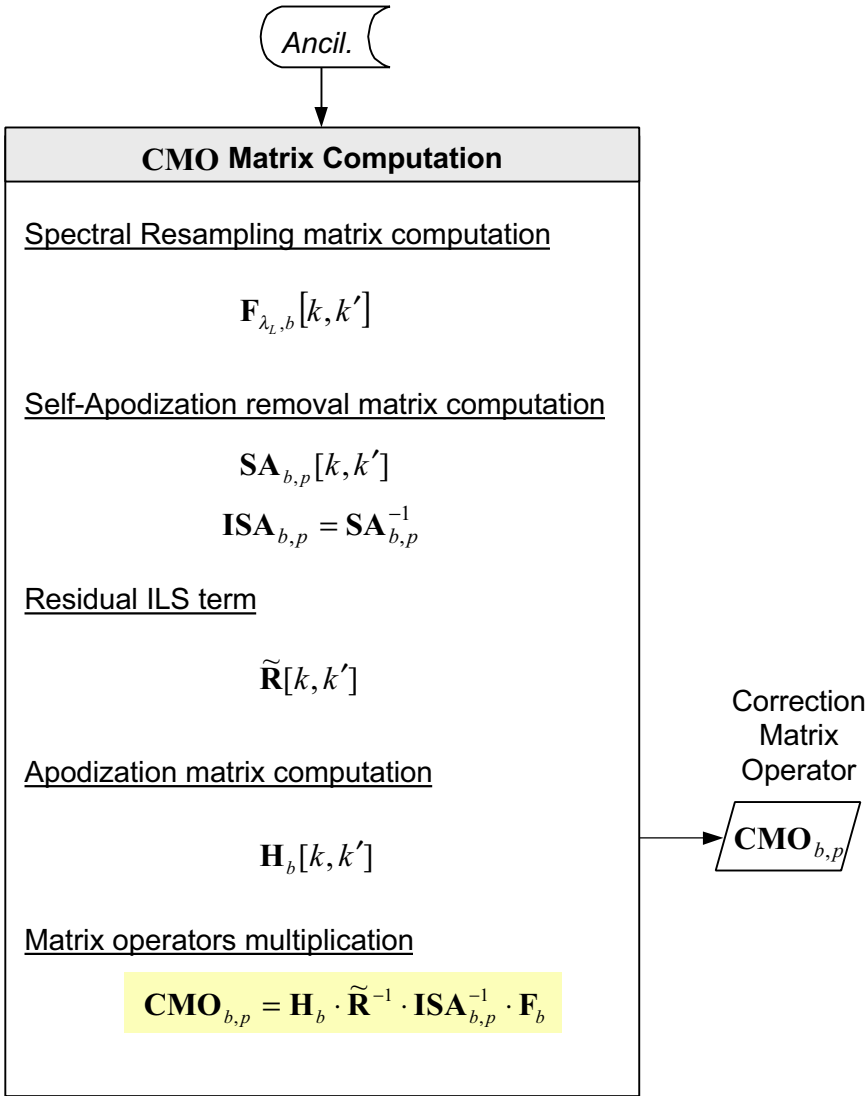

Figure 53: Self-Apodization Matrix Operator Computation Flowchart

Definition of variables

Input variables

None required for this function.

Calibration data

None required for this function.

Ancillary data

N_b^{req} number of output bins for each band.

λ_L computed wavelength of last spectral calibration.

λ_b effective wavelength of band b ($\lambda_b = 2MPD_b / N_b$).

Local variables

$F_b[k,k']$ spectral resampling/interpolator matrix operator.

$SA_{b,p}[k,k']$ self-apodization matrix operator.

$\tilde{R}[k,k']$ residual ILS matrix operator.

$ISA_{b,p}[k,k']$ self-apodization removal matrix operator.

$H_b[k,k']$ Hamming (or Blackman) apodization matrix operator (*with presence flag*).

Generated Auxiliary variable

CMO global Correction Matrix Operator.

7.9.3 Exception handling

None.

7.10 GEOMETRIC CALIBRATION MODULE

This module assigns a precise position on Earth to each ES spectrum. It also fix the correct time tag to each spectrum.

First, an interpolation is required to evaluate the S/C ephemeris at the time the interferogram was recorded. This allows the proper evaluation of the S/C position, velocity and attitude needed for geometric calibration as described in Chapter 6. The sequence of transformations and operations is given in Figure 55

The output data of this module are geolocation parameters to be associated to the spectrum recorded at a given time by a given pixel (detector).

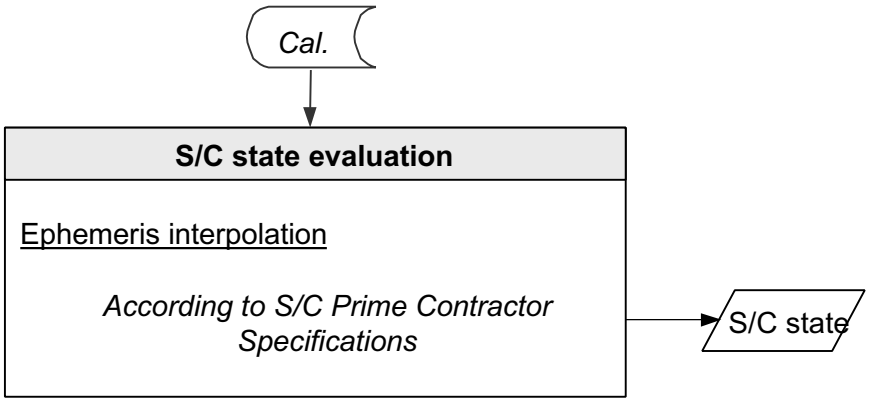

Figure 54: S/C State Interpolation Module Flowchart

Among the calibration data is the S/C State Record Time, the basis for ephemeris interpolation.

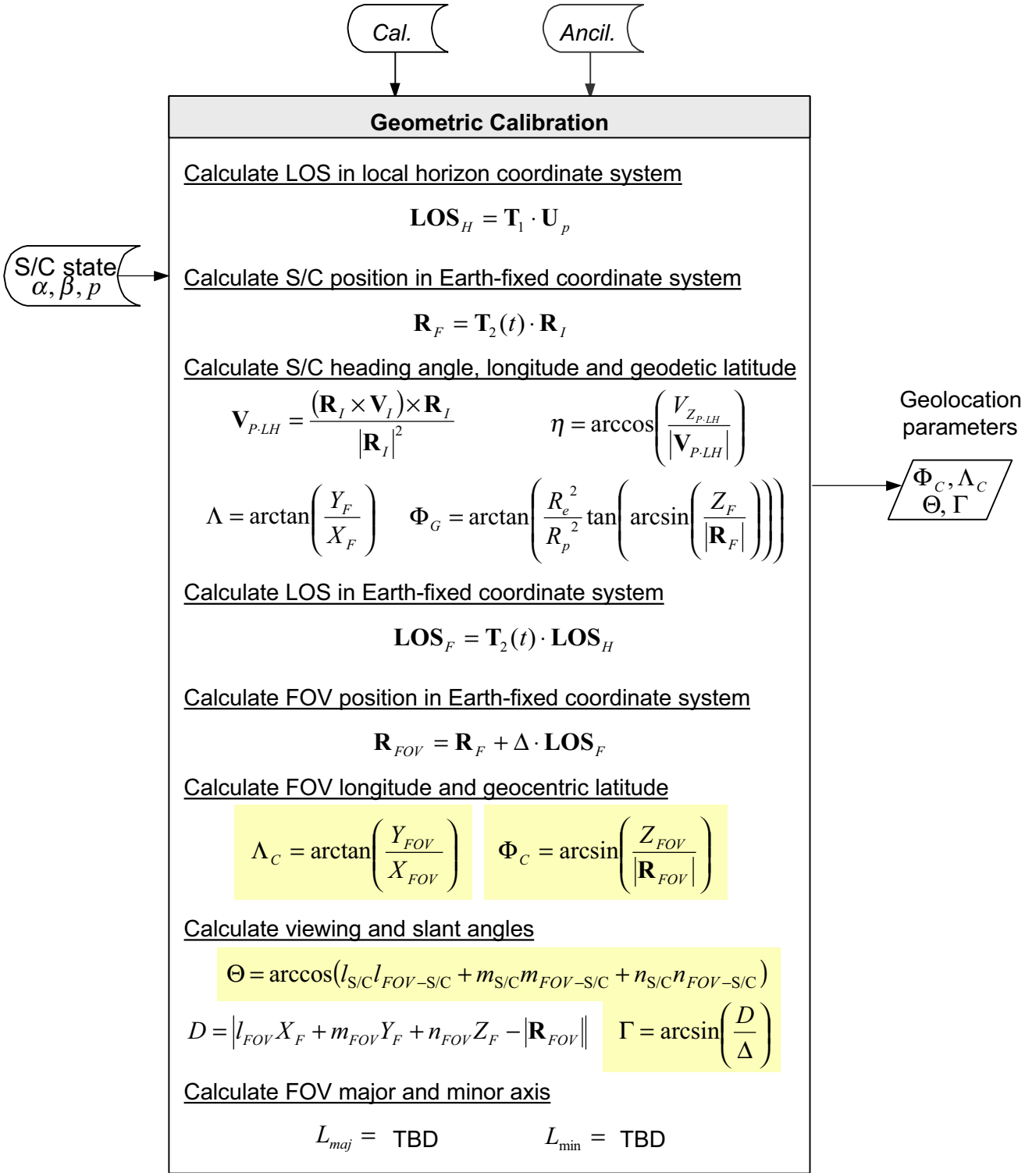

Figure 55: Geometric Calibration Module Flowchart

7.10.1 Definition of variables

Input variables

t_{rec}	time of interferogram recording
α	cross-track angle
β	elevation angle
p	pixel identifier

Calibration variables

E_t	ephemeris data table
$\mathbf{U}_p$	line of sight unit vector for pixel p
(ϕ,θ,ψ)	CrIS mounting offset Euler angles
υ	Earth rotation angular velocity
R_e	Earth equatorial radius
R_p	Earth polar radius

Local variables

$\mathbf{R}_I$	S/C position vector in geocentric-equatorial coordinate system
$\mathbf{V}_I$	S/C velocity vector in geocentric-equatorial coordinate system
$\mathbf{T}_1$	transformation matrix to local-horizon coordinate system
$\mathbf{LOS}_H$	line of sight unit vector for pixel p in local-horizon coordinate system
$\mathbf{R}_F$	S/C position vector in Earth-fixed coordinate system
$\mathbf{T}_2(t)$	transformation matrix to Earth-fixed coordinate system
η	S/C heading angle
Λ	S/C longitude
Φ_G	S/C geodetic latitude
$\mathbf{LOS}_F$	line of sight unit vector for pixel p in Earth-fixed coordinate system
Δ	distance from S/C to Earth surface (sea level)
$\mathbf{R}_{FOV}$	FOV position in Earth-fixed coordinate system
$l_{FOV}, m_{FOV}, n_{FOV}$	cosine director of FOV position vector
$l_{S/C}, m_{S/C}, n_{S/C}$	cosine director of S/C position vector
$l_{S/C\text{-}FOV}, m_{S/C\text{-}FOV}, n_{S/C\text{-}FOV}$	cosine director of S/C to FOV vector

Output variables

Λ_C	FOV geocentric longitude
Φ_C	FOV geocentric latitude
Θ	viewing angle
Γ	slant angle
L_{maj}	FOV major axis
$L_{\min}$	FOV minor axis

7.10.2 Exception handling

Time out of ephemeris interpolation range

Pointing angles out of range

Complex value for Δ (LOS not pointing toward Earth)

7.11 DATA QUALITY INDICATORS ROUND UP

SDR Algorithms compile data contamination error flags and various types of exception set by each data processing modules. Quality control is assured by the gathering of all various processing quality checks corresponding to each output data.

A report of Single Event Upset (SEU) is also given within the data quality indicators:

- Soft SEU or latchup detected (loss of interferogram)
- Hard SEU detected (loss of 16 seconds of data)

The possible error flags are listed below; consult sections referring to each module for further information about each error.

1. Impulse noise count detection:
   Detected/corrected spikes in current sweep
   How many?
   Index points
   Corrected?
   Failed bit trim
2. Compute Spectrum
   Computed laser wavelength exceeds expected limits
3. FCE handling
   Flags calibrated spectra: identifies in which of the constituents FCE were found (ICT, DS, ES, or combinations)
   How large shift?
   Fractional FCE.
   Erroneous FCE.
   Slope error.
   Dimension error (too many points discarded):
   Incoherence detected with N^{ZPD} (TBD)
4. Moving Average
   Not applied for given input signal
   Computed temperatures exceed expected values
5. Radiometric Calibration
   None.
6. Health monitoring
   Non-zero mean detected in imaginary part.
7. Spectral Correction
   What type of apodization was performed.
8. Geolocation
   TBD.

8. CONCLUSION

Summary of ATBD Document

The present Algorithm Theoretical Basis Document defines the Level 1B algorithms needed on ground in order to produce meaningful data meeting all the requirements of the CrIS instrument. This ATBD exposes the scientific basis, the mathematical description, and documentation of these algorithms required to generate as output geolocated, radiometrically and spectrally calibrated spectra in which instrument distortions are efficiently removed. Different algorithms are exposed and tradeoffs are given to substantiate the choice of the most appropriate algorithms for the task. The ATBD shows the functional partition and the internal data flow inside the SDR Algorithms, identifying data structures, and the transforms between them. The major features of the planned on-orbit and ground calibration processes are described and discussions are conducted over what is to be done in order to minimize output errors.

The SDR Algorithms successfully transform input RDR into SDR delivered as output, producing calibrated spectra meeting the specifications and requirements of the CrIS instrument. The algorithm performance is meeting all assigned top-level system performance and is compatible with the sensor's design.

Key algorithm characteristics

All essential concepts exposed in Section 2.1 have been covered in the remaining parts of the document. The effects of phase dispersion, fringe count errors, signal self-apodization, polarization, spectral shifts, are included.

The SDR Algorithms removes design particularities and attributes of the CrIS sensor, contained in RDRs, from the SDR user. SDR Algorithms convert data from real CrIS hardware into data that appears to originate from an ideal CrIS sensor. The SDRs are handed out with a pixel-invariant, sampling wavelength-invariant properties, and uniform (common) spectral grid outputs. The SDR Algorithms thus relieve EDR algorithms from any sensor specific perturbations.

The pixel-invariant property is done through off-axis self-apodization removal. All pixels at the SDR to EDR interface have the same characteristics: a standard geolocated grid, a standard wavenumber grid, a standard instrument line shape and wavenumber values. Stability of ILS is assured by the CrIS dynamical alignment. Proper ILS correction is a key element of the SDR algorithm, allowing a sensor with multiple FOVs to be used to process measured radiances by contrasting channels that have already undergone spectral correction. Without such correction, the implementation of the “Cloud Clearing” algorithm or any other pixel-to-pixel comparison at the EDR level may be compromized.

The SDR Algorithms rely on a set of data that is independent from any external instrument sources; all required inputs are taken from the CrIS sensor raw data records.

The SDR Algorithms are fault-tolerant: features have been incorporated into the algorithm and software designs to accommodate operational environment errors, including potential errors induced by anomalous conditions (impulse noise, FCE, sampling wavenumber drifts, etc.). The developed algorithms are strong and robust: they will work even in the presence of single unrecoverable error: for example, in the presence of a totally wasted calibration signal, this signal is discarded by the process in order to avoid corrupting the moving average, and the process then resumes its normal operations.

The current version of the SDR Algorithms represents the most up-to-date trade for the design. It has the modular flexibility of its inherent design in terms of its ability to accommodate requirement changes, performance enhancement, and technology insertions. An effort was made to create an

adaptable and flexible design that can withstand adjustments and refinements to meet unexpected future changes. The SDR Algorithms follow a simple structure, allowing similar processing for most of the measurements (DS, ICT, and ES).

Moreover, much of the present SDR Algorithms have heritage in other space programs, like the Engineering Model and Flight Model development and testing of MIPAS [RD 26], where Bomem has applied its expertise and developed solutions that helped the functional definition of practical interferometer calibration algorithms, like with the IASI program [RD 27] for example. The CrIS Engineering and Demonstration Model (EDM) [RD 7] is another example where Bomem has validated its models and algorithms, reaching a radiometric accuracy of better than 0.2%.

Scientific Code

The SDR Scientific Code (see description and results in [RD 28]) is a system prototype that successfully demonstrates the validity of all the SDR Algorithms in a working environment. Test and validation cases are presented in this document, giving confirmation that radiometric calibration is performed within the 0.1% requirement and spectral calibration within the 2 ppm for all the FOVs. The validity of the algorithms for geometric calibration is also demonstrated. The Scientific Code shows that the CrIS SDR Algorithms can meet the processing power requirements of 3.7 msec per field of view (includes all 3 bands) with reasonable resources on typical machines available by launch time (extrapolated from a Pentium II 400 MHz).

Final Word

Many major issues have been resolved by Preliminary Design Review (PDR). Few pitfalls have been caught and resolved by Detailed Design Review (DDR). Moreover, during DDR phase, more accurate ILS correction scheme and ICT radiometric model have been developed, and impact of central obscuration within the instrument has been preliminary assessed. The present SDR Algorithm ATBD provides comprehensive written documentation, giving description, explanations, and justifications for the various algorithms. We believe that the present version of the SDR Algorithms fully meet the CrIS accuracy requirements and will also meet the processing time constraints. Minor issues remain regarding the geolocation (SDR algorithm scope about this is not yet decided).

Few studies remain to be done after DDR, in order to further validate the calibration and correction approaches. For example, the behavior of the SDR Algorithms will be studied with typical measurements from a prototype interferometer or with the CrIS Engineering Development Unit (EDU) in order to further fine-tune or adapt the system to real conditions.

Pre-launch calibration uses a combination of optical inputs to the CrIS sensor and generated scene data to test and calibrate the SDR Algorithms. Post-launch calibration will use CrIS data and calibration sources combined with ground truth. A separate document will present a comprehensive plan for all these calibration procedures (characterizations), as well as test and validation processes.

9. APPENDICES

9.1 FAST FOURIER TRANSFORMS

Data acquisition yialds the digitized interferogram $I(x)$, which must be converted into a spectrum by means of a mathematical operator called Fourier transformation (FT). Generally, the FT determines the frequency components making up a continuous waveform. However, if the waveform (the interferogram) is sampled and consists of N discrete, equidistant points, one has to use the discrete version of the FT, i.e. the discrete FT (DFT). The used conventions for the discrete direct and inverse numerical Fourier transforms are, as expressed in the interferogram and the spectrum domains:

$$S[n] = \Delta x \sum_{m=0}^{N-1} I[m]\, e^{-2\pi i\, m\, n/N} \tag{121}$$

$$I[m] = \Delta \sigma \sum_{n=0}^{N-1} S[n]\, e^{+2\pi i\, m\, n/N} \tag{122}$$

The equivalent function calls for the Fast Fourier Transform implementation are given by:

$$S_{b,p,d}[n] = \mathrm{FFT}\left\{I_{b,p,d}[m]\right\} \tag{123}$$

$$I_{b,p,d}[m] = \mathrm{I\,FFT}\left\{S_{b,p,d}[n]\right\} \tag{124}$$

with the following notation:

N is the total number of points in numerical arrays

n the interferogram index data points: $0,\ldots,N-1$

m the spectral index data points: $0,\ldots,N-1$

and Δx the sampling of the interferogram: $\Delta x = \dfrac{2\,MPD}{N} = \lambda_L = \dfrac{1}{\sigma_s}$ [cm] (125)

and $\Delta\sigma$ the sampling of the spectrum: $\Delta\sigma = \dfrac{1}{2\,MPD} = \dfrac{\sigma_s}{N}$ [cm^{-1}] (126)

The relation coupling the two spaces is: $\Delta x \Delta\sigma = \dfrac{1}{N}$ (127)

Results are expressed in term of unit of amplitude per sampling interval (Δx or $\Delta\sigma$), i.e., when integrating, the amplitude value must be multiplied by this sampling.

9.1.1 Comments on various algorithms

The Fast Fourier Transform algorithm is perhaps the one algorithmic discovery that has had the greatest practical impact in history. Fourier transforms are of fundamental importance is such disparate applications as optics, acoustics, quantum physics, telecommunications, system theory, and signal processing including speech recognition. For years, progress in these areas was limited by the fact that the known algorithms for calculating Fourier transforms all took far too long.

The discovery by Cooley and Tukey in 1965 of a fast algorithm revolutionized the situation: problems previously considered infeasible could now at last be tackled. In one early test for the “new” algorithm, the Fourier transform was used to analyze data from an earthquake that had taken place in Alaska in 1964. While the classic algorithm took more than 26 minutes of computation, the “new” algorithm was able to performs the same task in less than two and half seconds. Ironically it turned out that an efficient algorithm had already been published in 1942 by Danielson and Lanczos, and all the necessary theoretical groundwork for Danielson and Lanczos's algorithm had been published by Runge and Konig in 1924. And if that were not sufficient, Gauss describes a similar algorithm in a paper written around 1805 and published posthumously in 1866!

The “Fast Fourier Transform” (FFT) is an algorithm exist implementing the Fourier transform in a very efficient manner, with a much less complexity than a direct implementation as the one expressed in Equation (121).

There are different algorithms for performing numerical Fourier transforms. There are prime-factor algorithms, which only works on sizes that are products of relatively prime factors. There is also the Winograd algorithm. There is Bruun's algorithm (and related methods). And, there are various methods to change an FFT into a convolution, which can then be performed using one of a variety of fast convolution algorithms. Also, you can express the FFT in terms of fast Hartley transforms. That's all the major methods, but there are probably a few other obscure (and thoroughly impractical) algorithms.

These methods, however, tend to be either difficult to implement (and thus slow in practice) or limited to a small set of sizes. It is not clear if they offer any general advantage in practice. However, each of them tends to be useful in particular cases.

The choice of the right (fastest) FFT for a given application is a good question. No single implementation FFT can claim to be the “best" or the "fastest". A given implementation can behave differently on various machines and environments. It depends on many factors, among which a few are listed below:

- type of processor available (architecture, registers, etc.)
- size of memory available (main memory and cache memory)
- can the number of points be rounded to a power of two?
- size of transforms to be computed (up to 1024 points, or 1 M points?)
- use or not of intermediate temporary vectors
- use or not pre-computed trigonometric tables
- acceptable complexity of implementation
- type of complex data representation
- etc.

For example, some assembler Radix 4 routines outperform Radix 8 routines, while other optimized compiled in C language are faster on other machines with larger number of registers and local cache. The complexity of a given FFT routine is also an important factor to consider: some very fast routines are so complicated that their implementation in a DSP for example would be out of the question, while other almost as fast routines are much more simpler and can be coded in a small number of lines.

Some implementations use the complex data structure, while others use double precision data type to store complex numbers. This is not really a problem as data storage structure can always be interchanged by modifying the source code.

For some applications, the precomputation of trigonometric tables has no effect on the overall performance, while in other applications this could be detrimental. Double precision computation is preferable for adequate numerical accuracy. This is especially true if a trigonometric recurrence algorithm is chosen, where the last points may be totally corrupted due to “rounding effect” in single precision. On modern computers, double precision algorithms require almost the same computing time as the single precision algorithms, so there should be no penalty using maximum precision.

In summary, one has to check various FFT routines and his practical requirements to choose the right tool for the job. The choice of the FFT algorithm is an important issue for SDR Algorithms accuracy. From an accuracy point of view, no specific FFT algorithm is imposed and different algorithms are possible that use different optimization techniques. Care must be taken when considering the exponent sign ($\pm$) and the normalization constant ($1/N$ or $1/\sqrt{N}$ employed in the direct or inverse transform particular implementation. Consult [RD 18] for a thorough study and various implementations of discrete FFTs.

9.1.2 Data translation and centering

Signal swapping is required for bit reverse vectors data storage, where zero frequency is at the middle point of the signal. An alternative way to avoid this operation is to introduce a linear phase shift into the input data to change the position of the transform. In one dimension, we have the following translation relationship:

$$\mathrm{F}\left\{ f(x)\, e^{\pm 2\pi i x \sigma_0 / N} \right\} = F(\sigma \mp \sigma_0) \tag{128}$$

If we want to center the FFT result in the data array, we let $\sigma_0 = N/2$ in the previous equation:

$$\mathrm{F}\left\{ f(x_i)\,(-1)^i \right\} = F(\sigma - N/2) \tag{129}$$

This shows that to store the data with the origin at the center of the array, it is necessary the multiply the array by a phase factor of $(-1)^i$ to end up with a centered function after the transform is taken. For phase shifted, centered data, we have:

$$S(\sigma_i - N/2)\cdot(-1)^i = \mathrm{F}\left\{ I(x_i - N/2)\cdot(-1)^i \right\} \tag{130}$$

Therefore to obtain the correct result, the transform must also be multiplied by a $(-1)^i$ phase factor. For more information, consult [RD 11].

9.1.3 Prime Factor Algorithm Fast Fourier Transform

The Prime Factor Algorithm Fast Fourier Transform is a very effective self-sorting in-place complex FFT. It uses the Prime Factor Algorithm as described by Temperton [RD 5 and RD 6]. The implementation given by Dave Hale at the Center for Wave Phenomena at the Colorado School of Mines [RD 18] can rival most of all other existing algorithms when limited to a given set of dimensions (239 different values).

Other algorithms exist for array dimensions factor of any small prime numbers. Among these there are variants of the Cooley-Tukey algorithm (1965), as the one developed by P. Swarztrauber at the National Center for Atmospheric Research (FFTPACK), or the based on the subroutine FOURG by N. M. Brenner (1969) IBM Contributed Program Library, taken from the NAASA public library, Leonard J. Harding, April 1976 University of Michigan Computer Control, Ann Arbor. There is also machine-optimized versions by FFTW which can be competitive.

The execution times given in Table 7 correspond to three among the fastest FFT routines available, coded in C with CodeWarrior Pro 3 and optimized executables on a Pentium II at 350 MHz. The first is the PFA FFT, as implemented by the Center for Wave Phenomena at the Colorado School of Mines, and a FFT by Ooura. The two others are described below, while the fourth is the one available in Matlab 5. The execution times shall only be considered relative with respect to one another. These times are representative of the complexity of the algorithms, and can be viewed as estimates of the number of floating point operations required. Timings are given for the dimensions closest to the expected dimensions given in the present CrIS instrument specifications.

1: **Prime Factor Algorithm (PFA) in-place FFT**

The fastest of the fastest.
+ extremely fast for selected values of N
– only works for a few limited values of N (see conditions), N must be factorable into mutually prime factors taken from the set $\{2, 3, 4, 5, 7, 8, 9, 11, 13, 16\}$. In other words,

$$n = 2^p \cdot 3^q \cdot 5^r \cdot 7^s \cdot 11^t \cdot 13^u \text{ where } 0 \le p \le 4,\ 0 \le q \le 2,\ 0 \le r,s,t,u \le 1$$

2: **Mixed-Radix** (2-3-4-5-n) based on a variant of the Cooley-Tukey algorithm.

Developped by P. Swarztrauber at the National Center for Atmospheric Research (FFTPACK). Code inspired from IMSL library.
Good for N not powers of 2.
+ Optimized for small prime factors 2, 3, 4, 5.
(faster than Brenner when only these factors are present)
+ reasonably fast when not powers of 2.
– medium size implementation (880 lines of code).

3: **Modified Cooley-Tukey FFT**

Based on code by N. M. Brenner, adapted by Leonard J. Harding, NAASA library.
Good for N not power of 2.
+ faster than IMSL when N composed of large prime factors.
+ very small size implementation (190 lines of code).

9.2 ALIAS UNFOLDING

After the operation of decimation on an interferogram, the spectral range of the corresponding spectrum changes and must be precisely determined. To assign correct spectral axis one must perform *alias unfolding* (also called spectrum unscrambling or spectrum re-ordering) in order to remove the down conversion to a zero IF (intermediate Frequency) introduced at the satellite level

Let us suppose an original spectrum of N points with frequencies ranging from 0 to σ_s, where σ_s is the sampling frequency of the reference laser. We decimate the IGM using a decimation frequency DF_b (b for channel/band index), and keeping only N_b points. Then, the apparent frequencies range from 0 to σ_S/DF_b. The spectral range determination implies the reordering of the spectrum and a shift to the original band.

The reordering point k is determined with the following:

Defining

$$\Delta\sigma_{\text{dec}\,b} = \frac{1}{N_b\,\lambda_L DF_b} \tag{131}$$

the alias width is given by

$$W_b = N_b \Delta\sigma_{\text{dec}b} = \frac{1}{\lambda_L DF_b} \tag{132}$$

We want to position one alias window right over the spectral range of the numerical filter. Finding the integer number of $\Delta\sigma_{\text{dec}\,b}$ closest to the center of the numerical filter range determines the position of the lower limit of this alias window which is

$$\sigma_{\min b} = k\ \Delta\sigma_{\text{dec}\,b} \tag{133}$$

with

$$k = \text{Floor}\left\{\frac{\left(\sigma^{req}_{\min b} + \sigma^{req}_{\max b}\right) - W_b}{2\Delta\sigma_{\text{dec}\,b}}\right\} \tag{134}$$

where $\sigma^{req}_{\min b}$ and $\sigma^{req}_{\max b}$ correspond to the numerical filter limits.

Equation 134 provides the pivot which reorders the spectrum to cover the band of interest. One just has to rotate the spectrum k points to the left:

$$S[n] = \text{Rotate}\{S[n],\ k \bmod N_b\} \tag{135}$$

An example of the effect aliasing of decimation after complex numerical filtering is provided in Figure 56.

The numerical operation of unscrambling must be executed after each Fourier transform on decimated signals.

Decimation and alias unfolding
(data compression scheme)

As seen in the spectrum domain $S(\sigma)$

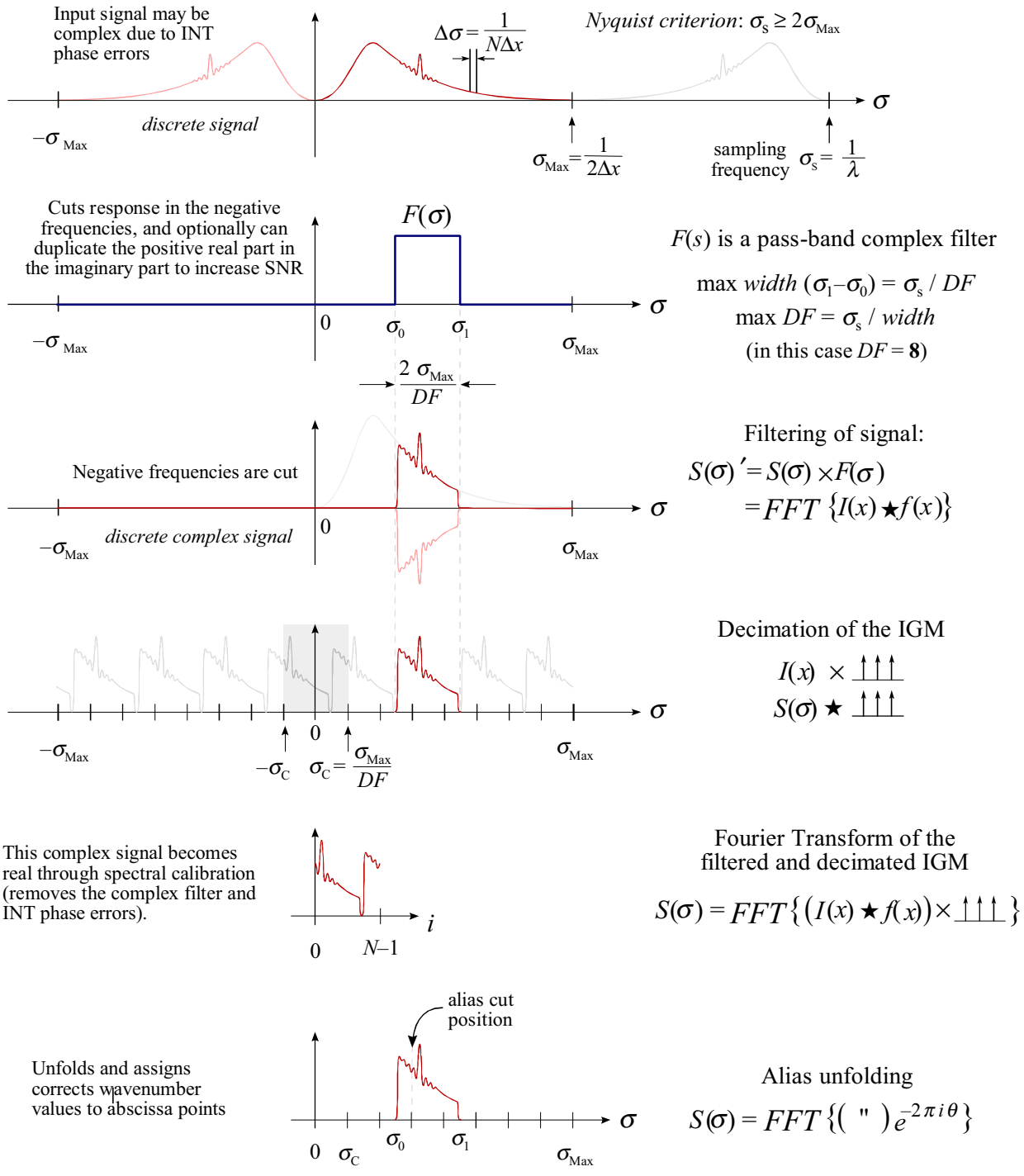

Figure 56: Interferogram decimation and alias unfolding

9.3 LINEAR FITTING

Description:

This subfunction is used for the determination of the slope and the ordinate of a straight line through a set of data points. It is used for the determination of the slope for the fringe count error detection.

We give here a general description for the implementation of the algorithm, that is independent of the type of data used as input.

Processing:

Variable	Descriptive Name	I/O	Type	Ranges / References / Remarks
N	Dimension of vectors to fit	i	i	No restriction on the size of N
x_i	Abscissa data values	i	r	could also be specified by: $x_i = x_0 + i\Delta x = \Delta x(-N/2 + i)$
y_j	Ordinate data values	i	r	
m	Computed slope of the fitted line	o	r	
b	Computed ordinate at origin of the fitted line	o	r	

One of the simplest implementation of the linear fitting is defined as follows:

$$y = mx + b \tag{136}$$

$$t = N \times \sum_{i=0}^{N-1} x_i^2 - \left(\sum_{i=0}^{N-1} x_i \right)^2 \tag{137}$$

$$m = \frac{1}{t}\left[N \times \sum_{i=0}^{N-1} x_i y_i - \sum_{i=0}^{N-1} x_i \times \sum_{i=0}^{N-1} y_i \right] \tag{138}$$

$$b = \frac{1}{t}\left[\sum_{i=0}^{N-1} y_i \times \sum_{i=0}^{N-1} x_i^2 - \sum_{i=0}^{N-1} x_i \times \sum_{i=0}^{N-1} x_i y_i \right] \tag{139}$$

When the abscissa data is uniformly distributed at Δx intervals, the previous expression can be further simplified:

$$y = mx + b$$

$$\begin{aligned} x &= x_0,\ x_0 + \Delta x,\ x_0 + 2\Delta x,\ \ldots,\ x_0 + (N-1)\Delta x \\ &= x_0 + [0, 1, 2, \ldots (N-1)]\ \Delta x \end{aligned} \tag{140}$$

$$t_1 = \frac{6}{\Delta x N(N+1)}, \tag{141}$$

$$t_2 = t_1 \sum_{i=0}^{N-1} y_i , \tag{142}$$

$$t_3 = \frac{2t_1}{N-1} \sum_{i=0}^{N-1} i y_i \tag{143}$$

$$m = t_3 - t_2 , \tag{144}$$

$$b = t_2 \left(x_0 + \Delta x \frac{2N-1}{3} \right) - t_3 \left(x_0 + \Delta x \frac{N-1}{2} \right) \tag{145}$$

9.3.1 Implementation of the linear interpolation

The following function call defined throughout the present document:

$$m, b = \text{LinearInterpolate}\left\{ S[n];\ \Delta\sigma, \sigma^{\min}, N,\ \sigma_{fit}^{\min}, \sigma_{fit}^{\max} \right\} \tag{146}$$

OR

$$m / \Delta\sigma, b = \text{LinearInterpolate}\left\{ S[n];\ N, n_0, n_1 \right\} \tag{147}$$

where $S[n]$ is the input function defined on N points, with numerical spectral axis values starting from $\sigma^{\min}$ and separated by $\Delta\sigma$. The $\sigma_{fit}^{\min}$ and $\sigma_{fit}^{\min}$ values define the spectral range limits in which the fit has to be computed.

Numerical interpolation shall be implemented as given in the previous section describing linear fitting when abscissa data is uniformly distributed.

9.4 NUMERICAL INTEGRATION

When we talk about numerical integration (which is also called “quadrature”) we immediately think about “Simpson’s rule” or “Trapezoidal rule”. The classical formulas for integrating a function whose values are known at equally spaced steps have a certain elegance about them, and they are redolent with historical association. But computing methods evolve and times change; with the exception of two of the most modest formulas (“extended trapezoidal rule” and “extended midpoint rule”, see [RD 19]), the classical formulas are almost entirely useless. They are museum pieces, but beautiful ones.

Integration with Gaussian Quadratures

Gaussian quadratures are among the most beautiful and the most powerful methods for numerical integration [RD 20]. The theory behind these methods goes back to Karl F. Gauss (1777–1885), who used in 1814 continued fractions to develop the subject. In 1826, Karl G. Jacobi (1804–1851) rederived Gauss's results by means of orthogonal polynomials. The systematic treatment of arbitrary weight functions $W(x)$ using orthogonal polynomials is largely due to Elwin B. Christoffel (1829–1900) in 1877.

The basic idea of Gaussian quadratures is to give ourselves one more degree of freedom with respect to traditional methods by an enlightened choice of the location of the abscissa points at which the function is to be evaluated: these points will no longer be equally spaced.

Instead of studying the habitual class of integrals of simple polynomial functions, we now study the class of integrands “polynomial times some known function $W(x)$”. The function $W(x)$ can then be chosen to remove integrable singularities from the desired integral. Given $W(x)$, in other words, and given an integer N, we can find a set of weights w_i and abscissas x_i such that the following approximation becomes exact if $f(x)$ is a polynomial:

$$\int_a^b W(x) f(x)\, dx \;\approx\; \sum_{i=0}^{N-1} w_i f(x_i) \qquad (148)$$

The fundamental theorem behind N-points Gaussian quadratures comes from the fact that the abscissas of Equation (148) together with the weighting function $W(x)$ in the interval (a, b) are precisely the roots of an orthogonal polynomial $p_N(x)$ for the same interval and weighting function. Without going into more mathematical details, lets mention that many known quadratures exist for different forms of the $W(x)$ function. The most general case where $W(x) = 1$ and with $-1 < x < 1$, implying Legendre polynomials P_N: these specific integrals are called *Gauss-Legendre quadratures*. This category is well suited for boundary conditioned physical problems like wave guides or resonators.

$$W(x) = 1 \quad \text{and} \quad -1 < x < 1$$

$$w_i = \frac{2}{(1 - x_i^2)\left[P_N'(x_i)\right]^2}$$

Legendre polynomial recurrence relation:

$$(n+1)\, P_{n+1} = (2n+1)\, x\, P_n - n\, P_{n-1}$$

9.5 DETERMINATION OF THE GOODNESS OF FIT

After a given fit has been computed, the standard deviation can be computed to evaluate the dispersion of the fit. The standard deviation is the root mean square of the deviations, and is associated with the *second moment* of the data about the mean [RD 21].

A goodness of fit indicator can also be computed between the reference points and the fit to determine with which validity they are similar. A useful operator used to evaluate the goodness of fit criteria is mathematically derived as follows:

$$r = \frac{\sum_{i=0}^{N-1}(f_i - \bar{f})(y_i - \bar{y})}{\sqrt{\sum_{i=0}^{N-1}(f_i - \bar{f})^2}\sqrt{\sum_{i=0}^{N-1}(y_i - \bar{y})^2}} \quad [-1\ldots1] \tag{149}$$

where f_i is the fitted data, or the experimental spectrum

y_i is the model data, or the reference spectrum

and $\bar{f}$ and $\bar{y}$ are the means of the vectors f and y.

Correlation coefficient *r*

r is the *linear-correlation coefficient,* also called the *product-moment correlation coefficient*, or *Pearson's* r. It indicates the strength of the association between the dependent and independent variables. The magnitude of the coefficient is not easy to interpret (see definition of coefficient of determination), but the sign (+ or –) indicates the direction of the relationship. The coefficient of correlation varies from -1 to $+1$, with -1, for example, indicating a reversed relationship (as one grows larger, the other grows smaller).

Coefficient of determination r^2

Measures the proportion of the variation of the dependent variable about its mean that is explained by the independent or predictor variable(s). The coefficient r^2 can vary between 0 and 1, inclusive. If the regression model is properly applied and estimated, the higher the value of r^2, the greater the explanatory power of the regression equation, and therefore the better the prediction of the criterion variable [RD 22]. It takes a value of 1, termed “complete correlation”, when the model and the experimental points match one-by-one.

r^2 has the following properties:

$r^2 = 1$ when input functions (the model and the experimental points) match perfectly.

$r^2 = 0$ when input functions are completely uncorrelated.

When a correlation is known to be significant, r^2 is one conventional way of summarizing its strength. In fact, the value of r^2 can be translated into a statement about what residuals (root mean

square deviations) are to be expected if the data are fitted to a straight line by the least-squares method. This value is always bounded, but it does not indicate when a fit departs linearly from the reference.

Another similar determination coefficient is R^2, that is closely related to the χ^2 criteria, and is defined as:

$$R^2 = 1 - \frac{\sum_{i=0}^{N-1}(f_i - y_i)^2}{\sum_{i=0}^{N-1}(y_i - \bar{y})^2} \qquad (150)$$

$$R^2 = 1 - \frac{\text{unexplained variation}}{\text{total variation about the mean}} \quad [-\infty \ldots 1]$$

R^2 has the following properties:

$R^2 = 1$ when input functions (the model and the experimental points) match perfectly.

$R^2 = 0$ when input functions are completely uncorrelated.

$R^2 = -\infty$ when input functions are completely anti-correlated.

An ill conditioned case occurs when the model *y* is distributed around zero in an horizontal line: this causes both correlation factors to take small values even in the presence of good fits.

In summary, r and R are the correlation coefficients, while r^2 and R^2 are the determination factors. It is on the last two values that the present analysis is based. The squared values are used to simplify the understanding, and both r^2 and R^2 are used to get as much information as possible for the goodness of the fit. At the end of the study, maybe it will be judged that only one identifier is sufficient for a correct identification.

Further details regarding the correlation/determination coefficient can be found at the following references: [RD 19, Chap. 15], [RD 21, Chap. 11], [RD 22, Chap. 11], [RD 23, Sect. 24.12].

Processing:

Variable	Descriptive Name	I/O	Type	Ranges / References / Remarks
N	Dimension of input vectors	i	i	$i = 0..N-1$
y_i	Ordinate values of reference data points	i	r	
f_i	Ordinate values of fitted data	i	r	
s	Standard deviation	o	r	
r^2	Determination factor	o	r	$-1 \le r^2 \le 1$
R^2	Determination factor	o	r	$-\infty < R^2 \le 1$

9.6 SINC SMOOTHING

The Sinc smoothing function is a moving average that convolves signals with normalized coefficients computed form an apodized Sinc filter. The amount of smoothing is controlled by two parameters: the amount of smoothing and the number of zeroes (at right of origin) used in the sinc function.

$$V'[n] = \sum_{i=-w}^{+w} V[i+n]\, S(w,i) \tag{151}$$

$$S(w,i) = \frac{\mathrm{Sinc}(i\ N^z / w)\ A(i/w)}{\sum_{j=-w}^{w} \mathrm{Sinc}(j\ N^z / w)\ A(j/w)} \tag{152}$$

$$A(p) = \begin{cases} e^{-10p^2} & -1 \le p \le 1 \\ 0 & \text{otherwise} \end{cases} \tag{153}$$

This smoothing algorithm computes the output value for a given point using the point's neighbors by combining an equal number of neighboring points before and after the point being smoothed. Special considerations must be taken into account for the extremities of the numerical vector, where indiciation becomes invalid. Indeed some points will not have enough neighbors so a method for fabricating adjacent values must be implemented. In that case, many options are possible:

The "bounce" method uses $V[i]$ in place of the missing $V[-i]$ values and $V[n-i]$ in place of the missing $V[n+i]$ values. This works best if the data is assumed to be symmetrical about both the start and the end of the wave.

The "wrap" method uses $V[n-i]$ in place of the missing $V[-i]$ values and vice versa. This works best if the wave is assumed to endlessly repeat.

The "zero" method uses 0 for any missing value. This works best if the wave starts and ends with zeroes.

The "fill" method uses $V[0]$ in place of the missing $V[-i]$ values, and $V[n]$ in place of the missing $V[n+i]$ values. This works best when data represents a single event.

The "zero" method is chosen for the case of zero-mean noise smoothing.

9.6.1 Definition of variables

The various variables used by the sinc interpolation algorithm are given in the following table with their description and ranges.

Variable	Descriptive Name	I/O	Type	Ranges / References / Remarks
V	Input signal to be smoothed	i	r	
N	Dimension of input vectors	i	i	
n	Indices of input vector points	i	i	$n = 0..N-1$
N^s	Smoothing order	i	i	0 for none, 5 for low, 10 for medium, and 20 for high smoothing.
N^z	Number of zeroes in the zinc function (at right of origin)	i	i	4 is about the minimum, 8 is good, 16 is more than good, while larger values do not add any improvement.
A	Apodization function	f	r	
w	Half width of the smoothing function	t	i	$w = \text{Floor}\{N^z\ N^s / 2\}$
V'	Output smoothed signal	o	r	

9.7 DEFINITIONS

In this appendix, we review some of the basic terms used in the document. For each term, we provide (in *italics*) the definition established by the mission prime contractor, if such a definition exists. Then, if necessary, we present an interpretation of the definition for the CrIS instrument SDR Algorithms.

9.7.1 Sensor Calibration

Sensor calibration, is the procedure for converting instrument measurement data into data with the required physical units while correcting systematic errors.

Three types of calibration for CrIS can be identified:

Radiometric Calibration: The process of assigning absolute values in radiance units, (noted [r.u.] expressed in $\mathrm{m}W/(\mathrm{m}^{-1}\ \mathrm{sr}\ \mathrm{cm}^{2})$) to the intensity axis (y-axis) with a specified accuracy. This calibration equation remodulates the data to real components. The radiometric calibration implies the knowledge of a certain spectral calibration.

Spectral Calibration: The process of assigning absolute values in cm^{-1} to the wavenumber axis (x-axis) with a specified accuracy. Also the process of removing systematic errors from the Instrument Line Shape (ILS) with a specified accuracy.

Geometric Calibration: The process of assigning an absolute earth surface location in latitude and longitude to a given atmospheric spectrum with a specified accuracy.

9.7.2 Raw Data Record (RDR)

Raw data records are full resolution, unprocessed digital sensor data, time-referenced and earth located (or orbit-located for in-situ measurements), with radiometric and geometric calibration coefficients appended (but not applied) to the data. Aggregates (sum or weighted averages) of detector samples are considered to be full resolution data if the aggregation is normally performed to meet resolution and other requirements. Sensor data are unprocessed with the exceptions of lossless data compression (decimation and bit trimming) which is allowed [RD 24].

All calibration data will also be retained and communicated to the ground without lossy compression.

The CrIS contractor shall be responsible or generating operational RDRs ([**RD 25**] 3.2.1.1.3.1).

9.7.3 Sensor Data Record (SDR)

Sensor data records are full resolution sensor data that are time referenced, earth located (or orbit-located for in-situ measurements), and calibrated by applying the calibration information including radiometric and geometric calibration coefficients and georeferencing parameters such as platform ephemeris. These data are processed to engineering units (radiance). Calibration, ephemeris, and

any other ancillary data used for the conversion are either included directly in the SDR product or otherwise referenced as external files.

The requirement to be able to convert the sensor units back to sensor raw data (counts) is removed, as some mathematical operations (like convolution) are not reversible (SRD 3.2.1.1.2.1 and [**RD 24**])

9.7.4 Environmental Data Record (EDR)

Environmental data (also termed “mission data”) refers to all data, atmospheric, oceanographic, terrestrial, space environmental, and climatic, being sensed and collected by the satellite or derived, at least in part, from these measurements.

9.7.5 Data product Levels

The following table summarizes the various levels of data distribution for the CrIS products:

Table 17: CrIS Product Levels Classification

Level	Description
Level 0	Raw Data Records (RDR)s from CrIS sensor formatted to CCSDS transmission standards. Unprocessed raw data packages of instrument data at original resolution, are time ordered (no overlap), with duplicate packets removed. Contents of data record includes sensor raw science data, housekeeping and calibration data merged with spacecraft orbit information (ephemeris, attitude, and time data). The data granule is assumed to be 1.25 orbit maximum. → RDR sensor output
Level 1A	Level 0 data (including reconstructed interferograms) which may have been reformatted or transformed reversibly, located to a coordinate system, and packaged with needed calibration characterization data needed to begin calibration procedure.
Level 1B	Radiometrically, spectrally (frequency), and geolocated calibrated spectra mapped onto EDR channel sets with specific ILS and apodization, with annotated quality indicators. → Output of SDR Algorithms
Level 2	Environmental variables retrieved from Level 1 data. Geolocated profiles of pressure, temperature, and humidity of the atmosphere. Land and ocean skin temperature, and total column ozone → Output of EDR Algorithms

The present document refers to the computation of Level 1B data.

9.7.6 Measured Data

Measured data is all raw sensor data acquired by the instrument after digitization.

By this is meant the data points from the source signal. In the case of CrIS, the source signal can be a raw unprocessed interferogram sampled at full resolution from any of the nine FOVs and from any of the three IR spectral bands covered by a FOV.

The following separates the different measurements taken by the instrument according to the physical meaning and content of the observational data acquired.

Scene Measurements

CrIS will take measurements of the atmosphere at different angles. The surface of the earth is scanned in discrete steps using the pointing mirror. A single scene measurement is taken at each pointing value.

Deep Space Measurements

The instrument itself is contributing to the observed spectrum. In order to remove this contribution, it is necessary to take a measurement of a “cold” scene, i.e. a scene with negligible radiance. Since the instrument contribution is varying, mainly because of temperature orbital variations, this offset measurement shall be repeated regularly.

Blackbody Measurements

Measurements of an internal calibration source, a well-characterized blackbody source, are performed to characterize the instrument responsivity (or gain). These measurements are also repeated regularly because of the expected responsivity variations. A complete determination of the instrument gain is composed of several blackbody measurements combined with an equivalent number of deep space measurements combined in a moving average.

Of all the measurement types listed previously, only the scene measurements contain the desired scientific information, i.e. spectra of the atmosphere. All other measurements are characterization measurements for calibration. Using the results from these characterization measurements, the calibration procedure is applied to the scene measurements.

Deep space and blackbody measurements are used for the radiometric calibration. Deep space measurements are taken for the subtraction of the instrument contribution (self-emission) from the scene measurements and blackbody measurements.

9.7.7 Calibration Data

Calibration data are defined as all the additional data sent by the instrument, apart from the observational data, required by the ground processing to allow full interpretation of its observational data for the delivery of ground segment data products.

From the instrument point of view, calibration data are those data that are used in the processing and come from the actual measurement data stream (instrument data packets from the signal processor electronics), since interpretation and evaluation of the observational data is done on ground. These data include mainly calibration information, like ICT temperatures, spacecraft position, laser wavelength, etc. but also instrument characterization data.

9.7.8 Ancillary Data

Ancillary data are all data to be provided by external source to allow full interpretation and evaluation of its observational data.

Ancillary data are defined as all the additional data required by the ground processing for the generation and delivery of ground segment data products, coming neither from the space segment nor from the ground segment itself. These data are intended to be rarely changed. They include constant definitions, templates for data validation, look-up tables for data conversion, etc.

9.7.9 Other Instrument Specific Terms and Definitions

Accuracy

A measure of correctness to a true value. Under most reasonable conditions accuracy may have a probabilistic distribution function, i.e. normally or Gaussian distributed. If symmetrically distributed the standard deviation, 1σ or some other interval 2σ or 3σ should be identified. If a measurement has small systematic errors, the measurement is considered to have high accuracy.

Apodization

Apodization (originating from the Greek work $\alpha\pi o\delta$, which means “removal of the feet”) consists in the multiplication of an interferogram by a decaying function. It is the process which attenuates the spurious “feet” in the spectral domain.

It is a mathematical transformation carried out on data received from an interferometer to alter the instrument’s response function before the Fourier transformation is calculated to obtain the spectrum.

Calibration data

Data calculated by the ground segment from specific periodical observational data (IGM) and used to calibrate subsequent scene spectra.

Decimation

Operation consisting in taking one out of a predetermined number of points in a sampled signal. It is also called “undersampling”. When a signal has been properly filtered, the decimation permits to decrease the number of points required to represent the signal with the same resolution.

Field of Regard

The Field Of Regard (FOR) has 9 Fields Of Views (FOV) forming a 3 by 3 matrix. In each band, a separate detector is associated with each FOV. (SRD 3.2.1.19)

Input data

In the present document, the term input refers to the origin with respect to the ground processor. It also implicitly means data that is continuously produced. Thus, input data will contain either the primary data coming from the Space Segment or additional data coming from the Flight Operation Segment.

Instrument Line Shape (ILS) and Resolution

The ILS is the response of the spectrometer to a monochromatic spectral stimulus. A distinct ILS exists for each wavenumber and for each FOV. In general, the ILS corresponds to a small deviation from an ideal sinc response.

The resolution of the instrument is defined as the FWHM of the ILS. For the sinc function definition we have:

$$\text{FWHM} = \frac{1.2}{2\,MPD} \quad \text{(unapodized)}$$

$$\text{FWHM} = \frac{2}{2\,MPD} \quad \text{(Hanning apodized)}$$

Interferogram

The intensity $I(x)$ of the combined IR beams, measured by the detector of an interferometer as a function of the moving mirror displacement x.

Interferometer Sweep

An interferometer sweep is the data recording for a single measurement resulting in a complete interferogram. A sweep can be in either direction, reverse or forward.

Measurement Scan Sequence

A measurement scan sequence comprises a sequence of interferometer sweeps within a fixed time interval at variable azimuth angle with respect to the CrIS local normal reference frame. See [RD 29] for more details.

Scanning occurs in the cross track direction using a scan mirror angled at 45° to the optical axis. The resulting scan pattern for this scan configuration is shown in Figure 16. Although image rotation results, this scan provides adequate performance while minimizing scan mirror size and complexity. The scan mirror assembly is designed to keep the field of view on a fixed location on the ground during integration; this process is termed Image Motion Compensation (IMC).

Noise

The noise performance requirements are defined at the aperture of the system by the noise-equivalent radiance difference (NEdN) arriving from the top of the atmosphere (TOA). The noise-equivalent temperature difference (NEdT) at a given wavenumber is defined by dividing the NEdN at that wavenumber by the derivative with respect to the Planck black body radiance function, evaluated at 250 degrees K at the same wavenumber.

Optical Frequency

As commonly used, optical frequency, σ is the reciprocal of the radiation wavelength λ and has the modern-day units of cm^{-1} and are called wavenumbers.

Optical Path Difference

When two optical waves are separated temporally by the equivalent of one wavelength, recombination leads to constructive interference or consonance. When the separation is a half wave, destructive interference or dissonance occurs. The above separations are referred to as optical path difference (OPD) denoted Δ, and may vary from zero to many waves. Related to OPD is the term phase difference, $\delta = k(x_2 - x_1) = k\Delta$, where $k = 2\pi / \lambda$ and is referred to as the propagation number. The physical meaning of k is that it may be interpreted as the number of wave per $2n$ centimeters.

Precision

Precision is measure of repeatability, either short term or long term, in performing a measurement. Under most reasonable conditions precision may have a probabilistic distribution function, i.e. normally or Gaussian distributed. If symmetrically distributed the standard deviation, 1σ or some other interval 2σ or 3σ should be identified. If a measurement has small experimental or uncertainties, the measurement is considered to have high accuracy.

Radiation Terms

Radiance and spectral radiance are field quantities, as in Maxwellian electromagnetic theory and correspond to the radiant power per unit solid angle per unit area from a source and additionally per unit wavelength, $\Delta\lambda$ or unit optical frequency $\Delta\sigma$. The chosen units in the CrIS study are mW/(m^2 sr cm^{-1}). The unit cm^{-1} denotes wavenumbers.

Radiance and spectral radiance are denoted by the symbol $L(\sigma)$. The term $B(\sigma)$ appear in much of the FTIR literature and denote spectral radiance and when referred to a blackbody.

Repeatability

The closeness of the agreement between the results of successive measurements of the same measure and carried out under the same conditions of measurements.

Scene

Atmosphere observational data; defined in contrast with blackbody and deep space observation.

Spectral Bands

A spectral band is defined as the radiometric pass band of the scene radiance for a single detector or group of detectors where the edge of the band is defined by the 50% response point relative to the peak response in that band.

Spectral Bin Size

The spectral bin size is defined as $1/(2\ MPD)$, where MPD is the optical path difference from Zero Path Difference (ZPD) in the sampled interferogram. The spectral bin size is a function of off axis field angle.

Spectrum

A display or plot of radiation intensity as a function of wavelength or frequency.

Unapodized Spectral Resolution

The unapodized spectral resolution is defined as $1/(2\ MPD)$, where MPD is the maximum on-axis optical path difference from Zero Path Difference (ZPD) in the sampled interferogram.

Zero padding

The process of adding zeroes at the extremities of interferograms in order to bring their length to a number of points corresponding to the smallest power of 2 greater than the initial number of points. Zero-padding (sometimes wrongly called “zero-filling”) is usually performed to speed-up the computation process by bringing the number of points of the interferogram vector compatible with standard fast Fourier transform algorithms. But special FFTs like mixed radix routines also exist for dimensions that are factor of small prime factors, that can circumvent the necessity of doing zero padding. Care must be taken to the edge effects: in order to avoid discontinuities, the interferogram must first be first be removed from its DC constituent by a DC offset removal procedure.

— End of document —